Thesis for the degree	עבודת גמר (תזה) לתואר
Doctor of Philosophy	**דוקטור לפילוסופיה**
Submitted to the Scientific Council of the	מוגשת למועצה המדעית של
Weizmann Institute of Science	מכון ויצמן למדע

By	מאת
Lior Embon	**ליאור אמבון**

חקר הדינמיקה והריתוק של מערבולת בודדת במוליכי-על מן הסוג השני באמצעות מיקרוסקופ סורק מבוסס "התקן התאבכות קוונטית של מוליכי-על" בקצה חוד

Study of dynamics and pinning of single vortices in type-II superconductors using a scanning SQUID-on-tip microscope

Advisor:	מנחה:
Eli Zeldov	אלי זלדוב

December 2014	כסלו התשע"ה

Acknowledgements

First and foremost, I would like to extend my gratitude to my advisor Prof. Eli Zeldov. He has been a fabulous mentor, combining vast knowledge, incredible intuition and competency with endless patience and kindness. This work has been the most challenging and fulfilling thing I have ever done and I thank him for the opportunity to be a part of it.

Dr. Yonathan Anahory has been my main partner throughout this work. His devotion and hard work contributed tremendously to my success and I thank him for a fruitful and very enjoyable collaboration and friendship.

I wish to thank Dr. Yuri Myasoedov for his continuous support and involvement in my project, and for taking the time to teach me essential skills and practices. His able hands and endless patience have been a great help.

I would also like to thank Dr. Michael Rappaport who has always made himself available to provide good advice and clever solutions.

My time spent working with Prof. Martin Huber was both pleasant and highly educational, and for that I am grateful.

I have had the pleasure of working along some great people in the group: Dr. Amit Finkler, Dr. Yehonathan Segev, Dr. Denis Vasyukov, Lior Neeman, Ella Lachman, Jonathan Reiner, Dr. Jo Cuppens, Dorri Halbertal, Dr. Alex Meltzer, Aviram Uri and Dr. Naren Hoovinakatte. These have all contributed to my research and I thank them for that.

Special gratitude goes to the members of the Gas Liquification Center, the Physics Instrumentation workshop, the Electronics and Data Acquisition workshop and the department Secretariat for creating a pleasant and supportive working atmosphere.

Finally, I thank my wife Tamar for her constant support and endless strengthening love.

I dedicate this work to the memory of Shlomi Sharon. Shlomi was a true craftsman, who took my ideas and designs and turned them into reality. His contribution to this work is beyond quantification. May he rest in peace.

עבודה זו מוקדשת לזכרו של שלומי שרון אשר נלקח מעמנו בטרם עת. שלומי היה אומן במלוא מובן המילה, אשר לקח את רעיונותיי ותכנוניי, והוציא אותם מן הכוח אל הפועל. תרומתו לעבודה זו לא תסלא בפז. יהי זכרו ברוך.

Table of contents

List of figures

List of abbreviations

SQUID – Superconducting QUantum Interference Device

SOT – SQUID-On-Tip

SSM – Scanning SQUID Microscopy

SSAA – Series SQUID Array Amplifier

SEM – Scanning Electron Microscope

AFM – Atomic Force Microscope

MFM – Magnetic Force Microscopy

SHPM – Scanning Hall-Probe Microscopy

MRFM – Magnetic Resonance Force Microscopy

TF – Tuning Fork

GL – Ginzburg-Landau

Abstract

A novel scanning SQUID-on-tip (SOT) microscope has been designed and built. SOTs as small as 46 nm were fabricated at the apex of a sharp pulled quartz tip. The SOTs present flux noise down to $50\, n\Phi_0/Hz^{1/2}$ which is on-par with the best reported SQUIDs. They can operate at magnetic fields of up to 1 T and have a wide bandwidth, from dc to over 1 MHz. Because the SOTs have an ideal geometry for scanning microscopy, they may be scanned merely nanometers away from the surface of a sample. These properties present an unprecedented combination of resolution and sensitivity, and result in spin noise down to $0.38\ \mu_B/Hz^{1/2}$, almost two orders of magnitude better than any SQUID before.

The scanning SOT microscope is a versatile tool which can be used to investigate a wide variety of systems that display magnetic structure on the nm scale. The design of the microscope, fabrication and characterization of the SOT's, as well as examples from studies of flux flow in superconductors and emerging magnetic phenomena at the interface of oxides are presented in part I of the thesis.

In part II, I report using the scanning SOT microscope for the investigation of the dynamics of quantized magnetic vortices and their pinning by materials defects in lead films with unprecedented sub-Å sensitivity to vortex displacement. We measured, for the first time, the fundamental dependence of the elementary pinning force of multiple defects on the vortex displacement, revealing a far more complex behavior than has previously been recognized, including striking spring softening and broken-spring depinning, as well as spontaneous hysteretic switching between cellular vortex trajectories. Our results indicate the importance of thermal fluctuations even at 4.2 K and of the vital role of ripples in the pinning potential, giving new insights into the mechanisms of electromagnetic response of superconductors.

Part I SQUID-on-tip microscopy

Introduction

High quality magnetic nano-scale imaging is a necessary tool both for the development of technologies such as quantum computation and spintronics, and for the investigation of fundamental physics such as superconductors, topological insulators, and other phenomena that involve edge currents and surface states in which spin degrees of freedom play a central role. One of the critical milestones in the intensive pursuit of quantitative nanoscale magnetic imaging tools is achieving the level of sensitivity required for detecting the field generated by the magnetic moment of a single electron due to its spin. This is called the Bohr magnetron $\mu_{B.}$

Older techniques such as bitter decoration have a very low spatial resolution and sensitivity to magnetic field, in addition to being an intrinsically static method, mostly unable to resolve dynamics [1]. The Kerr effect based Magneto-optic technique [2] and the Lorentz microscopy technique [3] can operate at video rates, allowing the study of dynamics. However, Lorentz microscopy requires very specific thin sample preparation, and magneto-optics are limited by the ability to bring the magnetic indicator close to the sample. Both are limited to very low fields.

Better magnetic imaging capabilities are displayed by scanning probe techniques such as Magnetic Force Microscopy (MFM), Magnetic Resonance Force Microscopy (MRFM), Scanning Hall Probe Microscopy (SHPM), Scanning Nitrogen-Vacancy (NV) Microscopy and Scanning SQUID Microscopy (SSM) [4]. However, most common applications of these techniques are limited by spatial resolution (SSM), magnetic sensitivity (SHPM), working distance (SSM and SHPM), bandwidth (NV centers and MRFM), operable magnetic fields (SSM), invasiveness (MFM) or a combination of the above. Currently, none of the existing techniques can directly measure the magnetic field generated by a single μ_B over practical signal averaging periods.

In the past few years we have developed a tool which is operable over a wide range of applied magnetic fields, can be scanned within nm scale proximity to the sample, and presents a unique combination of high spatial resolution and sensitivity to magnetic field [5,6].

In this part of the thesis, I will present this tool's design and realization, as well as some examples of its versatile capabilities.

Superconducting Quantum Interference Device (SQUID)

In the absence of a magnetic field, the current through an ideal single Josephson junction is given by $I = I_c sin(\Delta\varphi)$, where I_c is the maximum dissipationless current through the junction and Δφ is the phase difference between the Ginzburg-Landau wave functions of the two superconducting electrodes on both sides of the junction. If we introduce a magnetic field into the junction, we must replace Δφ with a gauge invariant term

$$\gamma \equiv \Delta\varphi - \Phi_0/2\pi \int A \cdot ds$$

where A is the vector potential, $\Phi_0 = h/2e$ is the flux quantum (h is the Planck's constant and e is the electron charge), and the integral ds is taken along a certain path.

A dc SQUID consists of a superconducting loop with two Josephson junctions or weak links. The maximal dissipationless current I_{max} which can be supported by the SQUID depends on the magnetic flux passing through it [7,8].

We start by writing the expression for the magnetic flux using a closed contour taken across the two junctions and far from the edges of the electrodes.

$$\Phi = \iint B \cdot da = \oint A \cdot ds = \Phi_0/2\pi \int_{electrodes} \nabla\varphi \cdot ds + \int_{links} A \cdot ds$$

Where A is the vector potential ($B = \nabla \times A$) and we have divided the integral into an electrode part and a junction part. We have also used the Ginzburg-Landau equations to replace A by $\Phi_0/2\pi\, \nabla\varphi$ inside the superconducting electrodes where J=0. Since the phase must be single valued, the first term simply equals $\Delta\varphi_1 - \Delta\varphi_2$, where $\Delta\varphi_i$ is the phase difference across the link i. Multiplying by $\Phi_0/2\pi$ and using the definition of γ we wrote we get the relation

$$\gamma_1 - \gamma_2 = \frac{2\pi\Phi}{\Phi_0} \, mod \, 2\pi$$

We now write the expression for the supercurrent through the SQUID, which is the sum of the two currents passing through the junctions. For simplicity, we will consider the junctions to be identical $I_{c1} = I_{c2} = I_c$.

$$I = 2I_c\big(sin(\gamma_1) + sin(\gamma_2)\big)$$

Combining the last two equations we find the the maximal supercurrent through a SQUID is flux dependent and given by

$$I_{max} = 2I_c \left|cos\left(\frac{2\pi\Phi}{\Phi_0}\right)\right|$$

By tracking changes in the critical current of a SQUID, one can measure minute changes in magnetic field, transforming it into a sensitive sensor. The flux sensitivity of a SQUID is determined by its intrinsic flux noise with a typical value of the order of $S_\Phi^{1/2} = 1\ \mu\Phi_0/\mathrm{Hz}^{1/2}$.

Scanning SQUID microscopy

In SSM, a SQUID is brought to close proximity to a sample and scanned across it to produce an image of the magnetic field at its surface. In order to attain a low magnetic field noise, $S_B^{1/2} = S_\Phi^{1/2}$ / A, some SQUIDs are designed to have large pickup loops, yielding a large effective area A of the magnetometer. This is helpful under the assumption that the field is uniform on the scale of A. In recent years there has been a growing interest in the development of nano-SQUIDs for the study of quantum magnetism and for nanomagnetic imaging, where the field varies on very small length scales [9-15]. In this case, field sensitivity is compromised for the benefit of spatial resolution.

However, if one is interested in imaging magnetic dipoles, having a small diameter SQUID loop might be beneficial. By taking into account the coupling of a SQUID loop of diameter R with a dipole placed at a distance h away and pointing out of the loop's plane, we can define a spin noise

$$S_n{}^{1/2} = S_\Phi{}^{1/2}\left(1 + \frac{h^2}{R^2}\right)^{3/2} R/r_e$$

where r_e is the classical radius of the electron. In the case the SQUID is far from the dipole $h \gg R$, the noise will grow with size reduction. However, if the SQUID can be brought close enough such that h is comparable with R, we get $S_n{}^{1/2} \propto S_\Phi{}^{1/2}R$, giving further advantage to smaller SQUIDs.

Most micro- and nano-SQUIDs that are used today in SSM are fabricated using planar lithographic techniques. Although this yields highly robust devices and permits the integration of pickup and excitation loops [10], the planar geometry is an obstacle in bringing the probe close to the surface and usually imposes a lower bound of roughly $1\ \mu m$ on the sample to probe distance.

We have developed novel SQUIDs which are fabricated on the apex of a very sharp pipette. This is the ideal geometry for scanning probe microscopy as it imposes almost no limitations on the probe's proximity to the scanned sample. We call these SQUID-on-tip's (SOTs) [5,6].

SOT fabrication and characterization

Pipettes with tip diameters in the range of 40 to 300 nm are fabricated from quartz tubes with 1 mm outside diameter and 0.5 mm inside diameter using a Sutter Instrument P2000 micropipette puller. Using an evaporator, superconducting films are deposited in three self-aligned steps to create a SQUID, as illustrated in Figures 1a and 1b.

Firstly, a superconducting film is deposited on one side of the pipette to form an electrode. The pipette is then rotated to deposit an electrode on the other side, and lastly, the pipette is pointed towards the source and a thin film is deposited onto the apex ring of the pipette, forming the superconducting loop of the SQUID. In the regions where the loop overlaps the leads, stronger superconductivity is attained, while the short parts of the loop next to the gaps between the leads act as two Dayem-bridge weak links, thus forming a self-aligned SOT.

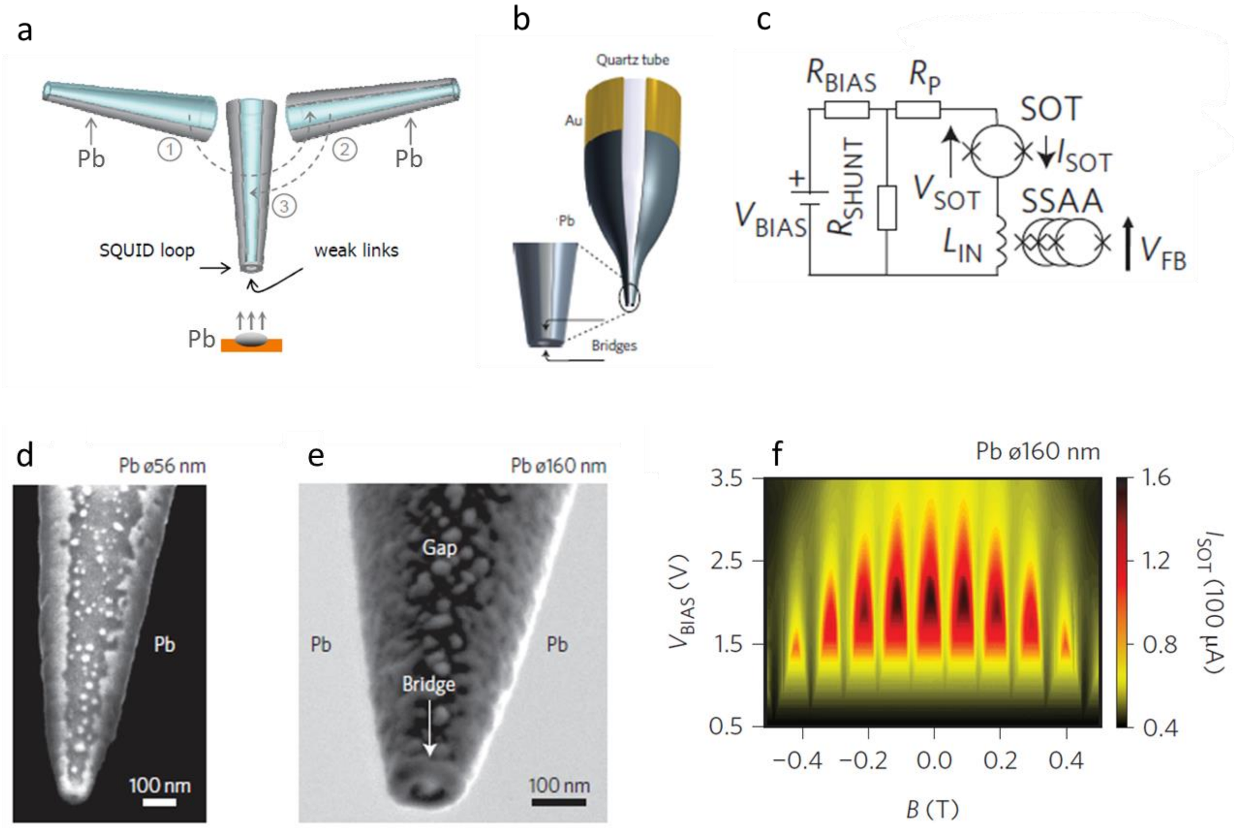

Figure 1. SOT fabrication and measurement

a, Schematic description of three self-aligned deposition steps for fabrication of SOT on a hollow quartz tube pulled to a sharp tip (not to scale). In the first two steps, Lead is evaporated onto opposite sides of the tube forming two superconducting leads and in the third, the apex ring is covered to form the nanoSQUID loop. b, Schematic illustration of the pulled quartz tube with two Pb superconducting leads connected to Au electrodes. Inset: magnified view showing the superconducting loop on the apex of the tip. The bridges that reside in the gap regions between the leads form the two weak links of the SQUID. c, Electrical schematic of the SQUID measurement circuit. d and e, Scanning electron microscope images of Pb SQUID-on-tip devices with ø56 nm and ø160 nm respectively. f, Quantum current oscillations in the ø160 nm Pb SOT

Characteristic SEM images of two SOT's are shown in Figure 1d and Figure 1e. Pb based SOT's were made as small as 46 nm and show extremely low white flux noise down to $50\, n\Phi_0/Hz^{1/2}$ (at frequencies above a few hundred Hz). These numbers represent almost two orders of magnitude improvement in spin sensitivity over any other SQUID, down to 0.38 $\mu_B/Hz^{1/2}$. In addition, the devices operate over a wide range of magnetic fields with sensitivity even at 1 T [16].

To measure the SOT we use the circuit shown in Figure 1c. A current source (voltage source V_{BIAS} with a large $1k\Omega$ R_{BIAS} in series) is used to bias the SOT and a 5.4Ω resistor R_{SHUNT} in parallel. A parasitic resistance R_P of roughly 1Ω is present in series with the SOT due to contacts, the gold leads at the basis of the pipette, and wiring. A DC SQUID Series Array Amplifier (SSAA) [5,6,10,17] is used as a cryogenic current-to-voltage converter to read out the

SOT current I_{SOT}. The SSAA is inductively coupled to the SOT circuit through a superconducting input coil L_{IN} and is operated in a closed flux locked feedback loop, the output of which V_{FB} is proportional to I_{SOT} with $V_{FB}/I_{SOT} \cong 40$ kΩ. Figure 1f shows the quantum interference pattern of the I-V characteristics of a ø160 nm SOT as measured in our system.

The SOT's usually have current-voltage characteristic with negative differential resistance above I_c which would show hysteretic behavior if they were current biased and their voltage was measured. This hysteresis is very inconvenient for sensor applications. In the abovementioned scheme, the shunt resistor provides a low resistance load-line to the SOT, creating essentially a voltage bias and allowing stable operation.

The SOT which was used for part II of this work was a Pb-based device with an effective diameter of 177 nm (83.7 mT field modulation period), 103 µA critical current at zero field, and white flux noise (at frequencies above a few hundred Hz) down to $230\ n\Phi_0/Hz^{1/2}$. Figure 2 shows the measured quantum interference pattern of I_c for this device. The asymmetric structure of this SOT provides high sensitivity even at zero applied field with flux noise of $360\ n\Phi_0/Hz^{1/2}$.

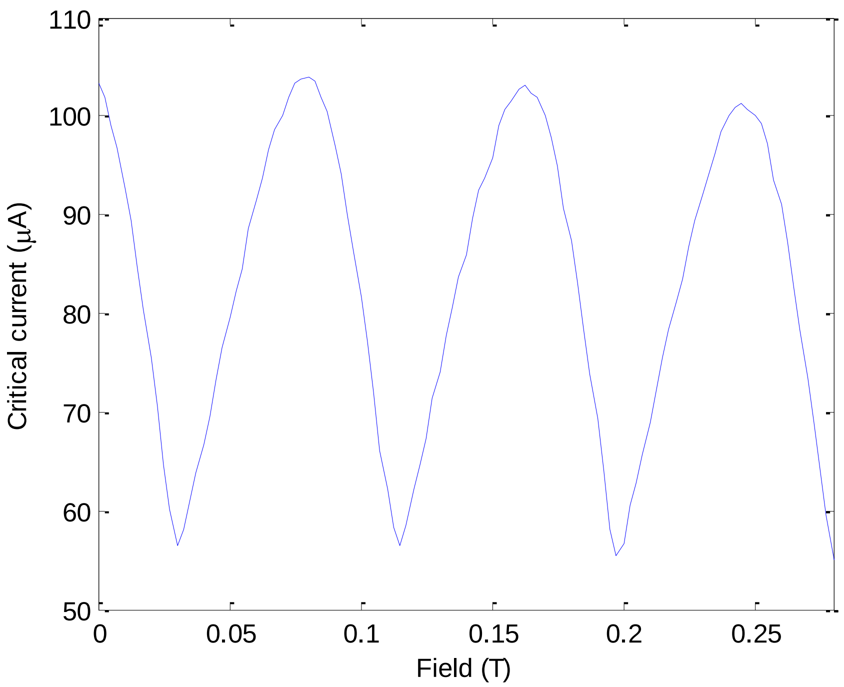

Figure 2. SOT critical current as a function of applied magnetic field

I_c of the SOT that was used in part II of this work as a function of applied magnetic field. It has a 83.7 mT modulation period which corresponds to a 177 nm diameter. The asymmetric structure of the SOT results in sensitivity at zero applied field.

Scanning SOT microscope

The SOT's are mounted onto an in-house-built scanning microscope operating at 4.2 K (Figure 3). Using the microscope we bring the sample to close proximity of the SOT and scan it across the surface, producing the magnetic image. The microscope enables coarse motion in a volume of $5 \times 5 \times 5\,mm^3$ with three Attocube piezoelectric positioners based on a slip-stick mechanism. Scanning is performed with sub-nm precision using an Attocube integrated xyz scanner with a range of $30 \times 30 \times 15\,\mu m^3$. Up to fourteen wires may be connected to the sample, enabling gating, application of current, voltage etc.

The microscope is designed for operating the SOT in combination with tuning fork based AFM [5,6]. For technical reasons, the imaging presented in this thesis was performed at a constant nominal distance between the SOT and the sample and without the height correcting feedback mechanism.

The microscope is cooled in a liquid Helium dewar inside a sealed can which allows operation in high vacuum or in a He exchange gas atmosphere. The temperature is monitored by a calibrated diode and can be slightly varied by using a heating element. The measurements presented in part II were all carried out at 4.2 K in He exchange gas at 0.95 bar.

The design and construction details, including part schematic are presented in the "Microscope design" appendix on page 67.

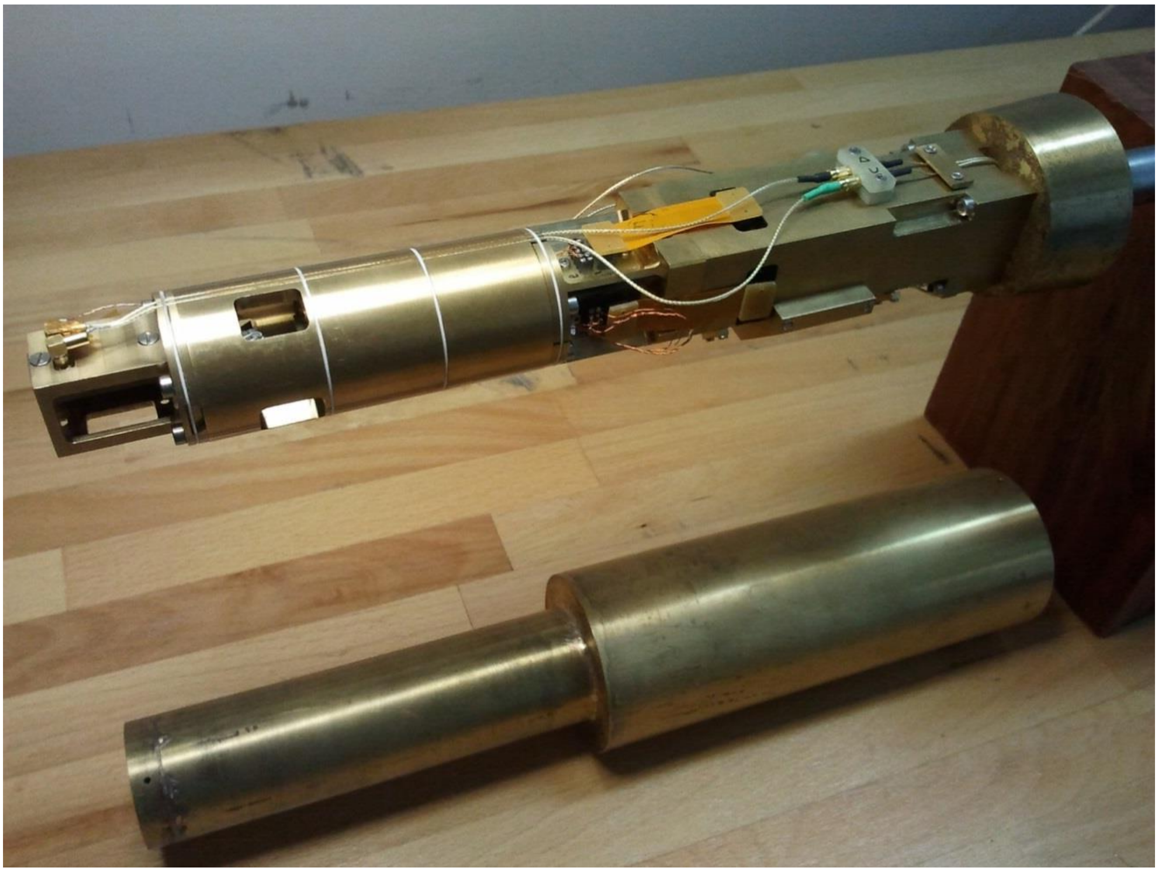

Figure 3. A photograph of the cold end of the microscope.

Visible (from the left) are the tip holder flange, the protective sleeve which is covering the tip holder, sample and positioner stack, the microscope base, the body, and the sealing cone. On the bottom of the picture is the vacuum can.

Results

The scanning SOT microscope is a highly versatile tool that has the power to explore and study magnetic phenomena which have been out of reach up until now. In part II of the thesis I will describe in detail my most complete work, studying the pinning mechanism of vortices in superconductors. For the conclusion of this part, I present some preliminary results and examples from other ongoing projects.

Vortex dynamics in superconductors

The understanding of vortex matter in superconductors has implications on both advances in superconductor-based technologies, and on the fundamental understanding of superconductivity. The scanning SOT microscope is a powerful tool in this field. Figures 4 and 5 demonstrate our ability to image individual vortices in fields spanning three orders of magnitude, from virtually zero to 0.2 T. The images in Figure 4 are of a superconducting Pb hour-glass shaped thin film, and those in Figure 5 are of a 420 nm thick strip of Nb film.

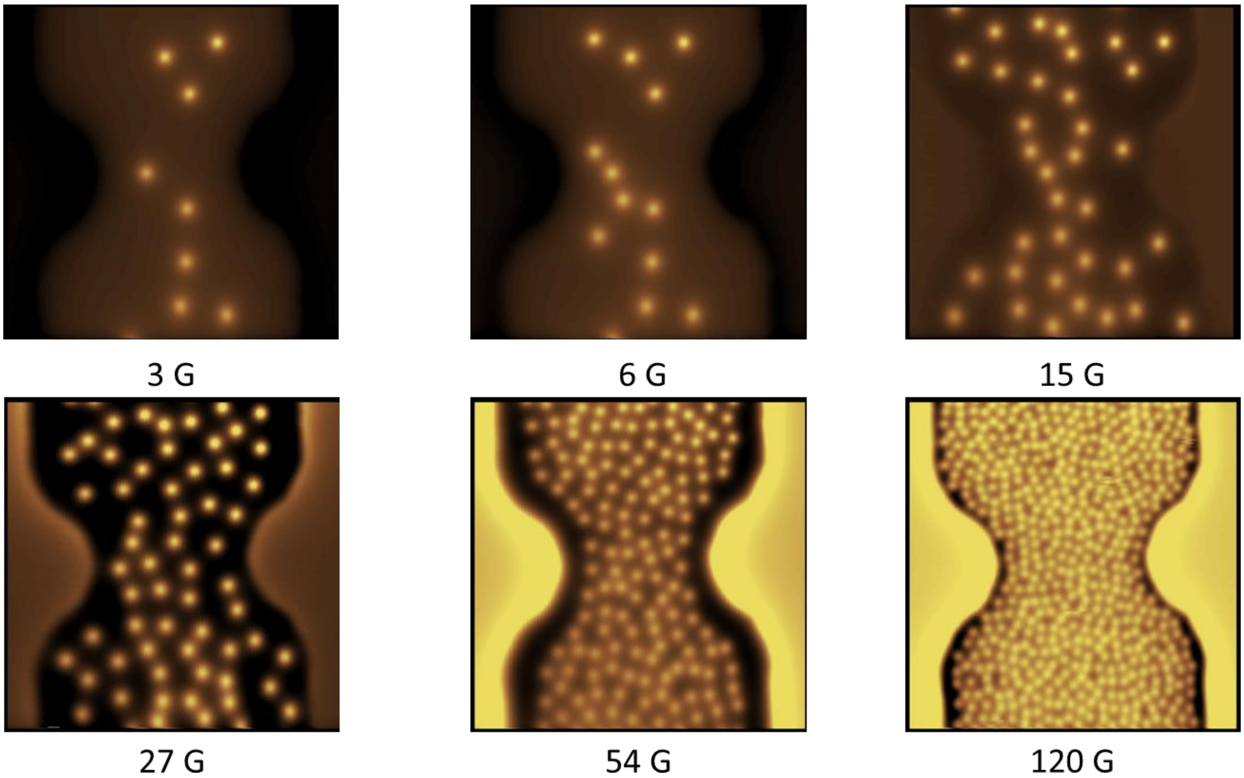

Figure 4. Scanning SQUID-on-tip microscopy images of vortices at different fields.

The images were acquired using a 225 nm diameter SOT. The scan area is $12 \times 12\ \mu m^2$ and the pixel size 100nm. The sample is an hourglass shaped thin Pb film. Prior to imaging, the film was cooled in the presence of an externally applied out-of-plane field with the indicated value. Individual vortices (yellow circles) are visible inside the film. The films outlines are visible due to the Meisner expulsion of the external field.

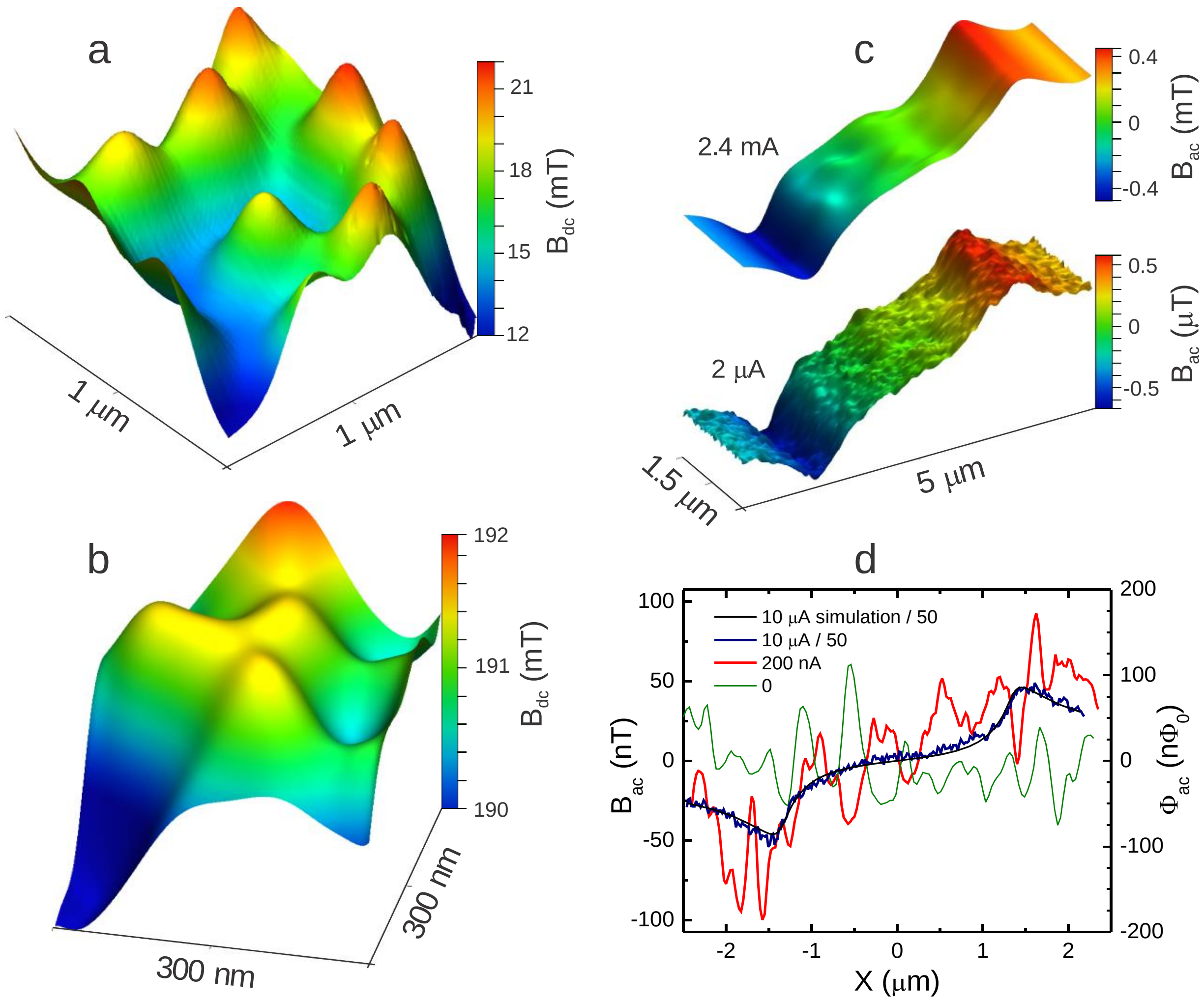

Figure 5. SOT images of vortices and a current carrying film

SOT images of vortex matter (a,b) and of magnetic field distribution generated by AC current (c,d) in a Nb film at 4.2 K. a, 3D false color plot of the magnetic field distribution measured with a ø117 nm Pb SOT displaying pronounced peaks (red) at the vortex centers. The image shows the raw data with no processing measured at a constant height of about 50 nm above the surface of a 420 nm thick Nb film. The external field was 280 G, the scan area 1×1 μm^2 and the pixel size 7 nm. The minimum distance between the vortices is 330 nm. b, Similar image as in (a) obtained with a ø88 nm Pb SOT in an applied field of about 2000 G. The scan area is 300×300 nm^2 and the pixel size 2 nm. The distance between the closest vortices is 120 nm. c, 3D false color image of the ac field B_{ac} induced by a transport current through a 3 μm wide Nb strip with I_{ac} = 2.4 mA (top) and 2 μA (bottom) at 609 Hz using a lock-in amplifier and a ø70 nm Pb SOT. Both images show raw unprocessed data (scan area 1.5×5 μm^2, pixel size 33.5 nm, lock-in time constant 100 ms). The wavy features in the top image are due to small local AC displacement of vortices by the I_{ac} = 2.4 mA. d, B_{ac} line profiles at I_{ac} = 10 μA (blue, divided by 50), 200 nA (red), and zero current (green) (pixel size 25 nm, lock-in time constant 1 s). The black curve shows the calculated theoretical field profile (divided by 50) induced by 10 μA current at 100 nm above the surface of 400 nm thick superconducting strip. Note some six orders of magnitude variation in the field values between the different panels [16].

Figure 5 also presents a measure of our minimal detectable field produced by a current of merely 200 nA applied through a 3 μm wide superconducting Nb strip.

For the study of the dynamics of vortex matter, we have designed samples that enable the application of currents through the superconducting film. These currents exert a Lorentz force on the vortices. If the force is large enough to overcome the pinning of vortices, dissipative motion will commence.

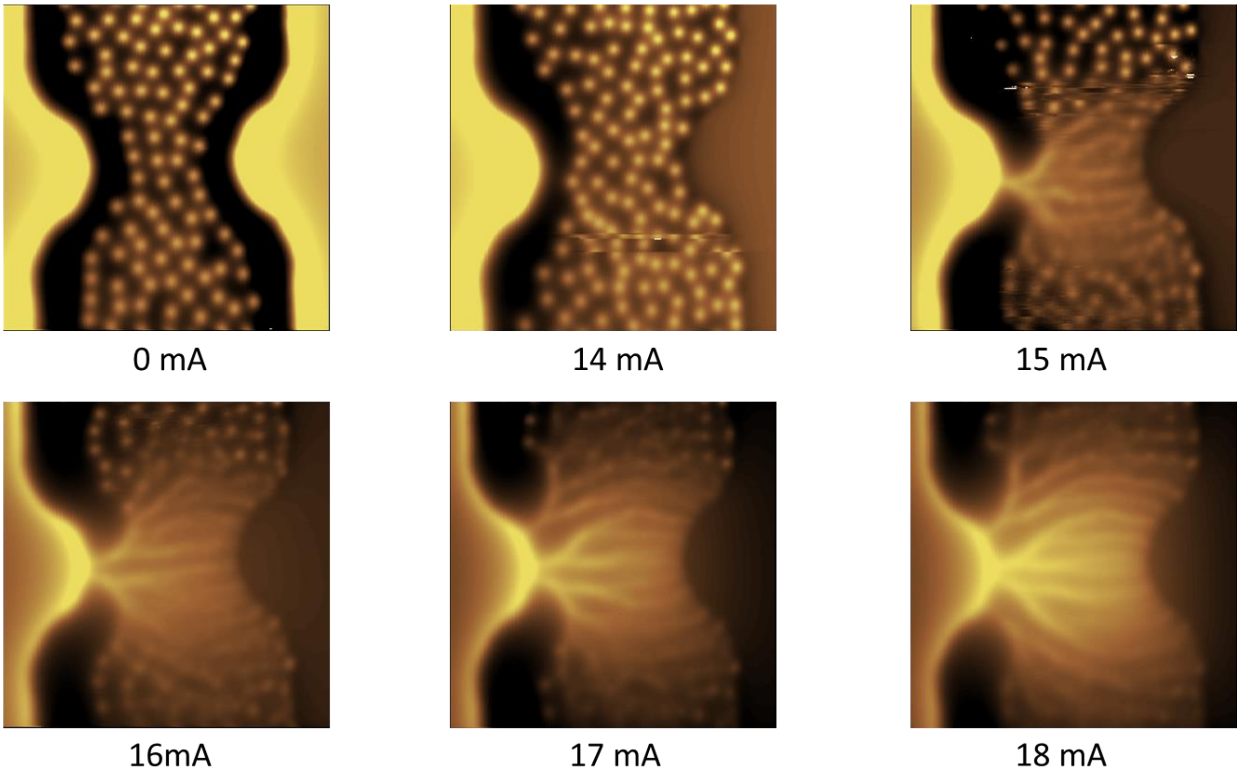

Figure 6. SOT images of flux flow

Flux flow as imaged by a 225 nm diameter SOT (External field of 42 G, scan area of 12 × 12 μm^2 and pixel size 40nm). A transport current through an hourglass shaped Pb film exerts a Lorentz force on the initially stationary vortices (0 mA). At 14 mA the vortices have moved through flux creep to the right side of the image. The streaks on the bottom of the image are hopping events which occurred as the image was being acquired. At 15 mA a channel of fast moving vortices appears. By increasing the current, more channels enter the film. 18 mA is the maximal current which this bridge can sustain before heating drives it into its normal state.

Figure 6 presents an unprecedented peak into flux flow. It shows six scans of the same area as in Figure 4 while a dc current is applied through the bridge. In the absence of current the vortices are stationary. With 14 mA, the vortices are still stationary but have moved through random hopping to the right side of the frame. The streaks which appear on the bottom half of this image are in fact hopping events that occur while the tip is scanning. 15 mA is the critical current for this constricted bridge. Flux flow begins and a voltage drop appears across the bridge. The scanning image reveals a single channel of fast moving vortices which enter at the narrow part of the constriction from the left and travel to the right while bifurcating several times into branches.

By increasing the current further, more channels are formed. 18 mA is the maximal sustainable current for this bridge. A higher current causes an unstable heating and quenching of the film.

Upon studying the onset of flux flow at different fields we find a plethora of intriguing features. Among those are the shape of the channels, the spacing between them, their number and orientation in respect to the force and the velocity of the moving vortices as indicated by the different intensities within the channels. Figure 7 presents sample images acquired while applying the highest sustainable current for the indicated field and revealing beautiful dendrite-like shapes of the vortex channels.

The onset of flux flow and the dissipation which appears with it are a major obstacle for technologies involving superconductors. These images constitute a first glance into the macroscopic mechanism of this phenomenon and are a part of an ongoing project to study this phenomenon. Improving the understanding of flux flow has implications both on applications and on the basic understanding of superconductors.

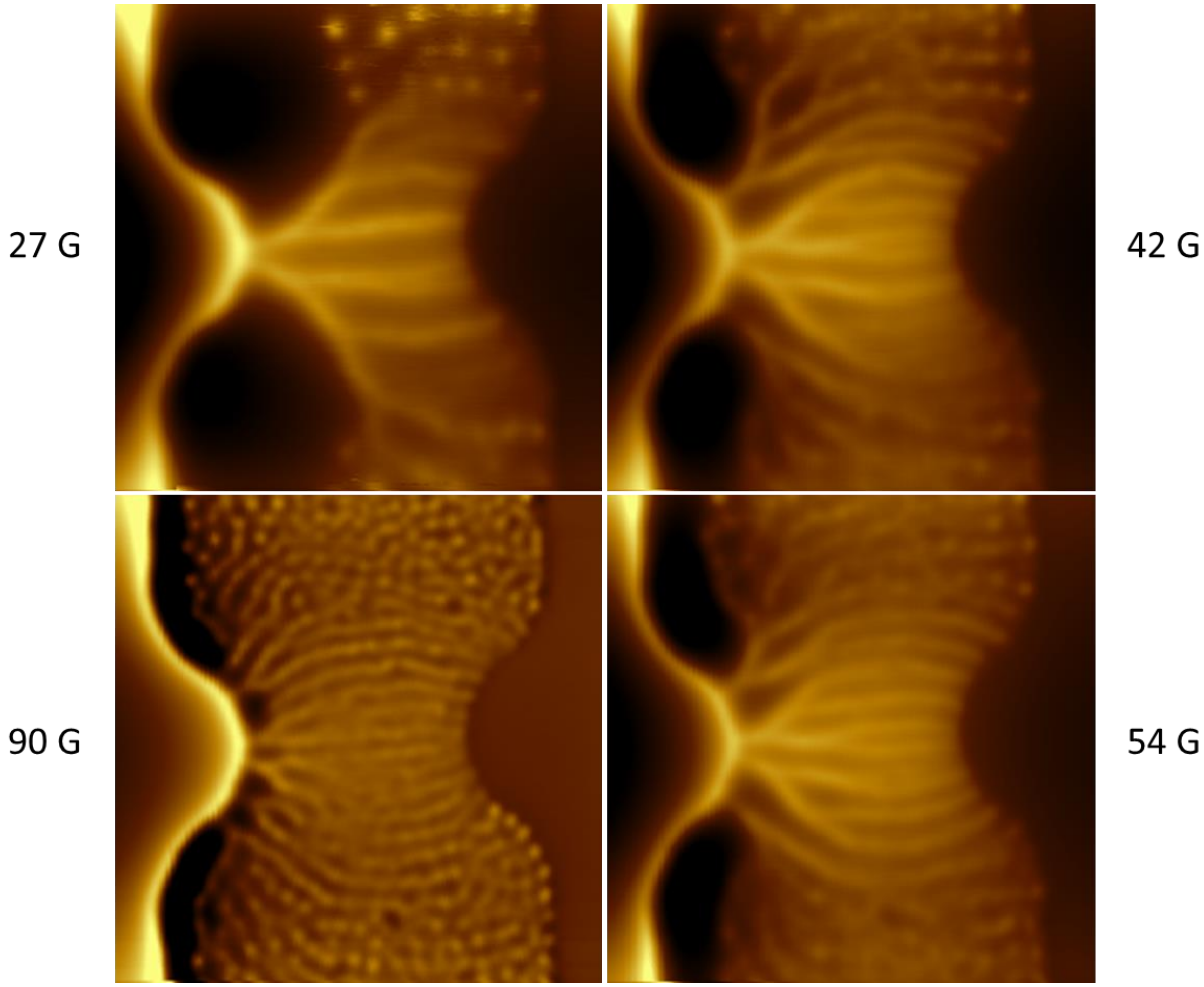

Figure 7. Flux flow at different fields.

We have repeated the measurement described in Figure 6 for different fields. These images show the vortex channels at the maximal sustainable current for the indicated field. The spacing between the channels decreases as the density of vortices increases.

Magnetism in LMO-STO

Heterostructures of $LaAlO_3/SrTiO_3$ (LaO/STO) and $LaMnO_3/SrTiO_3$ (LMO/STO) interfaces have been the focus of intense research in the past years due to their technological potential and unusual physical properties. Our scanning microscope allows us to study these magnetic phenomena on a nanometric scale, where the fundamental building blocks of the magnetic behavior occur. Although this work is at a preliminary stage, we have already obtained some striking results which challenge some of the widely accepted ideas in this field.

Over the past few months we have been measuring samples with STO as a substrate and varying thicknesses of LMO, from 6 to 24 unit cells. Global magnetization measurements on these samples carried out by our collaborators indicate an in-plane ferromagnetic behavior. Using our microscope we have found the ferromagnetic domains to be more than two orders of magnitude smaller than previously thought. We have also uncovered a still unexplained anisotropy of the domains and a domain flipping behavior which deviates from the expected picture of ferromagnetic domain wall motion.

We are currently studying samples with varying LMO thicknesses, and exploring the dependence of their magnetic structure on the direction of the applied field. We are using our unprecedented capabilities to learn about the basic building blocks of the magnetic phenomenon in these types of materials.

Figure 8 presents two sample images of $1.5 \times 1.5\ \mu m^2$ of a 12 u.c. thick LMO-STO sample. Each image was taken at a slightly different externally applied in-plane magnetic field directed along the y-axis. The images seem to be identical to the naked eye. However, by carefully subtracting the two images we reveal the minute difference between them which has a dipole-like shape, consistent with an in-plane domain flip. We fit our data to find the magnitude of the flipped domains in terms of number of spins, orientation and spatial size. We can then sweep the applied field to get the full microscopic picture along the magnetization curve of the sample, acquiring the average values and distribution (both in field and in space) of parameters such as the magnitude of the flipped domains, their spatial size, and orientation.

We are currently acquiring more statistics, comparing samples with different LMO thicknesses and exploring the dependence of the magnetic behavior on the angle between the direction of the applied field and the crystallographic axis of the samples.

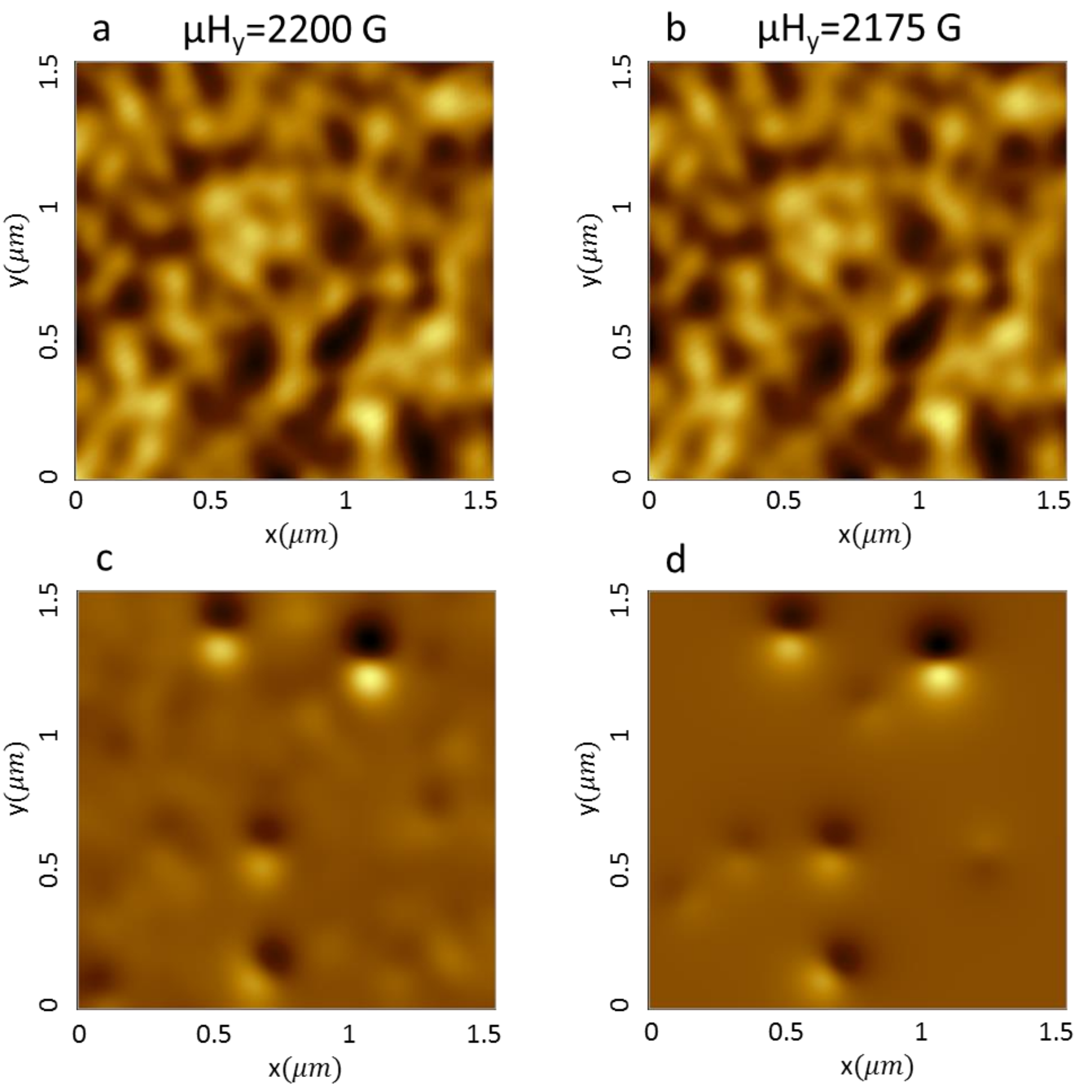

Figure 8. Sample SOT images of the magnetic structure of LMO-STO

a and b, sample SOT images of a 12 u.c. LMO-STO sample. The scan area was $1.5 \times 1.5\ \mu m^2$. The images were taken after applying an in-plane field along the y axis of 2175 G and 2200 G (b and a respectively). The span of the color scale is 50 G. c, A subtracted image showing the difference between (a) and (b). The color scale span is 3.8 G. d, A theoretical fit to (c) from which we can extract the magnitude of the flipped domains in μ_B and their spatial size. In this sample we find flips of domains with a magnitude on the order of $10^5\ \mu_B$ and a few tens of nanometers in size.

Summary

A novel scanning microscope based on a nanoSQUID which is fabricated on the apex of a sharp tip has been developed. This SOT based system possesses record breaking spin sensitivity, spatial resolution and operable magnetic fields, combined with a geometry which poses almost no limitations on the sample-probe distance. Our SQUIDs can operate at liquid Helium temperature and at applied magnetic fields of up to 1T, be made as small as 50 nm and display an extremely low flux noise of $50\ n\Phi_0/Hz^{1/2}$ which corresponds to a spin sensitivity better than $1\ \mu_B/Hz^{1/2}$. Using these newly acquired capabilities we can directly investigate a wide range of nano-scaled magnetic phenomena which were completely out of reach up until now.

Preliminary results from studies of flux flow and of magnetism in oxide heterostructures which were carried out using the microscope have been presented and a complete work on the pinning of vortices in superconductors will be detailed in part II. Planned projects for the microscope include further studying vortex dynamics in different sample geometries, studying the pinning of vortices in high-T_c superconductors, studying magnetic nano-particles, carbon nano-tubes, quantum wells and more.

In addition, we are constantly working towards improving the performance of our tools, and also expanding its capabilities. These efforts include: SOTs with sensitivity to both the out- and in-plane components of the magnetic field which have already been produced [18], the development of a measurement scheme which uses the SOT as a thermometer with record breaking sensitivity, and the development of multi-junction SOTs with tunable quantum interference that will allow working with optimal sensitivity at all operable field values.

Part II Pinning of vortices in type-II superconductors

Introduction

Vortices appear in Type-II superconductors which have, by definition, a Ginzburg-Landau parameter $\kappa \equiv \frac{\lambda}{\xi} > \frac{1}{\sqrt{2}}$ [7], where ξ is the coherence length characterizing the size of a Cooper pair, and λ is the London penetration depth. When this is the case, and above a critical value of the magnetic field denoted by H_{c1}, the domain walls separating normal regions from superconducting regions in the material have a negative surface energy. As a result, it is energetically favorable for the magnetic field to penetrate into the superconductor. It does so in the form of Abrikosov vortices, each carrying a quantized magnetic flux of $\Phi_0 = \frac{hc}{2e} = 2.07x10^{-7}\ Gcm^2$. The core size of a vortex, in which superconductivity is suppressed, is characterized by ξ, whereas the area surrounding the core through which the magnetic field penetrates is defined by λ.

Type-I superconductors such as Pb (which was used in this work) have a smaller Ginzburg-Landau parameter $\kappa \equiv \frac{\lambda}{\xi} < \frac{1}{\sqrt{2}}$, and will thus not exhibit vortex penetration. However, in a thin film, where $\lambda > d$, the penetration depth is given by the a thickness-dependent value $\lambda_{eff} \approx \lambda^2/d$ [19]. This can be much larger than the bulk value for λ and turn the film into an effective type-II superconductor.

The ability to carry non-dissipative electric currents in strong magnetic fields is one of the fundamental features of type-II superconductors crucial for many applications [20-29]. However, applying currents through the material exerts a transverse Lorentz force on the vortex matter. If the vortices are free to move, dissipative motion will commence and finite resistance will appear. This causes the critical value of current density J_c to be significantly smaller than the fundamental depairing current density J_d at which the Cooper pairs are broken and superconductivity is lost. This is a major limiting factor for superconductor-based technology.

The interaction between two vortices is an elastic repulsion one, very much like the force between two parallel electric current carrying wires. In his paper [30], Abrikosov predicted that at low enough temperatures, this repulsion will cause the vortices to form a tightly packed and ordered lattice with a density determined by the overall magnetic field. However, this picture is an oversimplification and overlooks the importance of material defects and disorder. Defects in the material may immobilize the vortices, leading to an increase in J_c. This is known as vortex pinning [31].

Single pinning potential wells $U(r)$ produced by defects are the key building blocks that determine collective pinning phenomena, in which a flexible vortex line is pinned by multiple defects. It was shown by Larkin [32] that in the presence of any disorder, the perfect lattice cannot exist, even at low temperatures. In its place, at low disorder, we should find a glassy phase which surprisingly displays quasi-long ranged order. This was given the name Bragg glass [31,33-36]. In this phase each vortex is said to be displaced from its equilibrium position by neighboring pinning sites. As a result, the average displacement of the vortices diverges logarithmically with distance, and correlation is lost. Evidence for this phase was found using neutron diffraction [36].

The global electromagnetic response of the vortex matter is governed by a complex interplay of individual pinning centers along with the interaction between the vortices, and thermal fluctuations. This gives rise to more static phases of the vortex matter.

At higher magnetic fields, the density of vortices increases. This results in screening of the elastic repulsion, decreasing its effect, and making the pinning energy the dominant term. In this case, the displacement of vortices from their equilibrium points due to pinning is a larger fraction of the inter-vortex distance. The result is a glassy phase of the vortex matter, in which there is no long range order, which can be observed as the loss of peak intensity in a neutron diffraction experiment [37].

Inspecting the role of the thermal energy, one finds that as temperature is raised, the displacements of the vortex lines with respect to their equilibrium positions become larger. Using the Lindemann criterion, which states that a crystal will melt when the thermally induced displacements become some sizeable fraction of the lattice spacing, the vortex lattice melting temperature can be determined. This defines a transition into a liquid phase. Such transitions were measured in our laboratory using local magnetization measurements [38].

A typical static phase diagram of vortex matter can be seen in Figure 9. The diagram displays the vortex-vortex elastic interaction dominated Bragg glass at low temperatures and fields, the thermally dominated liquid phase at high temperatures, the pinning dominated vortex glass at high magnetic fields, and an intermediate phase suggested by the authors [35].

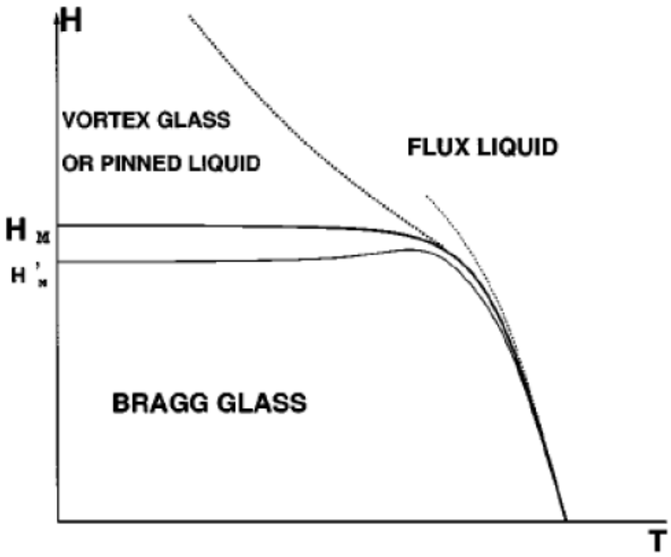

Figure 9. A typical static H-T phase diagram of a type II superconductor.

Shown: the Bragg glass phase at low temperatures and fields, the liquid phase at high temperatures, the vortex glass phase at high magnetic field, and an intermediate phase suggested by the authors. [35]

By adding a force exerted on the vortex matter, a plethora of dynamic phases is predicted to appear. If the vortices are strongly pinned in respect to the driving force, no vortex motion will occur and no resistance will arise. When the driving force is increased and reaches the proximity of the pinning force the system enters the flux creep regime [39,40]. In this phase, vortices are said to hop from one pinning site to the next through thermal activation. Further increasing the driving force should cause more vortices to depin, and a "plastic flow" to appear [41,42]. This means some vortices remain pinned while others move past them in a very non-homogenous flow.

Eventually, for a strong enough driving force, all of the vortices are predicted to depin and join the motion. The result is called a smectic flow, in which vortices move one after the other in an orderly fashion, forming channels. However, in the transverse direction to the flow, disorder prevents the coupling of channels and each has its own velocity. This phase is also known as a moving transverse glass [43,44].

At the high end, theory says the velocity of vortex motion is enough to average over disorder in both directions. Thus regaining its quasi-long ranged order. In this case we get what is called a "Moving Bragg glass". This means that in the moving frame the vortices form a Bragg glass type of lattice. In the lab frame this means that the channels are coupled and have the same velocity [45,46].

A schematic theoretical dynamic phase diagram is shown in Figure 10, presenting the different predicted vortex matter phases as a function of the temperature, the driving force, and the pinning force. Most of these phases and transitions have not been observed experimentally so far for lack of adequate tools [47].

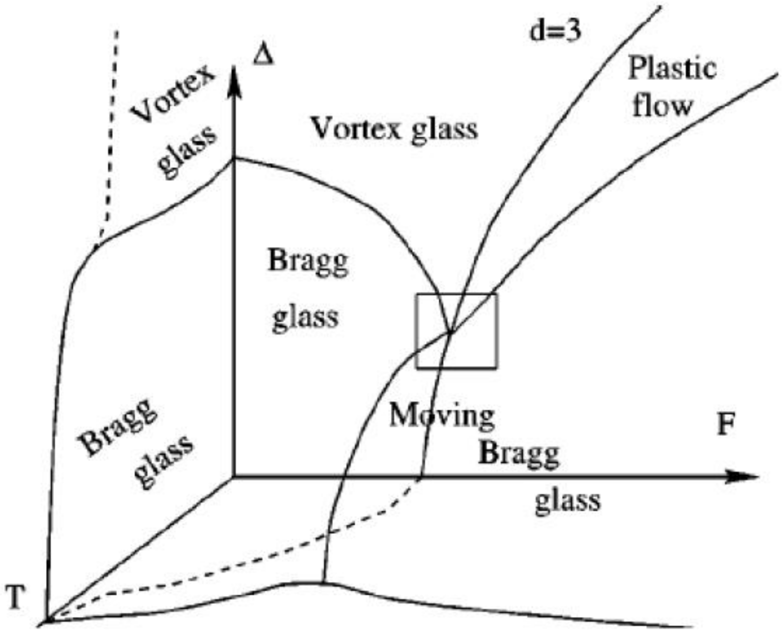

Figure 10. A schematic dynamic phase diagram of vortex matter in a type II superconductor.

Δ is the disorder, F is the driving force, and T is the temperature. At low F the static phases are shown: Bragg glass at low T and Δ, vortex glass at high Δ, and liquid at high T. At higher F and low Δ the moving Bragg glass regime is shown, and at higher Δ, the Plastic flow regime. The smectic flow phase does not appear [47]

The important role of vortex pinning in the macroscopic electrical and magnetic properties of superconductors, and thus on any superconducting technology has been a driving force for vast research in this field. Advances in materials science have enabled several groups to controllably produce nanostructures of nonsuperconducting precipitates to optimize the pinning of vortices in superconductors and to achieve J_c up to 10-30% of J_d [21-29]. In artificially-engineered pinning structures, the shape of $U(r)$ can also be made asymmetric to produce the intriguing vortex ratchet and rectification phenomena [48,49].

In recent years, local studies of individual vortices using scanning probe techniques have revealed phase transitions and depinning of vortex lines and the collective motion of the vortex lattice [50-62]. These studies include a measurement of the depinning force of a pinned vortex using MFM manipulation [53], SHPM imaging of the dissipative motion of a single vortex hopping from pinning site to pinning site in response to an alternating magnetic field [58], and Scanning Tunneling Microscopy (STM) imaging of vortex trajectory due to an oscillating magnetic field and the collective motion of the vortex lattice [59].

Even so, the intrinsic structure of a single pinning potential well $U(r)$, which determines the fundamental interaction of vortices with pinning centers, has not yet been measured directly. For theoretical calculations and artificial pinning structure design, $U(r)$ is commonly assumed to have an isotropic Lorentzian-like shape with a characteristic size of ξ [30, 63-65].

Methods

Sample

Difficulties with the measurement of $U(r)$ arise from the necessity of de-convoluting the effect of multiple pinning defects along the elastic vortex line, and from the lack of experimental techniques for extracting $U(r)$ on the scale of the superconducting coherence length ξ (ranging from 2 to 100 nm for different materials). To avoid the complexity of the situation in which the vortex line behaves like an elastic string pinned by multiple defects [53], the vortex length should to be of the order of ξ. This situation can be achieved in thin superconducting films of thickness $d \cong \xi$ in a perpendicular magnetic field. Moreover, in order to simplify the interpretation of experimental data, it is desirable to choose a film in which the three basic length scales of the system are comparable, $\xi \cong \lambda \cong d$, where λ is the bulk magnetic penetration depth. We have therefore chosen to study Pb thin films (T_c = 7.2 K) with $d = 75$ nm, ξ(4.2 K) = 46.4 nm, and λ(4.2 K) $\cong$ 90 nm. In this case, the vortex can be regarded as a particle in a two-dimensional (2D) potential landscape of pinning defects.

A 75 nm thick Pb film was deposited by thermal evaporation on a silicon substrate cooled to liquid nitrogen temperature in order to prevent island growth that would otherwise result from the high mobility of the Pb atom. The base pressure was 2×10^{-7} Torr and the deposition rate was 0.6 nm/s. A protective layer of 7 nm of Ge was deposited in-situ to prevent oxidation of the Pb. The sample was patterned using a standard lift-off lithographic process. Six micro-bridges of different widths (ranging from 5 to 20 μm) were patterned, through which currents could be applied independently. The measurements presented here were performed on an 8 μm wide bridge.

Several film characterization techniques were employed. These are detailed in the “Sample characterization” appendix in page 58.

Single-vortex state preparation

To avoid the effects of vortex-vortex interaction, the sample was prepared in a single-vortex state. For this aim, a quench and field-cooling technique was used. A current of a few tens of mA was applied to the microbridge which drove it to the normal state and heated it above T_c. The current was then turned off abruptly, and the film was field-cooled in an applied field of about 1 G. Due to a small remnant field of the superconducting magnet, the exact nominal value of the applied field required to trap a single vortex was found by trial and error. Figure 11 shows four

$12{\times}10\ \mu m^2$ scans of the same 8 μm wide bridge with 0, 2, 6 and 15 trapped vortices after field cooling in 0.7, 1, 3 and 7 G, respectively. Figure 12a shows a SOT image of the microbridge in which a single vortex was trapped upon field cooling at about 1 G.

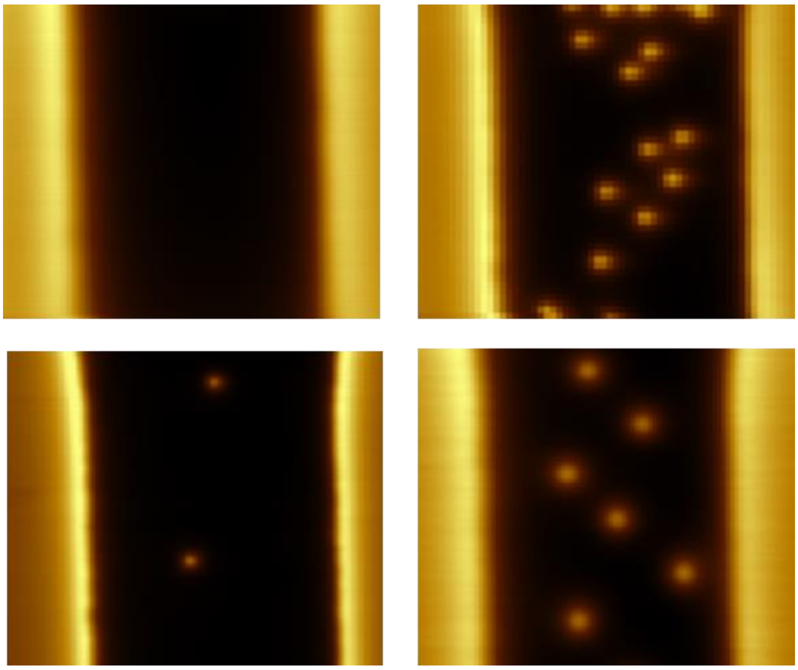

Figure 11. Single vortex state preparation

B_{dc} scans after field cooling. The $12{\times}10\ \mu m^2$ images show 0, 2, 6 and 15 vortices in the same area of the 8 μm wide bridge after field cooling in fields of 0.7, 1, 3 and 7 G, respectively.

Vortex manipulation, imaging and data extraction

A small ac current I_{ac} is applied along the bridge (y direction) resulting in a Lorentz force on the vortex $F_{ac} = \Phi_0 J_{ac}$ along the perpendicular x axis, where J_{ac} is the sheet current density.

Since the microbridge is in the Meissner state, the distribution of the applied transport current across the width $w = 8$ μm of the bridge is given by $J(x) = I/\left(\pi\sqrt{(w/2)^2 - x^2}\right)$, where I is the total applied current [66]. Because our vortex is essentially in the center of the bridge ($x = 0$), the sheet current density is $J(0) = 2I/\pi w$ and varies by less than 1% over the range of ± 0.5 μm that the vortex moves during the experiment. For $I = 1$ mA the sheet current density in the center of the bridge is $J(0) = 79.6$ A/m and it exerts a driving force of $F = 165$ fN on the vortex.

On the same note, it is also worth mentioning we applied a field of $B_a = 0.3$ mT perpendicular to the bridge. This field induces a Meissner sheet current density of $J(x) = -B_a x/\left(2\mu_0\pi\sqrt{(w/2)^2 - x^2}\right)$ which is zero in the center of the bridge and reaches $J = 4.8$ A/m and $F = 9.9$ fN at the maximum vortex displacement of about 0.5 μm from the center.

This dc force pushing the vortex towards the center of the bridge is negligible compared to our applied dc force. It can be readily incorporated into the calculations but was neglected for simplicity.

The weak F_{ac} results in a small oscillation of the vortex around its equilibrium position with typical amplitude of 1 nm, much smaller than ξ. The scanning SOT microscope simultaneously measures the distributions of the dc magnetic field $B_{dc}(x, y)$ and of the ac field $B_{ac}(x, y)$ at the driving frequency measured by a lock-in amplifier (Figures 12a and 12b). For small displacements of the vortex (in respect to the vortex dc signal spatial size) the two fields are related by

$$B_{ac} = -x_{ac}\frac{\partial B_{dc}}{\partial x} - y_{ac}\frac{\partial B_{dc}}{\partial y}.$$

Using this relation, we measured the ac displacements x_{ac} and y_{ac} of the vortex along the x and y axes as outlined in Figures 12c-g.

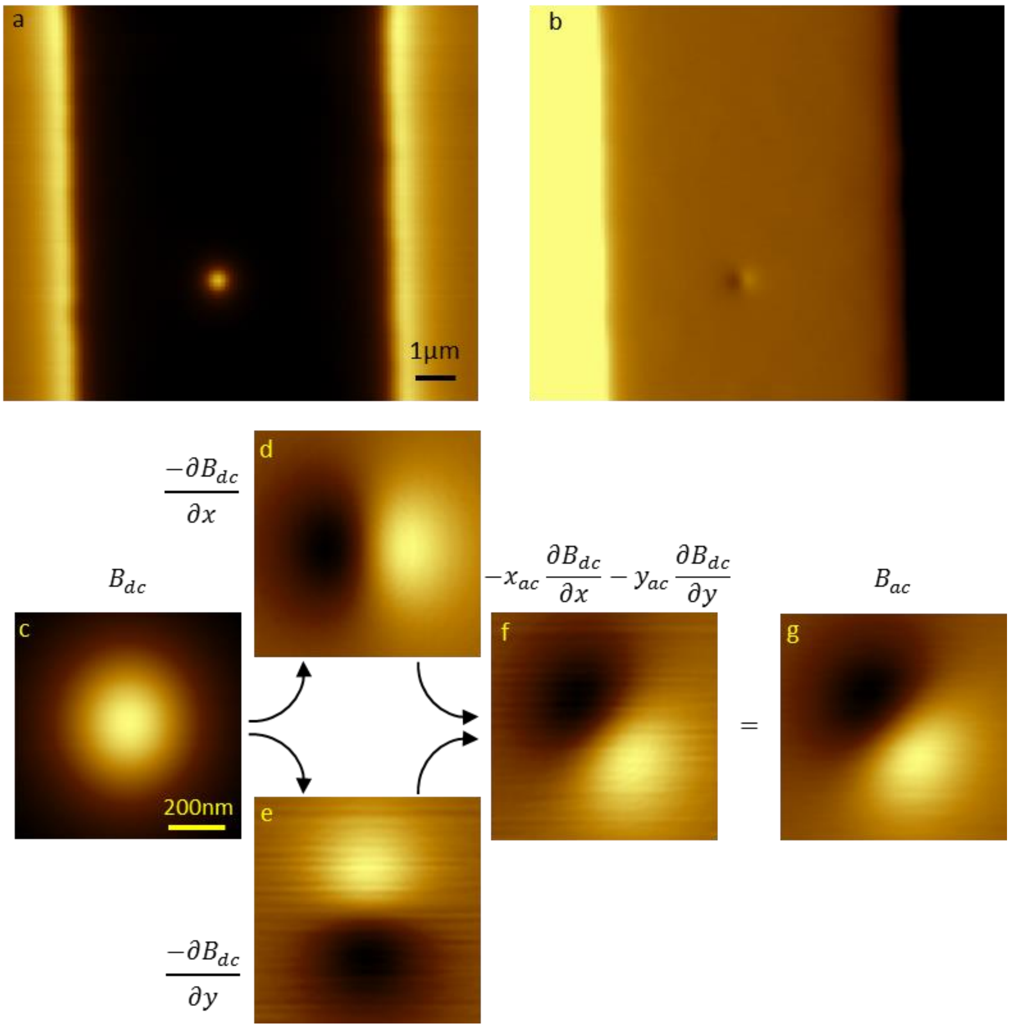

Figure 12. Magnetic imaging of a single vortex.

a. Scanning SQUID-on-tip image of $B_{dc}(x, y)$ showing a single vortex (bright) in a thin Pb film patterned into an 8 µm wide microbridge at $T = 4.2$ K. The microbridge is in the Meissner state (dark), and the enhanced field outside the edges (bright) is due to the screening of the applied field of 0.3 mT. b. Scanning image of $B_{ac}(x, y)$ acquired simultaneously with (a) showing the vortex response to an ac current of $I_{ac} = 0.94$ mA peak-to-peak (ptp) at 13.3 kHz applied to the microbridge. The Meissner response is visible along the microbridge ($B_{ac} = 0$, light brown) with positive (negative) B_{ac} outside the left (right) edge due to the field self-induced by I_{ac}. c. A zoomed-in image of the measured $B_{dc}(x, y)$ of a vortex. d - f. Numerically derived $\partial B_{dc}/\partial x$, $\partial B_{dc}/\partial y$ and $-x_{ac}\,\partial B_{dc}/\partial x - y_{ac}\,\partial B_{dc}/\partial y$ with $x_{ac} = 1.6$ nm and $y_{ac} = -1.9$ nm values obtained by a fit to (g). g. Experimentally measured $B_{ac}(x, y)$ of the vortex driven by I_{ac} acquired simultaneously with (c).

The sensitivity of the measurement of x_{ac} and y_{ac} using the procedure described in Figure 12 is determined mainly by the very high magnetic flux sensitivity of the SOT rather than by its physical size (provided it is sufficiently small to resolve the vortex). As a result, although an SOT with a diameter of 177 nm was used in the measurement, displacements with sub-angstrom precision could be obtained. If the vortex ac displacement is mainly along the x direction, there is no need to take a full 2D image, and a single line scan measurement through the center of the vortex is sufficient to determine the displacement x_{ac}. Figure 13a shows such a measurement of x_{ac} as a function of the excitation force F_{ac}, resolving displacements as low as 10 pm.

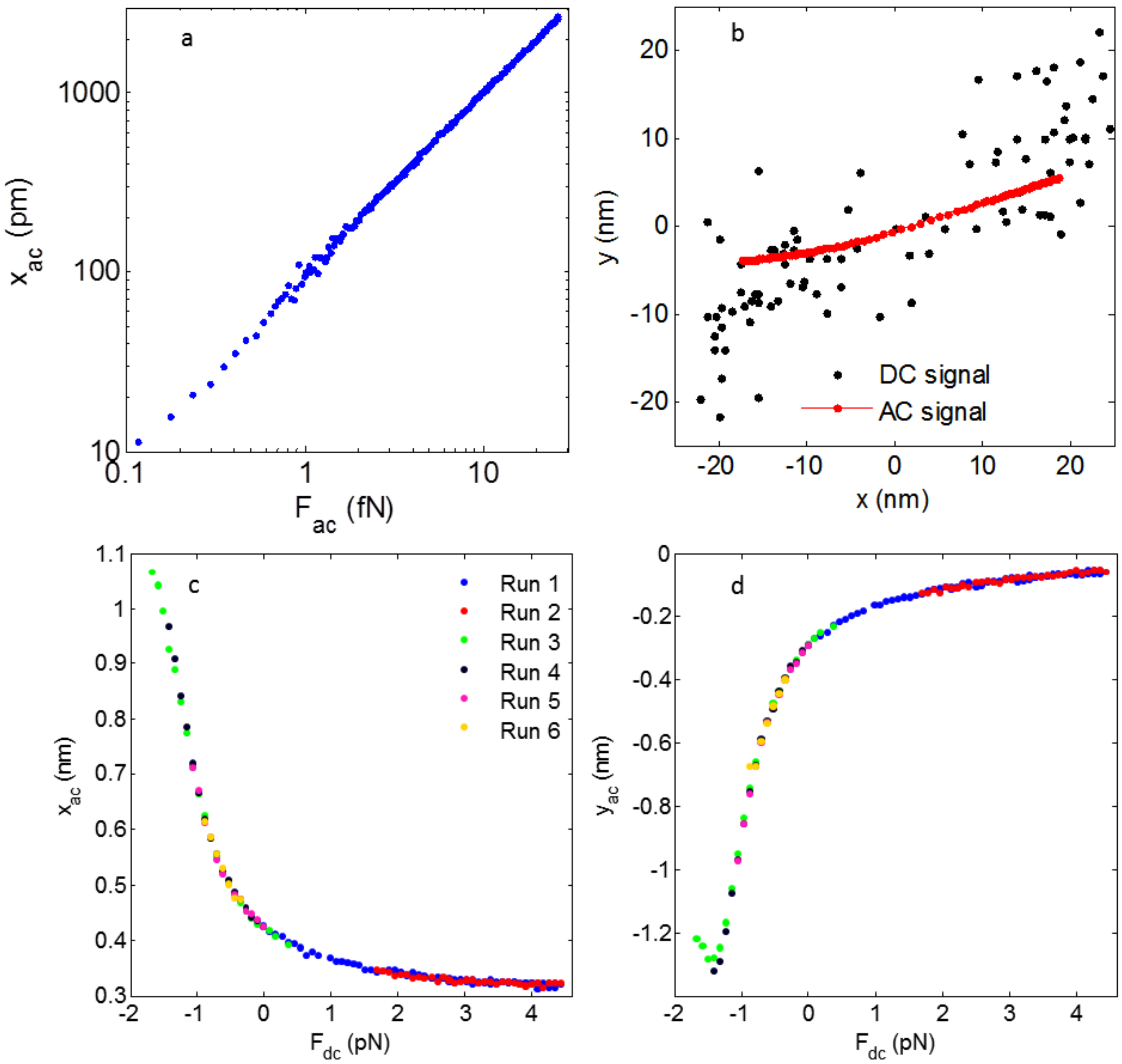

Figure 13. Sensitivity of vortex displacement measurements.

a, Measured vortex displacement x_{ac} as a function of the ac driving force F_{ac}. The measurement demonstrates the ability to resolve displacements as small as 10 pm. The time constant of the LIA was 10 ms for F_{ac}> 1 fN and up to 300 ms at lower drive amplitudes. b, Vortex trajectory within well 4 upon varying F_{dc}. The two data sets were extracted from the same experimental run using two methods: the DC signal was derived from the peak position of the B_{dc} image at each F_{dc}, and the AC signal was derived by integration of x_{ac} as described in the main text. c and d, x_{ac} and y_{ac} as a function of F_{dc} within well 5. The data were acquired in six different runs at different times yet the extracted displacements show remarkable consistency. The ac driving force was $F_{ac} = 88.9$ fN.

By adding a dc current I_{dc}, a driving force $F_{dc} = \Phi_0 J_{dc}$ is exerted that tilts the potential and shifts the vortex equilibrium position. By changing F_{dc} in small steps, we are able to reconstruct the full vortex ac response $x_{ac}(F_{dc})$ and $y_{ac}(F_{dc})$ along the potential well. If the vortex oscillates within a potential well without hopping to neighboring wells, dissipation is negligible and x_{ac} and y_{ac} are in-phase with I_{ac}.

In the absence of current, the vortex is located at the minimum of $U(r)$ at $x_m(0) \equiv 0$. A dc driving force $F_{dc} = \Phi_0 J_{dc}$ tilts the potential, $U_f(x) = U(x) - F_{dc}x$, displacing the vortex to a new minimum at $x_m(F_{dc})$, where the driving force is balanced by the restoring force, $F_r = -F_{dc} = -\,dU/dx|_{x_m}$ (Figure 14c). In our experiment, we measure the ac displacement of the vortex $x_{ac}(F_{dc}) = -F_{ac}/\left(\partial F_r/\partial x\,|_{x_m}\right) = F_{ac}/\left(\partial^2 U/\partial x^2|_{x_m}\right)$ which is inversely proportional to the pinning spring constant, $k = \partial^2 U/\partial x^2$. By sweeping the driving force F_{dc} and integrating over x_{ac}, the x position of the vortex $x_m(F_{dc}) = \int (dx/dF)\,dF_{dc} = \int (x_{ac}/F_{ac})\,dF_{dc}$ and the shape of the restoring force $F_r(x) = -F_{dc}(x_m)$ are obtained. Combining these results with the corresponding integration over y_{ac} yields the full vortex trajectory $y_m(F_{dc})$ vs. $x_m(F_{dc})$ within the well, while integrating over the driving force, $U(x) = \int F_{dc}(x)dx$, yields the single-well pinning potential

Since we measure both B_{dc} and B_{ac} images at each F_{dc} value, the vortex displacement and the trajectory could, in principle, also be derived from the B_{dc} image by tracing the position of the maximum field using data interpolation. This method, however, is much less sensitive since it depends on the pixel size of the image and on the size of the SOT, and since it is strongly influenced by thermal drifts in the microscope. The ac method, in contrast, is immune to the drifts and can resolve displacements that are some three orders of magnitude smaller than the pixel size. Figure 13b shows a comparison between the two methods demonstrating the advantage of the ac method. Note that the pixel size in the set of scans from which the trajectories were extracted was 10×10 nm^2, so the entire vortex travel range is just about 5 pixels.

As a final remark and in order to demonstrate the reproducibility of the measurement, Figure 13c and Figure 13d show six independent runs of measurements of the ac displacements x_{ac} and y_{ac} in the same well. The data clearly shows the very high reproducibility and consistency of the measurements and of the derivation method.

Results

As a reference, let us start by analyzing the expected response of a vortex trapped in a single potential well modeled by the generic Lorentzian function [31, 63-65] $U(r) = -U_0/(1 + (r/\xi)^2)$, where r is the radial distance from a materials defect (Figure 14d). Depending on the nature and the size of the defect, the pinning energy U_0 is a fraction of the maximum superconducting condensation energy of the vortex core $U_p \cong H_c^2 \xi^2 d$ = 28.3 eV [31], where d = 75 nm is the film thickness, H_c(4.2 K) = 530 Oe is the thermodynamic critical field of Pb, and ξ(4.2 K) = 46.4 nm is derived from the measurement of the upper critical field $H_{c2} = \Phi_0/2\pi\xi^2$ (Figure 24).

As Figure 14a shows, the spring constant $k(x)$ is the stiffest in the center of the well and gradually softens towards the inflection points of $U(x)$ at $x_i = \pm\xi/\sqrt{3}$ so that $x_{ac}(F_{dc})$ progressively increases until the vortex hops out of the well. In an isotropic potential, $y_{ac} = 0$ and the vortex trajectory is a straight line (Figure 14b).

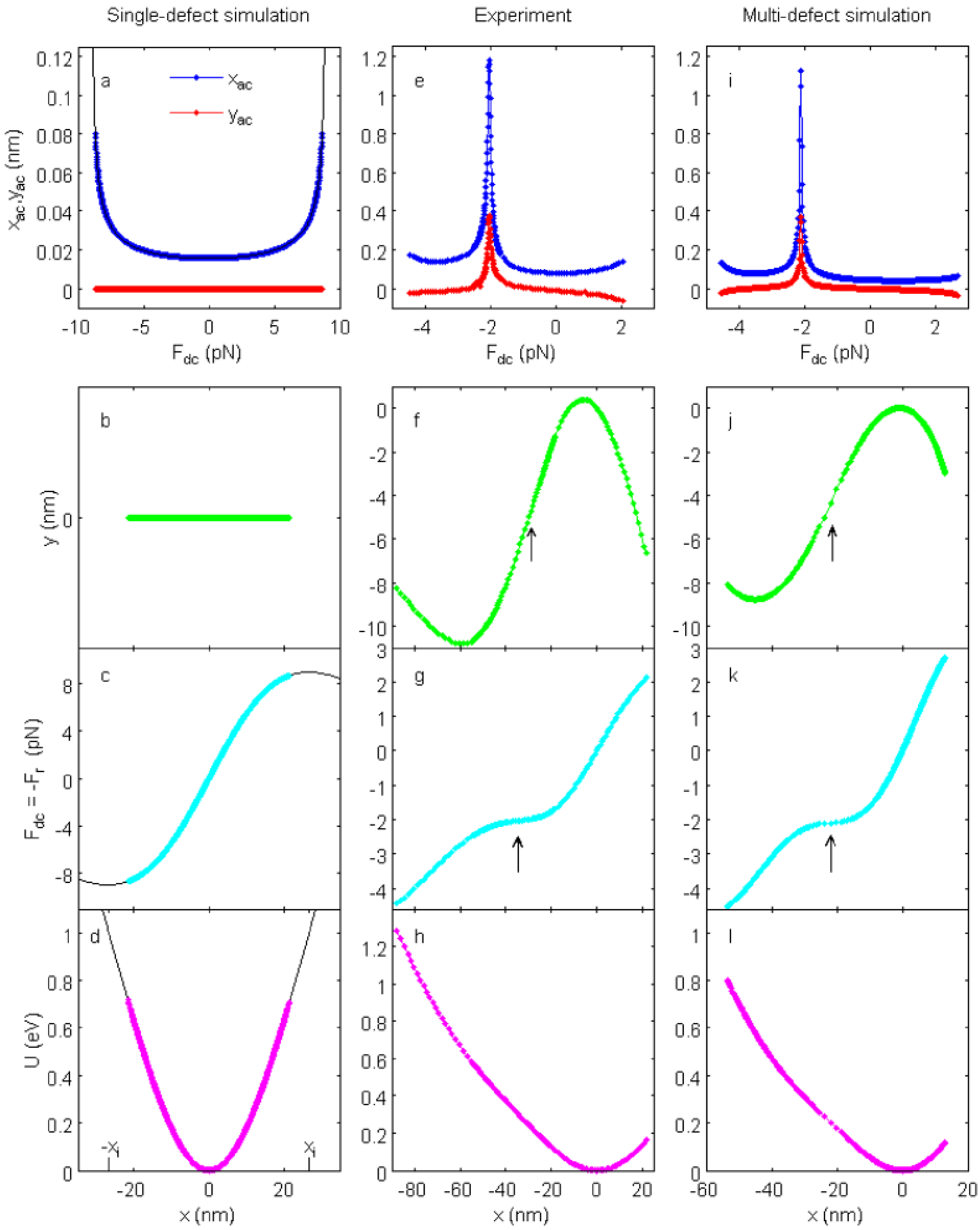

Figure 14. Vortex response and the structure of potential well 2 compared to simulations.

a-d, Calculated vortex response to $F_{ac} = 8.89$ fN in a potential well $U(r) = -U_0/(1 + (r/\xi)^2)$ due to a single defect with $U_0 = 4$ eV: a, vortex ac displacement x_{ac} and y_{ac}; b, vortex trajectory; c, restoring force; and d, the potential. The data points end where the activation barrier $\Delta U = 34k_BT$ (see detailed calculation in the "Rate of thermally-activated vortex jumps" appendix on page 62). e-h, Measured vortex response in well 2: e, displacements x_{ac} and y_{ac} in response to $F_{ac} = 8.89$ fN, displaying a large softening peak in the middle of the well; f, vortex trajectory with an 'S' shape; g, restoring force showing a pronounced inflection point; and h, the potential well. i-l, Calculated vortex response in a potential well due to a cluster of four defects (see Figure 5a for locations of defects): i, ac vortex displacement; j, vortex trajectory; k, restoring force; and l, the potential. The data points end where $\Delta U = 34k_BT$.

Figure 14e shows the ac displacements $x_{ac}(F_{dc})$ and $y_{ac}(F_{dc})$ measured for one of the studied potential wells (well 2, see Figure 15). Following the procedure described in the methods section, we derive the vortex trajectory within the well (Figure 14f), the restoring force (Figure 14g), and the single-well pinning potential $U(x) = \int F_{dc}(x)dx$ (Figure 14h). Figure 15 shows a compilation of similar results for different potential wells. Figure 17 shows an additional set of measured wells, displaying very similar properties. These data reveal the following features of vortex response that are strikingly different from the expected behavior shown in Figures 14a-d. (*i*) *Spring softening in the middle of the well*. In contrast to Figure 14a, which shows the highest stiffness in the center of the well, Figure 14e reveals a large and sharp peak in x_{ac}, which implies a small k and an inflection point in the restoring force in the central region of the well, shown by the arrow in Figure 14g. This intriguing feature turned out to be ubiquitous, and various degrees of softening in the middle of the wells were found in the majority of pinning sites as illustrated by Figures 15b and 17d. (*ii*) *Broken-spring phenomenon*. The ac response $x_{ac}(F_{dc})$ is expected to increase progressively towards the edges of the well and diverge at the inflection point of $U(x)$ due to the vanishing spring constant $k(x)$ at the maximum restoring force (Figures 14a and 14c). Surprisingly, Figure 14e shows only a small increase in x_{ac} towards the well edges, where the restoring force (Figure 14g) exhibits hardly any rounding at its maximum values. This response resembles the abrupt breaking of an elastic spring. (*iii*) *Anisotropy*. In an isotropic well, the vortex moves only in the direction of the driving force (Figures 14a and 14b). However, Figure 14e shows that the vortex also has a significant transverse ac displacement y_{ac} and a substantial y component in the trajectory (Figure 14f). Analysis of different wells has shown that the vortex may move at angles as large as 77° with respect to the direction of the driving force (see Figures 15a and 17c). (*iv*) *Asymmetry and internal structure*. Figures 15c and 17e show that most of the potential wells are asymmetric with respect to the positive and negative driving force and exhibit significant deviations from the model function $U(r) = -U_0/(1 + (r/\xi)^2)$. In Figure 14h, for example, the well is nearly parabolic at the bottom but has a linear intermediate section that again becomes parabolic at larger negative displacements. Even though the wells appear to be smooth on the scale of ξ, they have an internal structure that results in nontrivial shapes of the restoring forces and intricate trajectories of vortices in the individual wells (Figures 15a-b and 17c-d). Also, a point defect results in a well of width $\sim 2\xi/\sqrt{3} \cong 53$ nm between the inflection points, while many of the observed wells are significantly wider, reaching 110 nm (Figures 15c and 17e). (*v*) *Correlation between softening and the inflection point in the trajectory*. We also observed an intriguing correlation between the position of the softening point of the potential, which is the inflection point in the restoring force, and the position of the inflection point in the trajectory, as marked by arrows in Figures 14f and 14g. This correlation gives an important clue to the internal structure of the pinning potential and the dynamics of vortices, as described below.

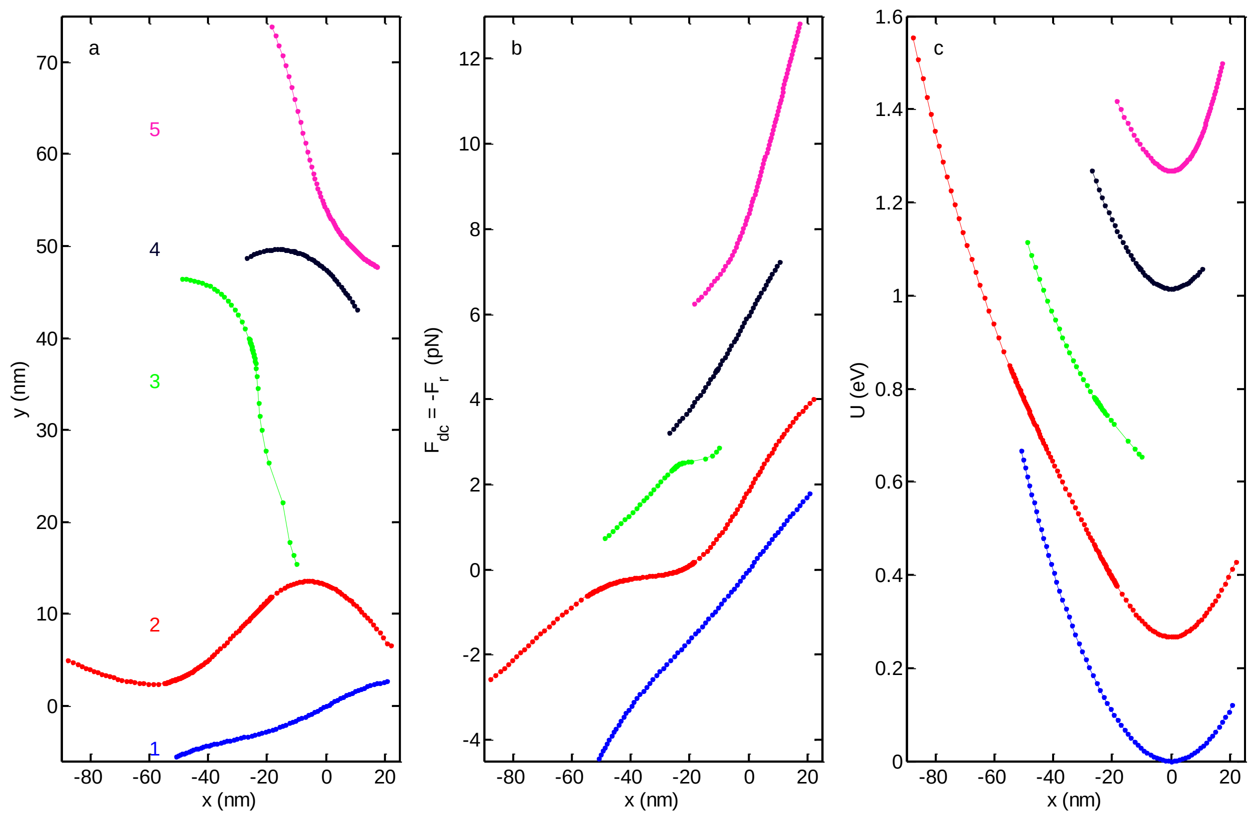

Figure 15. Comparison of different potential wells.

a, Vortex trajectories in wells 1 to 5, shifted vertically for clarity. $x = 0$ corresponds to the rest position of the vortex at $F_{dc} = 0$, except for the metastable well 3 that does not exist at $F_{dc} = 0$ (see Figure 4b). All the wells display nontrivial internal structure. b, The restoring force $F_{dc} = -F_r(x)$ of the different wells shifted vertically for clarity. $x = 0$ corresponds to $F_{dc} = 0$ for each well except well 3. c, The structure of the potential of the different wells shifted for clarity.

We now examine vortex dynamics on larger scales that include several pinning wells. We sweep F_{dc} up and down and at each step we acquire a full image of $B_{dc}(x,y)$ and $B_{ac}(x,y)$ at a constant F_{ac}, compiling a movie of the ac response. An example movie can be found at

www.weizmann.ac.il/condmat/superc/Scanning_SQUID-On-Tip_movies_of_vortex_dynamics.html

While sweeping F_{dc} up and down, the vortex moves in a closed trajectory which includes several wells. Figures 16e-j show a few frames of $B_{ac}(x,y)$ from one of the movies. $B_{ac}(x,y)$ shows significant variations in the intensity and the orientation of the dipole-like signal, reflecting the changes in both amplitude and direction of the ac displacement of the vortex within a single well.

If F_{dc} exceeds the maximum restoring force of a well, the vortex jumps to a different well, manifesting as an instantaneous displacement of the dipole in the movie. By recording the ac displacements in the wells and the jumps between the wells, a full map of closed loops of vortex trajectories was obtained, as shown in Figure 16a (and an additional example in Figure 17a). The corresponding plot of the restoring force is shown in Figure 16b (and Figure 17b). Figure 16b shows that the vortex resides in well 1 at large negative values of F_{dc}. As the applied force exceeds the maximum restoring force, the vortex may jump all the way to well 5, where it stays up to our maximum $F_{dc} = 4.44$ pN. As F_{dc} is decreased, the vortex undergoes a sequence of jumps to wells 4, 3, 2, and eventually back to 1. While the trajectory of the vortex within a well is reversible, the transition between the wells is hysteretic. Thus, to explore all possible intermediate trajectories and transitions, sub-loop sweeps of F_{dc} were performed. Analysis of the data from repeated sweeps leads to the following additional conclusions about the interaction of vortices with pinning wells: (*vi*) *Hopping distance and direction*. While the size of the individual wells is typically (1-2)ξ, the hopping distance between the wells is usually significantly larger, up to 20ξ. The vortex jumps between wells often have large transverse components with respect to the direction of the Lorentz force, as seen in Figure 16a (and Figure 17a). The hopping between wells 3 and 4, for example, occurs at an angle of roughly 70° with respect to F_{dc}. (*vii*) *Metastable wells*. Some minima in the pinning potential only appear at a finite dc Lorentz force. For example, well 3 in Figure 16b exists only at negative F_{dc} and well 6 exists only at positive F_{dc}. Moreover, Figure 16b shows that the vortex jumps from well 3 to well 4 in the positive x direction even though the driving force is negative (green dashed line); that is, the vortex moves against the Lorentz force. (viii) "*Nondeterministic*" *hopping*. Upon repeating the loops several times, we find that vortex jumps between the wells show significant variability. For example, the force F_{dc} at which the vortex jumps from well 5 to well 4 is quite different for different dc current sweeps (dashed magenta lines in Figure 16b). In addition, the vortex occasionally hops from well 5 directly to well 3 instead of well 4. Similarly, from well 4 the vortex may jump to wells 3, 2, or 1, while from well 3 it may jump to wells 2 or 1.

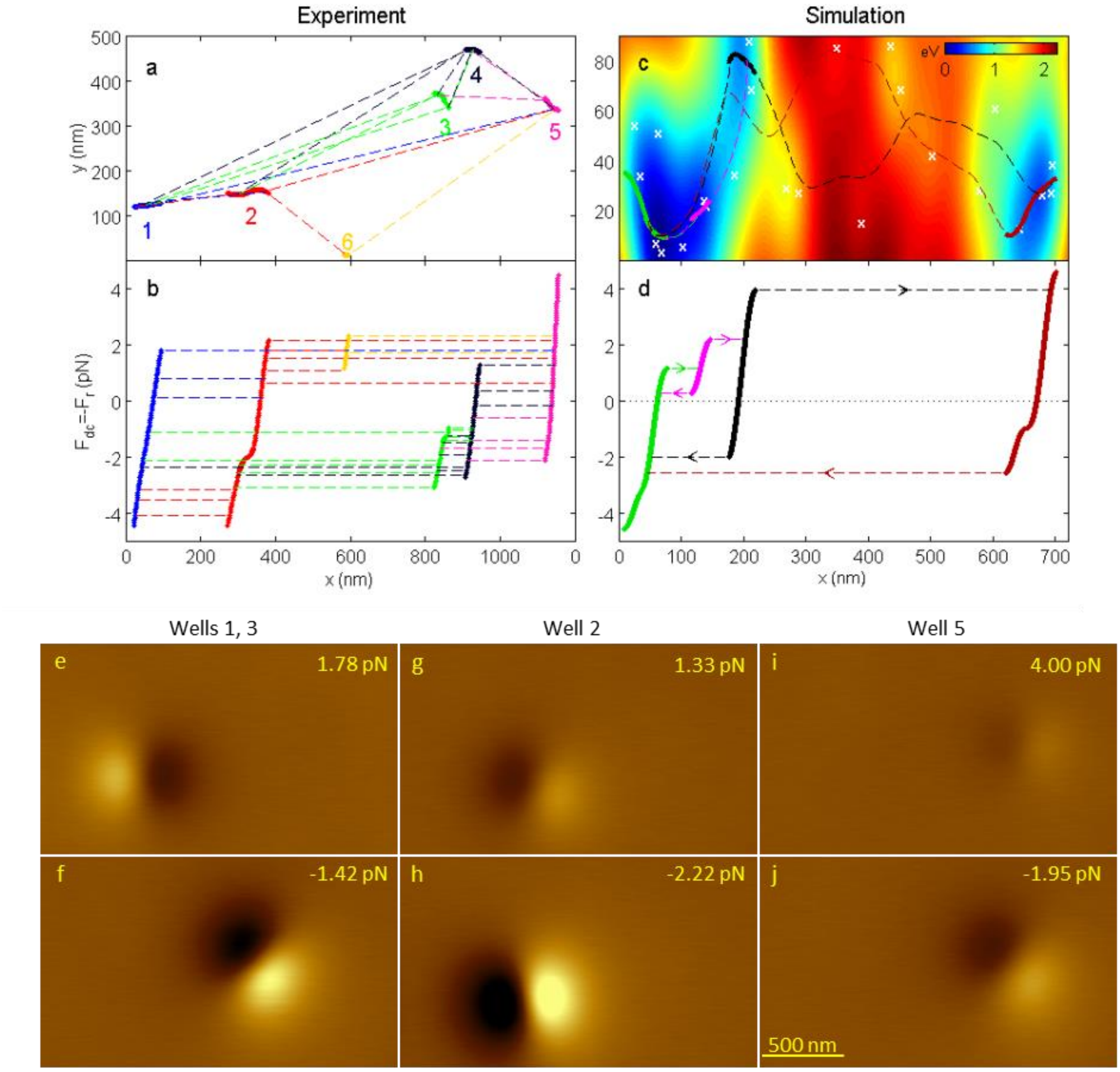

Figure 16. Vortex hopping between wells.

a, Vortex trajectories in wells 1 to 6 (solid symbols) and hopping events between the wells shown schematically by dashed lines with a color matching the original well. The hopping between the wells results in hysteretic closed-loop trajectories that vary upon repeated cycles of the full loop and of the sub-loops. b, The restoring force of the wells $F_{dc} = -F_r(x)$ with the hopping events (dashed lines with a color matching the original well). The vortex jumps to the right (left) when a positive (negative) applied force exceeds the restoring force. The vortex stops at a position where the restoring force of the new well equals the applied force (dashed lines are horizontal). Well 6 exists only at positive forces and well 3 only at negative forces. The jumps to the right from well 3 to well 4 occur against the direction of the driving force when the value of the applied force drops below the minimum restoring force of well 3. c, 2D potential due to a random distribution of defects, marked by ×, of equal $U_0 = 0.66$ eV and average density of 200 μm^{-2}. The stationary trajectories upon tilting the potential are shown by the solid lines and the dynamic escape trajectories by dashed lines with colors matching the source well. e-j, Selected $B_{ac}(x,y)$ images of the ac vortex response to $F_{ac} = 93.1$ fN ptp in different wells at the indicated values of F_{dc}. The false color scale spans 20 μT in all images. The full movie can be found at www.weizmann.ac.il/condmat/superc/Scanning_SQUID-On-Tip_movies_of_vortex_dynamics.html

Numerous sets of pinning wells were measured as part of this work. Here I present an additional example of a closed-loop trajectory comprising four potential wells. Figures 17a and 17b show a full map of the closed loop vortex trajectories and their corresponding restoring forces. Figures 17c-e show a comparison between the trajectories within each well, the restoring forces, and the potential structures.

Notice that the features discussed above also appear in this set, including the non-trivial trajectories and anisotropy of the wells, inflection points of the restoring force away from the edges, the broken spring effect, the non-deterministic hopping behavior, and the appearance of metastable wells.

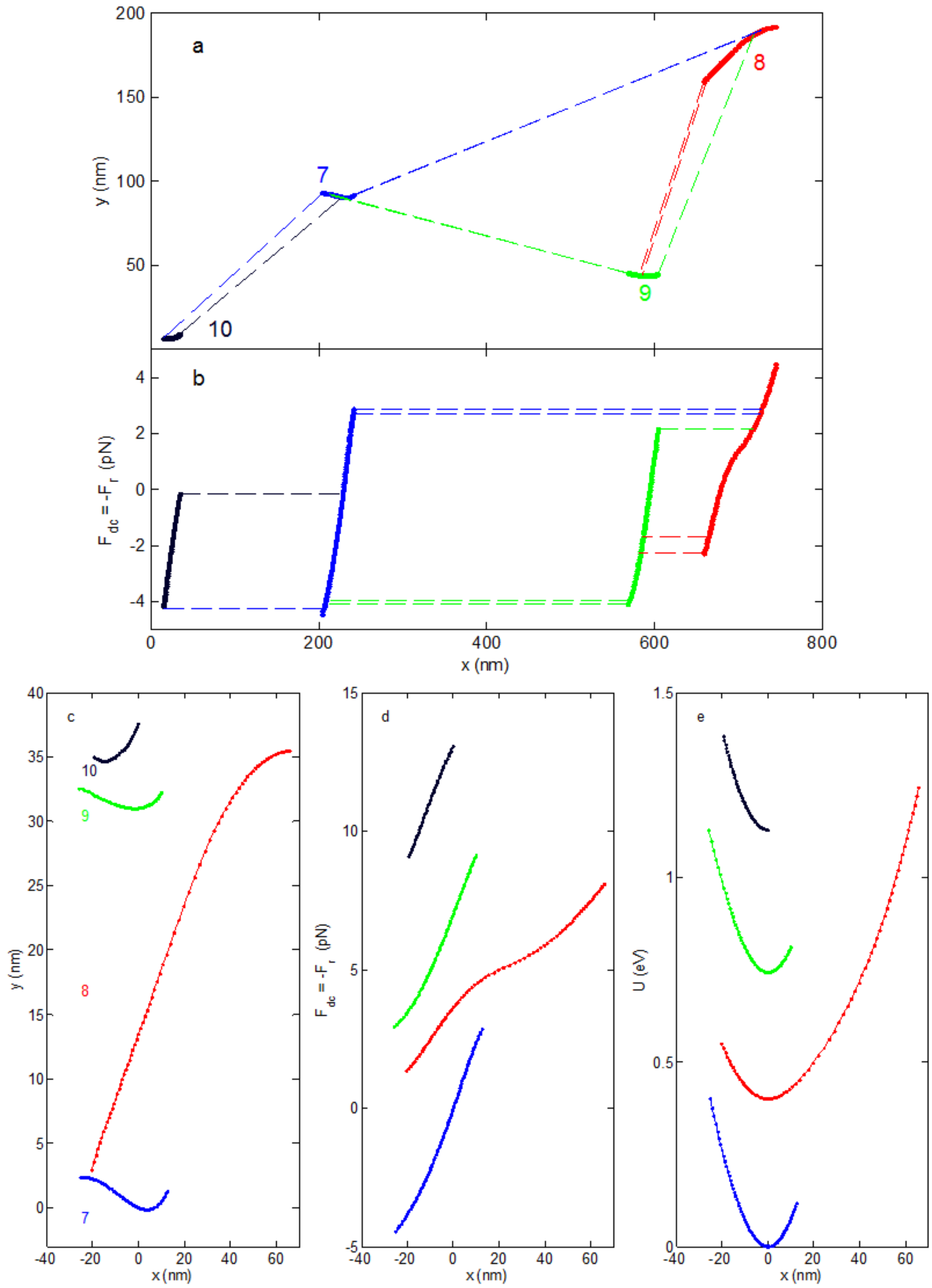

Figure 17. Additional set of potential wells

a, Closed loop trajectory with vortex trajectories in wells 7 to 10 (solid symbols) and hopping events between the wells (shown schematically as dashed lines with a color matching the original well). The hopping between the wells results in hysteretic closed-loop trajectories that vary upon repeated different cycles of the full loop and of the sub-loops. b, The restoring force of the wells $F_{dc} = -F_r(x)$ with hopping events shown schematically (dashed lines with a color matching the original well). The vortex jumps to the right (left) when a positive (negative) applied force exceeds the restoring force. The vortex stops at a position where the restoring force of the new well equals the applied force (horizontal dashed lines). Well 7 is metastable and exists only at negative forces. c-e, Comparison of the potential wells c, Vortex trajectories in wells 7 to 10, shifted vertically for clarity. $x = 0$ corresponds to the resting position of the vortex at $F_{dc} = 0$, except for well 7 which does not exist at $F_{dc} = 0$. All the wells display nontrivial internal structure. d, The restoring force $F_{dc} = -F_r$ of the different wells shifted vertically for clarity. $x = 0$ corresponds to $F_{dc} = 0$ for each well except well 4. e, The structure of the potential of the different wells, shifted for clarity.

Discussion

The above results clearly indicate that the observed vortex dynamics cannot be described by a sparse distribution of pinning centers that are well separated from each other. A single potential well simply cannot bring forth these behaviors.

At the inflection point of a potential well the restoring force reaches its maximum and the spring constant $k = \partial^2 U/dx^2$ vanishes, resulting in diverging softening and infinite x_{ac}. On approaching the critical force, the divergence may be cut off by thermal fluctuations when the activation barrier $\Delta U \cong 34\ k_B T$ (for our experimental situation. See calculation in the appendix on page 62). Figure 14a shows that for a potential well due to a single defect with U_0 of a few eV, x_{ac} increases gradually towards the well edges and reaches a value that is about five times larger than at the bottom of the well when $\Delta U \cong 34 k_B T$. Correspondingly, the restoring force flattens towards its extrema points (Figure 14c). In our experiment, this softening is much milder and x_{ac} increases usually by less than a factor of two (Figure 14e). The corresponding restoring force increases rather linearly with displacement and then vanishes quite abruptly with very little rounding, resembling the breaking of a spring (Figure 14g). This behavior is inconsistent with a potential due to a single defect.

We have conducted detailed numerical investigation of disorder to show that the vortex response changes drastically if potential wells of numerous defects overlap. We start with two defects separated by a distance $\Delta x > 2\xi/\sqrt{3}$. These form two distinct potential wells separated by a barrier (Figure 19a). However, at smaller separations, $\xi/2 \lesssim \Delta x < 2\xi/\sqrt{3}$, an interesting situation occurs in which the two defects form a single potential well, but $U(x)$ develops an intrinsic softening and an inflection point in the restoring force leading to a peak in x_{ac} in the center of the well, as shown in Figure 18a-c. The softening occurs where the attractive forces of the two defects balance each other. For two identical defects, the softening occurs exactly in the center, leading to a U-shaped potential well.

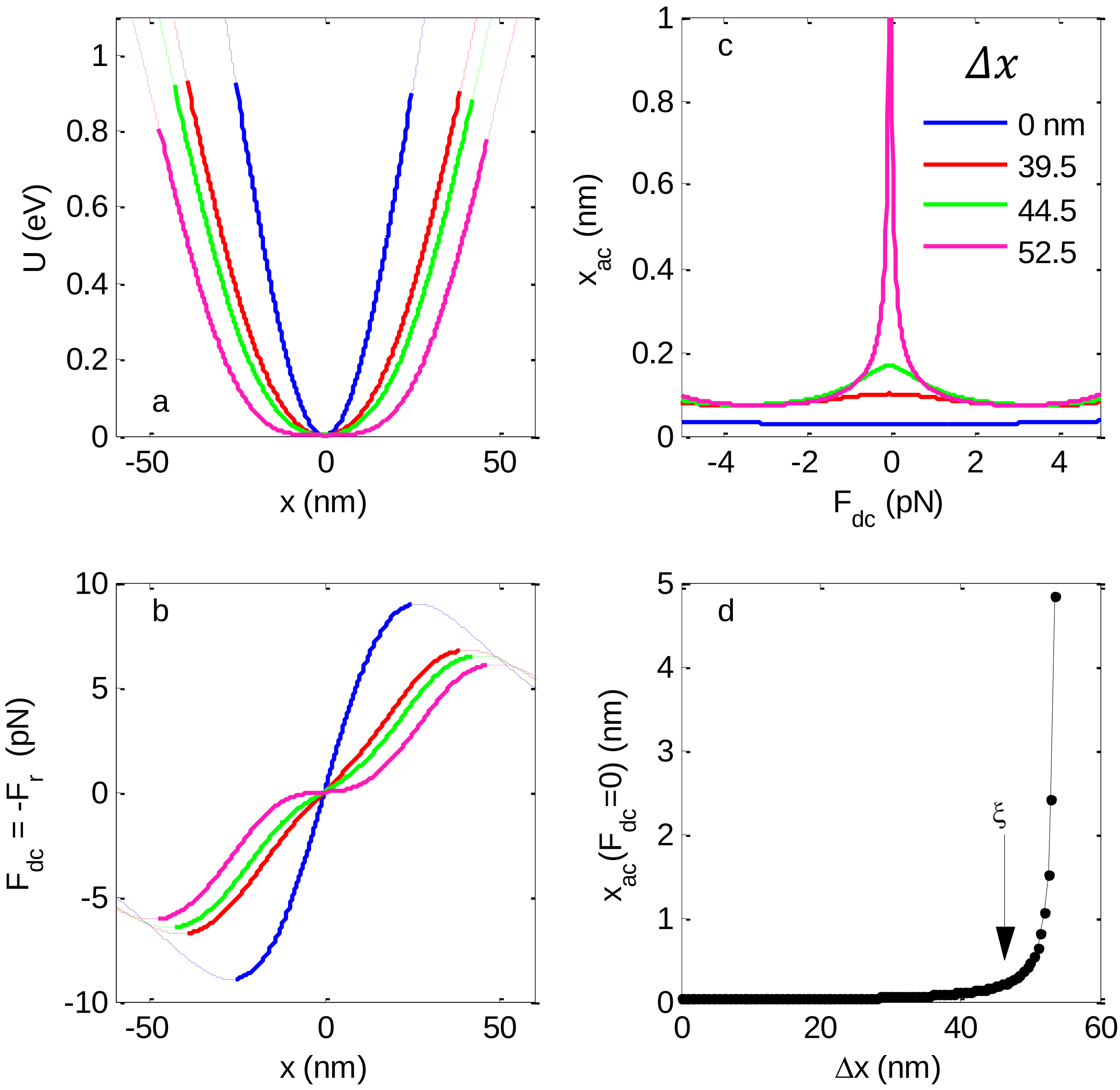

Figure 18. Potential structure and vortex response in the case of two close defects.

The case of two defects separated by $\Delta x < 2\xi/\sqrt{3}$. a, $U(x)$ due to two defects, each contributing a Lorentzian potential with $U_0 = 2$ eV and $\xi = 46.4$ nm for four values of separation Δx between the defects, ranging from 0 nm to 52.5 nm. U_0 was set to 0 eV for clarity. With increasing Δx, the potential gradually changes into a U shape, resulting in a reduction of the spring constant in the center of the well. The solid lines end at the inflection points of the potential. b, The corresponding restoring force $F_{dc} = \partial U/\partial x$ showing the development of an inflection point in the center of the well. c, Corresponding ac displacement x_{ac} due to $F_{ac} = 16.5$ fN showing the development of large softening in the center of the well. d, Dependence of x_{ac} at the softening point in the center of the well as a function of the separation Δx between the defects. The softening diverges on approaching $\Delta x = 2\xi/\sqrt{3} = 53.6$ nm for the case of a Lorentzian potential.

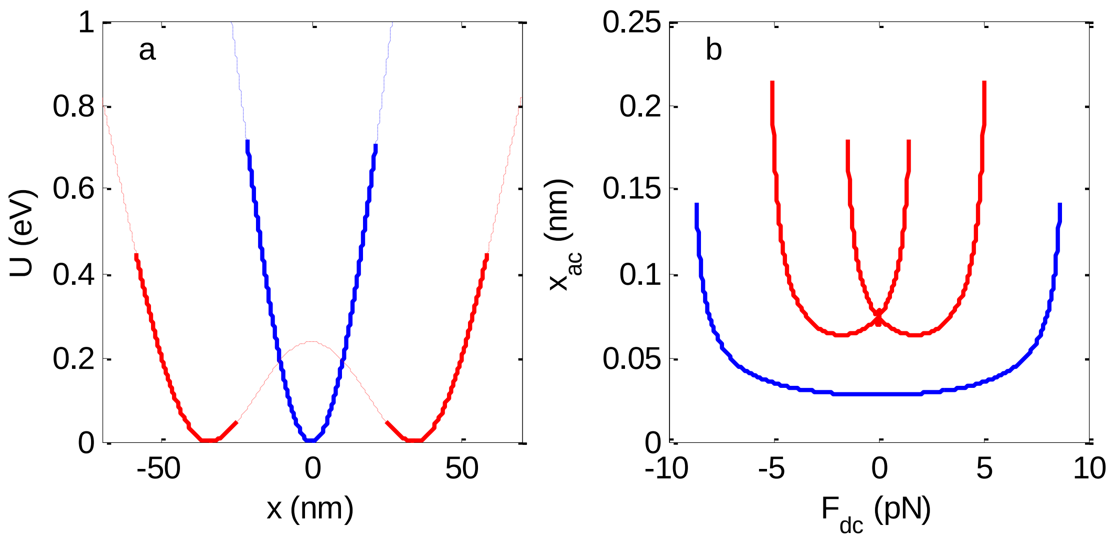

Figure 19. Potential structure and vortex response in the case of two defects.

a, $U(x)$ due to two defects with $U_0 = 2$ eV when the two defects overlap and form a single well (blue) and when the defects are separated by $\Delta x = 80$ nm and form two nearby wells separated by a barrier comparable to our experimental situation (red). b, Vortex ac displacement x_{ac} due to $F_{ac} =$ 16.5 fN for the two cases showing similar softening near all the well edges and the absence of the broken-spring effect. The data points in (a) and (b) end where the activation barrier $\Delta U = 34$ k_BT.

Figure 19 shows that two defects alone cannot result in a broken-spring effect. In this case, when the defects are closer than $2\xi/\sqrt{3}$ a single well is formed with large softening in the center of the well (Figure 18), but the response near the edges of the well displays softening similar to that of the single defect case (not shown in Figure 18c for clarity). When the defects are separated by more than $2\xi/\sqrt{3}$, two separate wells are formed with a barrier between them. The outer edges of the well show softening as in the case of a single defect, while the softening on the inner sides of the two wells depends on the size of the barrier. For small barriers, thermal activation clearly leads to breaking of the spring between the two wells. However, this is not observed experimentally since the breaking of the spring is observed for large untilted barriers. When the distance between the two defects is increased to form a barrier that is comparable to the experimental situation, no substantial spring breaking is attained (Figure 19). Thus, although displaying a softening in the middle of the well, the presence of two nearby defects is insufficient to explain the observed broken-spring effect.

More generally, it can be shown that any combination of defects in 1D cannot lead to the broken-spring effect since the resulting $U(x)$ is always smooth on the scale of ξ. Surprisingly, we find that the situation is fundamentally different in 2D.

By analyzing a 2D cluster of four defects as shown in Figure 20, we can reproduce our results with startling agreement between the experimental and numerical results shown in Figures 14i-l:

1) The vortex displacement has a sharp spring softening peak in the middle of the well (Figure 14i) and a corresponding inflection point in the restoring force (Figure 14k).

2) The potential structure is substantially wider than ξ.

3) There is a significant anisotropy of the vortex response (Figure 14j) and asymmetry between positive and negative drives (Figure 14l). This anisotropic vortex response occurs here in a cluster of isotropic pinning defects, unlike the anisotropic depinning in a network of planar defects such as grain boundaries in polycrystals [64].

4) The trajectory has an S shape with an inflection point (arrow in Figure 14j) that clearly matches the location of the inflection point in the restoring force (arrow in Figure 14k), as we indeed observe experimentally.

At zero driving force, the four close defects form a single potential well with its minimum at the origin. The blue solid line in Figure 20b shows the resulting potential $U(x)$ along the line $y = 0$, parallel to the driving force and passing through the minimum of the untilted potential landscape. The corresponding restoring force $\partial U/\partial x$ (blue line in Figure 20c), is smooth and flattens out at its maximum and minimum values, similar to that of a single defect (Figure 14c). However, as the potential is tilted by the driving force, the vortex moves along an intricate 2D trajectory shown in Figure 20a. In particular, for a small positive F_{dc}, only one potential minimum (magenta dot in Figure 20e) and one saddle point (black dot) are present. At $F_{dc} = 1.04$ pN, however, a new metastable well appears with a new minimum and saddle point (light green and yellow dots in Figures 20f and 20g). This additional well produces a sharp ripple in the projection of the potential $U(x)$, and of the corresponding restoring force, onto the direction of the driving force (Figures 20b and 20c). Thus, in contrast to the common perception that the pinning potential of multiple defects is smooth on the scale of ξ, a multi-defect potential along the projection of the intricate vortex trajectory onto the direction of the Lorentz force can have sharp ripples on length scales substantially shorter than ξ. Because of these ripples, the restoring force terminates quite abruptly as F_{dc} approaches a narrow region near the end points of the magenta line in Figure 20c, giving rise to a broken-spring response. Interestingly, Figures 20a and 20c show that, upon exiting the central (magenta) well to the right, the vortex hops into the green metastable well, while, upon exiting to the left, the vortex escapes without passing through the red metastable well. Thus, the effects of the ripples persist even if the vortex does not actually hop into the metastable wells.

By performing numerical studies we find that the necessary condition for spring-breaking is that at least two nearby defects form a single central well that is broader than ξ and that the additional adjacent defects create ripples in this 2D potential. Three defects are sufficient for breaking the spring on one side of the well, while four or more defects are required for spring-breaking on both sides of the well (Figure 20).

Broken-spring behavior is usually associated with the so-called pin-breaking mechanism that results from bending distortions of a long vortex trapped by a strong pinning center [67-70]. In our case, however, bending distortions of the vortex are suppressed because the thickness of our film is smaller than the diameter of the non-superconducting core, $2^{3/2}\xi = $ 131 nm. A pinhole of radius $a > \xi$ with sharp boundaries can also result in a hysteretic pinning potential $U(x, y)$ with no reversible quadratic part at small displacements [71], which is inconsistent with our SOT data shown in Figure 14. Our numerical simulations of the Ginzburg-Landau equations (see the "Ginzburg-Landau simulations for strong pinning" appendix on page 65) for the case of strong pinning (due to $T_c(r)$ depression in a region of radius $a{\sim}\xi$ and smooth recovery over the length ${\sim}\xi$ at $r > a$) gave a potential well $U(r)$ similar to that shown in Figure 14d, including the softening of the spring constant at the inflection point (Figure 18). The simplifying assumption of a vortex in a rigid potential of multiple pinning wells therefore does not change the main conclusions of this work. As a result, our model of potential ripples in a 2D random potential formed by an array of overlapping single wells $U(r)$ is applicable to both weak and strong pinning and it presents a new mechanism for spring-breaking that describes our experimental data surprisingly well.

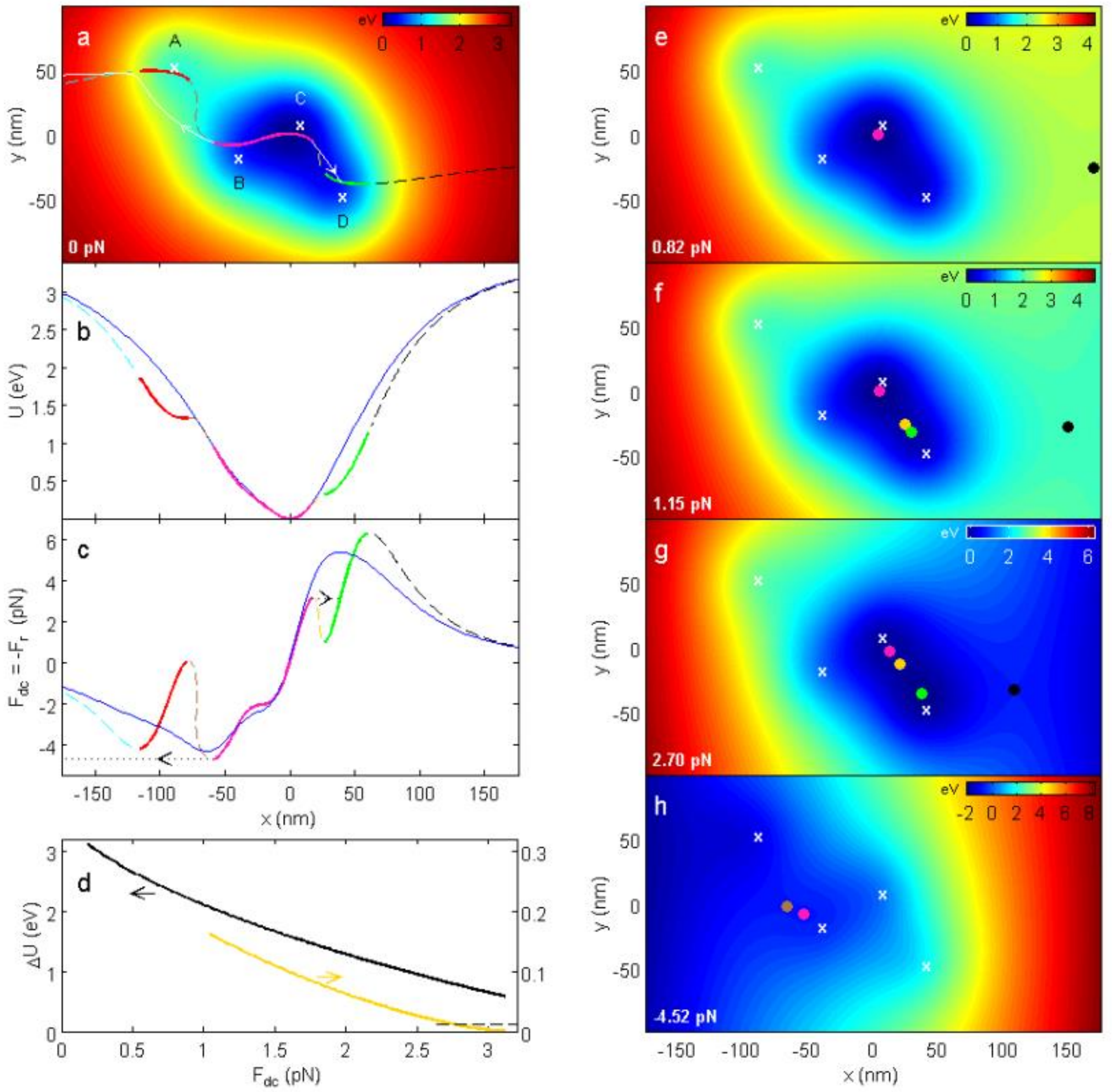

Figure 20. Simulation of vortex potential and dynamics in a multi-defect well.

a, Calculated 2D vortex potential at zero driving force due to a cluster of four point-defects at locations marked by × (defects A, B, C, and D contribute a Lorentzian potential with U_0 of 1.41, 1.41, 2.0, and 2.0 eV respectively). Overlayed is the calculated trajectory of the vortex upon varying the driving force F_{dc}: solid color lines – loci of static potential minima points; dashed lines – loci of inflection points; white solid lines – dynamic vortex escape paths out of the central well at positive and negative critical forces. An expanded view of the static trajectory in the central well is shown in Fig. 2j. b, $U(x)$ along the stationary vortex trajectory in (a) (color solid and dashed segments) as compared to $U(x)$ along the $y = 0$ line in (a) (solid blue). c, The corresponding restoring force $F_{dc} = -F_r = \partial U/\partial x$. The dashed lines (saddle points in (a)) are unstable solutions. The dotted lines show the escape of the vortex at the critical forces out of the central well. d, Black: activation barrier between the central minimum (magenta in (a)) and the main saddle point (dashed black in (a)) vs. F_{dc}. Yellow: activation barrier between the central minimum and the metastable saddle point (dashed yellow in (a)) that is formed at $F_{dc} > 1.04$ pN. The central minimum disappears for $F_{dc} > 3.1$ pN. The dashed line marks $\Delta U = 34k_BT = 12$ meV, at which thermal activation becomes relevant. e, 2D vortex potential at $F_{dc} = 0.82$ pN at which one minimum (magenta) and one saddle point (black) are present. f, 2D potential at $F_{dc} = 1.15$ pN at which two minima (magenta and light green) and two saddle points (yellow and black) are present. g, Same as (f) at $F_{dc} = 2.70$ pN. For $F_{dc} > 3.1$ pN, only the light green metastable minimum remains. h, 2D potential at $F_{dc} = -4.52$ pN, at which only the central minimum (magenta) and a nearby saddle point (brown) are present.

Another ingredient of the spring-breaking is thermal activation, which is usually disregarded for conventional superconductors at low temperatures [31,72]. Figure 20d shows that the typical energy barrier for thermally-activated hopping of vortices between the potential minimum and the main saddle point (black curve) is large ($\Delta U \cong U_0 \cong 1$ eV $\cong 104$ K) and decreases smoothly with F_{dc}. As a result, thermal activation at 4.2 K becomes relevant only within a few percent of the critical force F_c, at which $\Delta U(F_{dc}) \cong 34\ k_B T \cong 12$ meV (see appendix on page 62 for details). For a single defect, the spring constant at $F_c - F_{dc} \sim 10^{-2} F_c$ is reduced significantly, resulting in x_{ac} that is about five times larger than at the bottom of the well (Figures 14a and 19b) and inconsistent with the experimental data (Figure 14e). However, the metastable wells due to potential ripples create multiple saddle points separated by much smaller activation barriers (yellow line in Figure 20d) that can cause premature thermal activation of the vortex, facilitating the broken-spring effect (as shown in Figures 14k and 14i). At $J \sim J_c$, the heights of these metastable barriers depend weakly on F_{dc}, resulting in thermally-activated nondeterministic hopping of vortices over a wide range of applied currents, consistent with our experimental data.

A concern was raised whereas the interaction between the SOT and the vortex upon scanning might be the trigger for premature hopping. We can estimate the interaction force between the tip and the vortex as follows. In our geometry, we can approximate the SOT loop as a single segment of length $\Delta L = 177$ nm (equal to the SOT diameter) carrying current parallel to the sample. The current that flows in the segment is the current applied to the SOT, $I_{SOT} \cong I_c^{SOT} \cong 100\ \mu A$. The current through the segment is applied through two parallel wires perpendicular to the sample surface and carrying current in opposite directions; these are the leads to the SOT. These parallel leads, perpendicular to the sample plane, do not experience a net force in the vortex field, whereas the horizontal segment experiences an in-plane interaction force of $F_{int} = I_{SOT} \Delta L B_z$, where $B_z \cong 2$ mT is the typical field created by the vortex at the SOT location, as measured directly by the SOT. With the above parameters we obtain $F_{int} \cong 35$ fN. This dc force between the tip and the vortex is about two orders of magnitude smaller than the typical restoring force F_{dc} of a potential well and therefore should not affect our measurements. Although the interaction force is comparable to our typical $F_{ac} = 93.1$ fN, since it is dc, it should not influence the ac measurements.

In order to further test the possible influence of the tip, we have compared measurements of vortex hopping between two wells with and without scanning the SOT over the vortex. In the latter case, the SOT was stationary located away from both the wells, but not too far from the final well. When the vortex is located in the original well, it creates a very small B_z at the location of the SOT and hence no interaction force. When the vortex arrives at its final well, a small B_z increase is detected by the SOT. As a result, the hopping event can be observed without influencing the vortex at its original location. By sweeping F_{dc}, we have thus compared the hopping process with and without SOT scanning. The results showed no observable difference between the two procedures.

Based on the above insights, and to avoid "engineering" the potential landscape to fit our experimental findings, we performed a full analysis of a 2D potential comprising a random distribution of defects (see the “Numerical simulations” appendix on page 64 for details). Figure 16c shows the potential landscape and the resulting static vortex trajectories inside the wells, as well as the dynamic escape trajectories between the wells (dotted lines). The main features, including the extent of the wells, shape of the trajectories, metastable wells, typical hopping distances and the transverse displacement between the wells are in good qualitative agreement with the experimental results. In addition, the wells show the broken-spring effect and inflection points in the restoring force (Figure 16d) coinciding with the inflection points in the static trajectories.

Summary

In conclusion, the new scanning SQUID-on-tip microscopy enabled us, for the first time, to measure the fundamental dependence of the elementary pinning forces on vortex displacement. The totality of our experimental and computational results shows that a vortex typically interacts with small clusters of a few pinning defects separated by about the coherence length. At low currents, the random multi-scale pinning landscape results in complex vortex trajectories and unusual softening within the potential wells. On approaching the critical current, the 2D random configuration causes fragmentation of the potential into metastable wells and gives rise to sharp ripples in the restoring force, triggering abrupt thermally-activated depinning of vortices even in the case of strong pinning and low temperatures, for which no significant thermal relaxation is expected. These results provide new insights into the pinning of vortex matter, mechanisms of magnetic relaxation in superconductors at low temperatures, the nonlinear response of superconductors to strong alternating electromagnetic fields, and the development of high-critical-current conductors with artificial pinning nanostructures. This work may also open exciting opportunities in the controllable manipulation of single vortices on nanometer scales, particularly in quantum computations based on braiding and entanglement of vortices in thin film nanostructures.

Bibiliography

1. Gigorieva, I. V. Magnetic flux decoration of type-II superconductors, *Supercond. Sci. Technol.* **7** 161-176 (1994)
2. Williams H. J., Foster, F. G. and Wood, E. A. Observation of magnetic domains by the Kerr effect, *Phys. Rev.* **82,** 119 (1995)
3. Cohen, M. S. Magnetic measurements with Lorentz microscopy, *IEEE Trans. On Magnetics* **1** 156-167 (1965)
4. Kirtley, J. R. Fundamental studies of superconductors using scanning magnetic imaging, *Rep. Prog. Phys.* **73**, 126501 (2010)
5. Finkler, A., Segev, Y., Myasoedov, Y., Rappaport, M. L., Ne'eman, L., Vasyukov, D., Zeldov, E., Huber, M. E., Martin, J. & Yacoby, A. Self-aligned nanoscale SQUID on a tip. *Nano Lett.* **10**, 1046-1049 (2010)
6. Finkler, A., Vasyukov, D., Segev, Y., Ne'eman, L., Lachman, E. O., Rappaport, M L., Myasoedov, Y., Zeldov, E. & Huber M. E. Scanning superconducting quantum interference device on a tip for magnetic imaging of nanoscale phenomena. *Rev. Sci. Instrum.* **83**, 073702 (2012)
7. Tinkham, M. *Introduction to Superconductivity*. Dover Publications, Inc., 2 edition, (1996).
8. Clarke, J. and Braginski, A. I. *The SQUID handbook: Fundementals and Technology of SQUIDs and SQUID Systems*. Wiley-VCH, (2004).
9. Cleuziou, J.-P., Wernsdorfer, W., Bouchiat, V., Ondarçuhu, T. & Monthioux, M. Carbon nanotube superconducting quantum interference device. *Nat. Nanotechnol.* **1**, 53-59 (2006).
10. Koshnick, N. C., Huber, M. E., Bert, J. A., Hicks, C. W., Large, J., Edwards, H. & Moler, K. A. A terraced scanning superconducting quantum interference device susceptometer with submicron pickup loops. *Appl. Phys. Lett*. **93**, 243101 (2008).
11. Nagel, J., Kieler, O. F., Weimann, T., Wölbing, R., Kohlmann, J., Zorin, A. B., Kleiner, R., Koelle, D. & Kemmler, M. Superconducting quantum interference devices with submicron Nb/HfTi/Nb junctions for investigation of small magnetic particles. *Appl. Phys. Lett*. **99**, 032506 (2011).
12. Veauvy, C., Hasselbach, K. & Mailly, D. Scanning µ-superconduction quantum interference device force microscope. *Rev. Sci. Inst.* **73**, 3825-3830 (2002).
13. Foley, C. P. & Hilgenkamp, H. Why nanoSQUIDs are important: an introduction to the focus issue. *Supercond. Sci. Technol.* **22**, 064001 (2009).
14. Troeman, A. G. P., Derking, H., Borger, B., Pleikies, J., Veldhuis, D. & Hilgenkamp, H. NanoSQUIDs based on niobium constrictions. *Nano Lett.* **7**, 2152- 2156 (2007).
15. Hao, L., Macfarlane, J. C., Gallop, J. C., Cox, D., Beyer, J., Drung, D. & Schurig, T. Measurement and noise performance of nano-superconducting-quantum-interference devices fabricated by focused ion beam. *Appl. Phys. Lett.* **92**, 192507 (2008).
16. Vasyukov, D., Anahory, Y., Embon, L., Halbertal, D., Cuppens, J., Neeman, L., Finkler, A., Segev, Y., Myasoedov, Y., Rappaport, M. L., Huber, M. E. & Zeldov, E. A scanning superconducting quantum interference device with single electron spin sensitivity. *Nature Nanotech.* **8**, 639-644 (2013)

17. Huber, M., Neil, P., Benson, R., Burns, D., Corey, A., Flynn, C.; Kitaygorodskaya, Y., Massihzadeh, O., Martinis, J. & Hilton, G. DC SQUID series array amplifiers with 120 MHz bandwidth. *IEEE Trans. Appl. Supercond.* **11**, 4048 (2001).
18. Anahory, Y., Reiner, J., Embon, L., Halbertal, D., Yakovenko, A., Myasoedov, Y., Rappaport, M.L., Huber, M.E. and Zeldov, E., Three-junction SQUID-on-tip with tunable in-plane and out-of-plane magnetic field sensitivity. Nano. Lett. 14(11), 6481-6487 (2014)
19. Pearl, J., Current distribution in superconducting films carrying quantized fluxoids. *Appl. Phys. Lett.* **5**, 65 (1964)
20. Larbalestier, D., Gurevich, A., Feldmann, D. M. & Polyanskii, A. High-Tc superconducting materials for electric power applications. *Nature* **414**, 368-377 (2001)
21. Macmanus-Driscoll, J. L., Foltyn, S. R., Jia, Q. X., Wang, H., Serquis, A., Civale, L., Maiorov, B., Hawley, M. E., Maley, M. P. & Peterson, D. E. Strongly enhanced current densities in superconducting coated conductors of $YBa_2Cu_3O_{7-x}$ + $BaZrO_3$, *Nature Mater.* **3**, 439-443 (2004)
22. Fang L., Jia, Y., Mishra, V., Chaparro, C., Vlasko-Vlasov, V. K., Koshelev, A. E., Welp, U., Crabtree, G. W., Zhu, S., Zhigadlo, N. D., Katrych, S., Karpinski, J. & Kwok, W. K. Huge critical current density and tailored superconducting anisotropy in $SmFeAsO_{0.8}F_{0.15}$ by low-density columnar-defect incorporation. *Nat Commun.* **4**, 2655 (2013)
23. Haugan, T. J., Barnes, P. N., Wheeler, R., Meisenkothen, F. & Sumption, M. D. Addition of nanoparticle dispersions to enhance flux pinning in the $YBa_2Cu_3O_{7-x}$ superconductor. *Nature* **430**, 867-870 (2004)
24. Mele, P., Matsumoto, K., Horide, T., Miura, O., Ichnose, A., Mukaida, M., Yoshida, Y. & Horii, S. Tuning of the critical current in $YBa_2Cu_3O_{7-x}$ thin films by controlling the size and density of Y_2O_3 nanoislands on annealed $SrTiO_3$ substrates. *Supercond. Sci. Technol*. **19**, 44-50 (2006)
25. Kang, S., Goyal, A., Li, J., Gapud, A. A., Martin, P. M., Heatherly, L., Thompson, J. R., Christen, D. K., List, F. A., Paranthaman, M. & Lee, D. F. High-performance high-T_c superconducting wires. *Science* **311**, 1911-1914 (2006)
26. Gutierrez, J., Lloreds, A., Gazquez, J., Gibert, M., Roma, N., Ricart, S., Pomar, A., Sandiumenge, F., Mesters, N., Puig, T. & Obradors, X. Strong isotropic flux pinning in solution-derived $YBa_2Cu_3O_{7-x}$ nanocomposite superconducting films. *Nature Mater.* **6**, 367-373 (2007)
27. Maiorov, B., Baily, S. A., Zhou, H., Ugurlu, O., Kennison, J. A., Dowden, P. C., Holesinger, T. G., Foltyn, S. R. & Civale, L. Synergetic combination of different types of defects to optimize pinning landscape using $BaZrO_3$ - doped $YBa_2Cu_3O_{7-x}$. *Nature Mater.* **8**, 398-404 (2009)
28. Llordés, A., Palau, A., Gázquez, J., Coll, M., Vlad, R., Pomar, A., Arbiol, J., Guzmán, R., Ye, S., Rouco, V., Sandiumenge, F., Ricart, S., Puig, T., Varela, M., Chateigner, D., Vanacken, J., Gutiérrez, J., Moshchalkov, V., Deutscher, G., Magen, C. & Obradors X. Nanoscale strain-induced pair suppression as a vortex-pinning mechanism in high-temperature superconductors. *Nature Mater.* **11**, 329-36 (2012)
29. Lee, S., Tarantini, C., Gao, P., Jiang, J., Weiss, J. D., Kametani, F., Folkman, C. M., Zhang, Y., Pan,X. Q., Hellstrom, E. E., Larbalestier, D. C. & Eom C. B. Artificially engineered superlattices of pnictide superconductors. *Nature Mater.* **12**, 392-396 (2013)

30. Abrikosov, A. A. On the magnetic properties of superconductors of the second group. *Sov. Phys. JETP* **5**, 1174–1182 (1957).
31. Blatter, G., Feigel'man M. V., Geshkenbein V. B., Larkin A. I. & Vinokur V. M. Vortices in high-temperature superconductors. *Rev. Mod. Phys.* **66,** 1125 (1994)
32. Larkin, A. I. Effect of inhomogeneities on structure of mixed state of superconductors. *Soviet Physics JETP-USSR* **31**(4), 784–& (1970)
33. Giamarchi, T. and Le Doussal, P. Elastic theory of pinned flux lattices. Phys. Rev. Lett. **72**, 1530–1533 (1994)
34. Giamarchi, T. and Le Doussal, P. Elastic theory of flux lattices in the presence of weak disorder. *Phys. Rev. B* **52**, 1242–1270 (1995)
35. Giamarchi, T. and Le Doussal, P. Phase diagrams of flux lattices with disorder. *Phys.Rev. B* **55**, 6577–6583 (1997)
36. Klein, T., Joumard, I., Blanchard, S., Marcus, J., Cubitt, R., Giamarchi, T., and Le Doussal, P. A bragg glass phase in the vortex lattice of a type ii superconductor. *Nature* **413** (6854), 404–406, (2001)
37. Cubitt, R., Forgan, E. M., Yang, G., Lee, S. L., Paul, D. M., Mook, H. A., Yethiraj, M., Kes, P. H., Li, T. W., Menovsky, A. A., Tarnawski, Z., and Mortensen, K. Direct observation of magnetic flux lattice melting and decomposition in the High-T_c superconductor $Bi_{2.15}Sr_{1.95}CaCu_2O_{8+x}$. *Nature* **365**, 407–411 (1993)
38. Beidenkopf, H., Avraham, N., Myasoedov, Y., Shtrikman, H., Zeldov, E., Rosenstein, B., Brandt, E. H., and Tamegai, T. Equilibrium first-order melting and second-order glass transitions of the vortex matter in $Bi_2Sr_2CaCu_2O_8$. *Phys. Rev. Lett.* **95**, 257004–4 (2005)
39. Anderson, P. W., Theory of flux creep in hard superconductors. *Phys. Rev. Lett.* **9**, 309-311 (1962)
40. Anderson, P. W. and Kim, Y. B., Hard superconductivity: Theory of the motion of Abrikosov flux lines. *Rev. Mod. Phys.* **36**(1), 39-43 (1964)
41. Brandt, E. H. Computer simulation of flux pinning in type-II superconductors. *Phys. Rev. Lett.* **50**, 1599–1602 (1983)
42. Tonomura, A., Kasai, H., Kamimura, O., Matsuda, T., Harada, K., Shimoyama, J., Kishio, K., and Kitazawa, K. Motion of vortices in superconductors. *Nature* **397**, 308–309 (1999)
43. Moon, K., Scalettar, R. T., and Zim´anyi, G. T. Dynamical phases of driven vortex systems. *Phys. Rev. Lett.* **77**, 2778–2781 (1996)
44. Olson, C. J., Reichhardt, C., and Nori, F. Nonequilibrium dynamic phase diagram for vortex lattices. *Phys. Rev. Lett.* **81**, 3757– (1998)
45. Giamarchi, T. and Le Doussal, P. Moving glass phase of driven lattices. *Phys. Rev. Lett.* **76**, 3408–3411 (1996)
46. Giamarchi, T. and Bhattacharya, S. Vortex phases. *Lecture Notes in Physics* **595**, 314–360 (2002)
47. Le Doussal, P. and Giamarchi, T. Moving glass theory of driven lattices with disorder. *Phys. Rev. B* **57**, 11356–11403 (1998)
48. Villegas, J. E., Savel'ev, S., Nori, F., Gonzalez, E. M., Anguita, J. V., García, R. & Vicent J. L. Superconducting reversible rectifier that controls the motion of magnetic flux quanta. *Science* **302**, 1188-1191 (2003)

49. Zhu, B. Y., Marchesoni, F. & Nori, F. Controlling the Motion of Magnetic Flux Quanta. *Phys. Rev. Lett.* **92**, 180602 (2004)
50. Oral A., Barnard, J. C., Bending, S. J., Kaya, I. I., Ooi, S., Tamegai, T. & Henini, M. Direct observation of melting of the vortex solid in $Bi_2Sr_2CaCu_2O_{8+\delta}$ single crystals, *Phys. Rev. Lett.* **80**, 3610 (1998)
51. Troyanovski, A. M., Aarts, J. & Kes, P. H. Collective and plastic vortex motion in superconductors at high flux densities. *Nature* **399**, 665-668 (1999)
52. Bending, S. J. Local magnetic probes of superconductors, *Advances in Physics* **48**, 449-535 (1999)
53. Auslaender, O. M., Luan, L., Straver, E. W. J., Hoffman, J. E., Koshnick, N. C., Zeldov, E., Bonn, D. A., Liang, R., Hardy, W. N. & Moler, K. A. Mechanics of individual isolated vortices in a cuprate superconductor. *Nature Phys.* **5**, 35-39 (2009)
54. Kalisky, B., Kirtley, J. R., Nowadnick, E. A., Dinner, R. B., Zeldov, E., Ariando, Wenderich, S., Hilgenkamp, H., Feldmann, D. M. & Moler, K. A. Dynamics of single vortices in grain boundaries: I-V characteristics on the femtovolt scale. *Appl. Phys. Lett.* **94**, 202504 (2009)
55. Guillamon, I., Suderow, H., Fernandez-Pacheco, A., Sese, J., Cordoba, R., De Teresa, J. M., Ibarra, M. R. & Vieira, S. Direct observation of melting in a two-dimensional superconducting vortex lattice. *Nature Physics* **5**, 651 - 655 (2009)
56. Lee, J., Wang, H., Dreyer, M., Berger, H. & Barker, B. I. Nonuniform and coherent motion of superconducting vortices in the picometer-per-second regime. *Phys. Rev. B* **84**, 060515 (2011)
57. Kalisky, B., Kirtley, J. R., Analytis, J. G., Chu, J. H., Fisher, I. R. & Moler, K. A. Behavior of vortices near twin boundaries in underdoped $Ba(Fe_{1-x}Cox)_2As_2$. *Phys. Rev. B* **83**, 064511 (2011)
58. Raes, B., Van de Vondel, J., Silhanek, A. V., de Souza Silva, C. C., Gutierrez, J., Kramer, R. B. G. & Moshchalkov, V. V. Local mapping of dissipative vortex motion. *Phys. Rev. B* **86**, 064522 (2012)
59. Timmermans, M., Samuely, T., Raes, B., Van de Vondel, J. & Moshchalkov, V. V. Dynamic Visualization of Nanoscale Vortex Orbits. *ACS Nano **8***, 2782–2787 (2014)
60. Suderow, H., Guillamón, H., Rodrigo, J. G. & Vieira, S. Imaging superconducting vortex cores and lattices with a scanning tunneling microscope. *Supercond. Sci. Technol.* **27**, 063001 (2014)
61. Ganguli, S. G., Saraswat, G., Ganguly, R., Singh, H., Bagwe, V., Shirage, P., Thamizhavel, A. & Raychaudhuri, P. Direct evidence of two-step disordering of the vortex lattice in a 3 dimensional superconductor, $Co_{0.0075}NbSe_2$. arXiv:1406.7422
62. Raes, B., de Souza Silva, C. C., Silhanek, A. V., Cabral, L. R. E., Moshchalkov, V. V. & Van de Vondel, J. Closer look at the low-frequency dynamics of vortex matter using scanning susceptibility microscopy. *Phys. Rev. B* **90**, 134508 (2014)
63. Bespalov, A.A. & Mel'nikov, A.S. Abrikosov vortex pinning on a cylindrical cavity inside the vortex core: formation of a bound state and depinning. *Supercond. Sci. Technol.* **26,** 085014 (2013)
64. Gurevich, A. & Cooley, L.D. Anisotropic flux pinning in a network of planar defects. *Phys. Rev.* B **50**, 13563 (1994)

65. Thuneberg, E. V., Kurkijarvi, J. & Rainer, D. Elementary-flux-pinning potential in type-II superconductors. *Phys. Rev.* B **29**, 3913 (1984)
66. Zeldov, E., Clem, J. R., McElfresh, M. & Darwin, M. Magnetization and transport currents in thin superconducting films. *Phys. Rev. B* **49**, 9802-9822 (1994)
67. Blatter, G., Geshkenbein, V. B. & Koopmann, J. A. G. Weak to strong pinning crossover. *Phys. Rev. Lett.* **92**, 067009 (2004)
68. Koshelev, A. E. & Kolton, A. B. Theory and simulations on strong pinning of vortex lines by nanoparticles. *Phys. Rev.* B **84**, 104528 (2011)
69. Thomann, A. U., Geshkenbein, V. B., & Blatter, G. Dynamical aspects of strong pinning of magnetic vortices in type-II superconductors, *Phys. Rev. Lett.* **108**, 217001 (2012)
70. Campbell, A. M. & Evetts, J. E. Flux vortices and transport current in type-II superconductors. *Adv. Phys.* **21**, 194–428 (1972)
71. Priour, D. J. & Fertig, H. A. Deformation and depinning of superconducting vortices from artificial defects: A Ginzburg-Landau study. *Phys. Rev.* B **67**, 054504 (2003)
72. Yeshurun, Y., Malozemoff, A. P. & Shaulov, A. Magnetic relaxation in high-temperature superconductors. *Rev. Mod. Phys*. **68**, 911-949 (1996)
73. Weiss, U. ***Quantum Dissipative Systems***, *4-th Ed.* World Scientific Publishing Co., Singapore (2012)
74. Kopnin, N. B. & Vinokur, V. M. Dynamic vortex mass in clean superconductors and superfluids. *Phys. Rev. Lett.* **81**, 3952-3955 (1998)
75. Sonin, E. B., Geshkenbein, V. B., van Oterlo, A. & Blatter, G. Vortex motion in charged and neutral superfluids: A hydrodynamic approach. *Phys. Rev.* B **57**, 578-581 (1998)
76. Chudnovsky, E. M. & Kuklov, A. B. Inertial mass of Abrikosov vortex. *Phys. Rev. Lett.* **91**, 067004 (2003)
77. Suhl, H. Inertial mass of a moving fluxiod. *Phys. Rev. Lett.* **14**, 226-230 (1965)
78. Hoffman, J. E. A Search for Alternative Electronic Order in the High Temperature Superconductor $Bi_2Sr_2CaCu_2O_{8+\delta}$ by Scanning Tunneling Microscopy, Ph.D thesis, University of California, Berkley (2003)

Appendices

In the following appendices I provide a detailed report of the characterization of the sample which was used in part II, and a detailed and technical explanation of the design and construction of the microscope.

I'm also including three sections regarding some of the theoretical work which was a part of this study. These were carried out by others and are brought here for completion of the work.

Sample characterization

Scanning Electron Microscopy (SEM)

Figure 21a shows a SEM image of the sample with the six micro-bridges. A circular pattern of shaped holes was also patterned around the bridges to provide a map for SOT microscope navigation. The bridge which was used for measurements is shown in more detail in Figure 21b. The central straight part of the bridge is 8 µm wide and 12 µm long. Figure 21c shows a zoomed-in image of the film exhibiting a granular structure typical of metallic surfaces. This is the same area which was imaged by the SOT microscope. The grain diameter is on the order of a few tens of nm. No other distinct defects were observed.

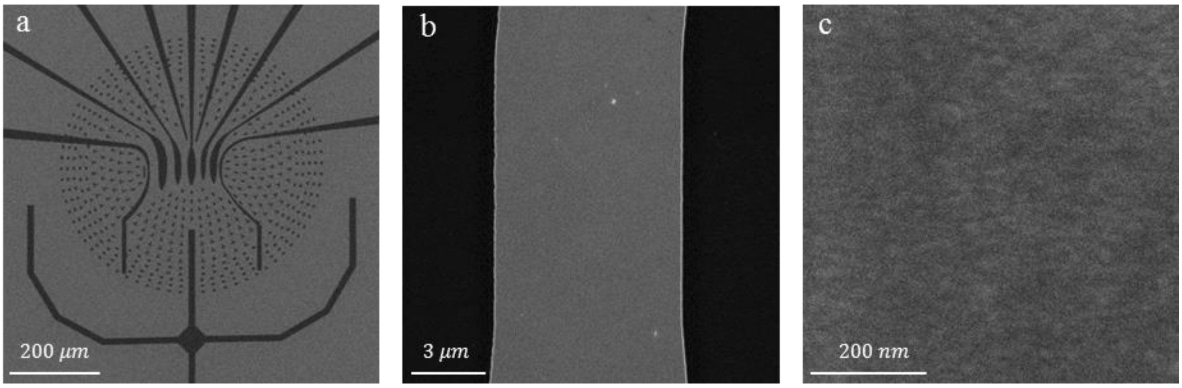

Figure 21. SEM images of the sample.

The Pb film is light gray and the substrate is dark. a, Six micro-bridges with different widths $(5 - 20\ \mu m)$ are patterned in the center. Currents can be applied through each of the bridges independently. A circular pattern of shaped holes provides a map for SOT microscope navigation. b, A zoomed-in image of the bridge on which the measurements were performed. The central straight section is 8 µm wide and 12 µm long. c, Surface of the Ge-capped Pb film showing grains with a typical diameter of a few tens of nm.

Atomic Force Microscopy (AFM)

Figure 22a shows a 3D representation of a 13x13 μm^2 scan of the 8 μm wide bridge using a commercial AFM. The overall thickness of the film was measured to be 82 nm which consists of a 75 nm thick Pb film and a 7 nm thick Ge capping layer. An averaged cross section of that scan is shown in Figure 22b.

Figure 22c is a high resolution 2x2 μm^2 scan of the surface showing a typical grain diameter on the order of a few tens of nm. Figure S3d displays a line cut through this scan showing a root mean square roughness of the surface of 1 nm.

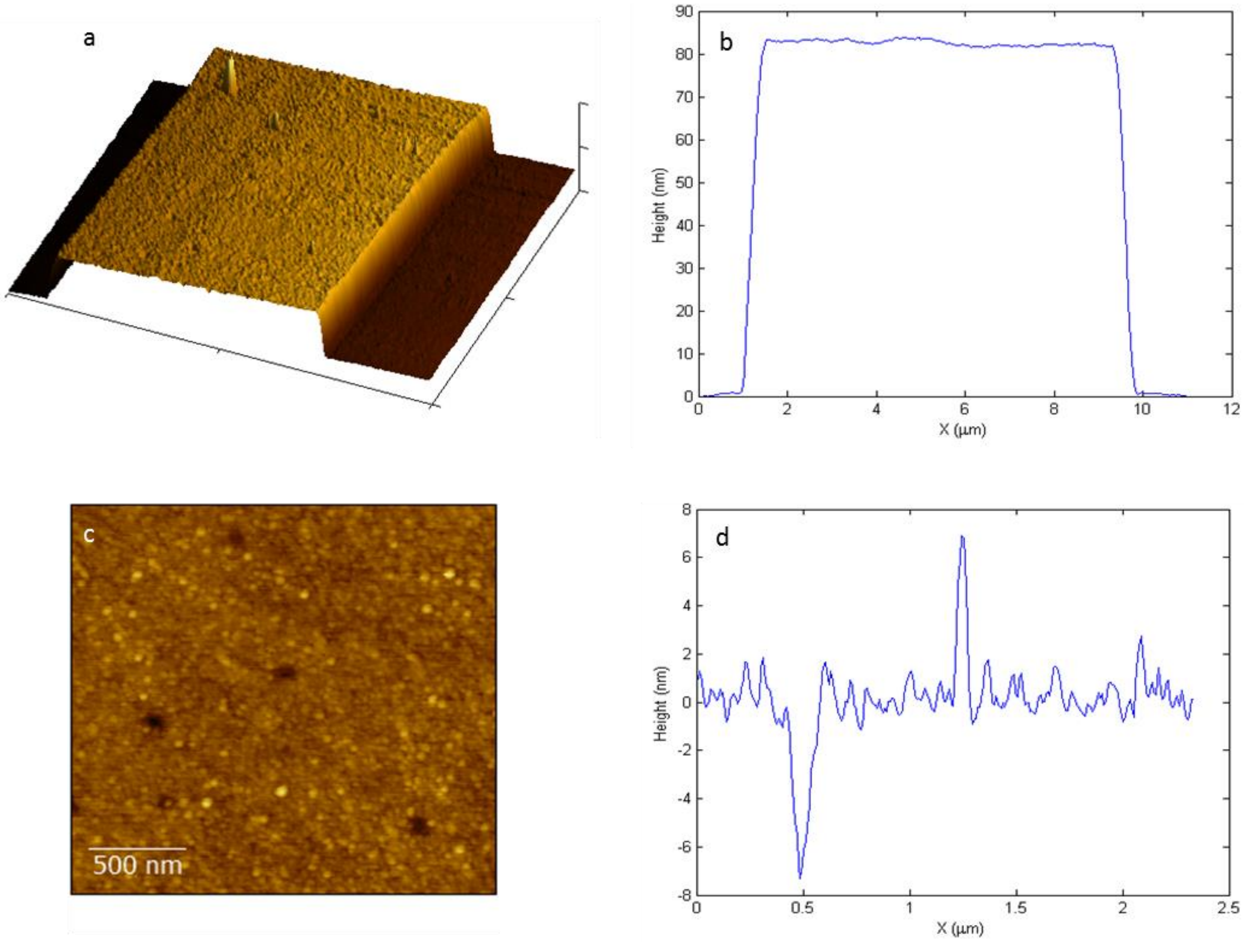

Figure 22. AFM scans of the 8 μm wide bridge.

a, A 3D representation of a 13x13 μm^2 scan. The surface of the film has granular features, as expected for a metallic surface. The patterned edges of the bridge are clear and sharp. b, An averaged cross section of the scan. The overall thickness of the film is 82 nm, which consists of 75 nm of Pb capped by 7 nm of Ge. c, A 2x2 μm^2 scan of the surface of the 8 um wide bridge. The false color scale spans 16 nm. The surface of the film is granular with a typical grain diameter on the order of a few tens of nm. d, An extracted line profile that was chosen to include both the highest and the lowest measured regions of (c). The calculated root mean square roughness is 1 nm.

X-ray Diffraction (XRD) measurements

The crystallographic phases of the Pb film were identified using XRD. An asymmetric 2θ scan with a fixed incident angle at 2 degrees was performed. The sample consists of a 70 nm thick unpatterned Pb film capped with 7 nm of Ge to prevent oxidation and was grown in similar conditions to the sample used in our experiment. Figure 23 shows ten Pb peaks associated with different (hkl) orientations of the crystallites. The unmarked peak corresponds to the Si substrate (asymmetrical (311)). The 7 nm Ge layer was not detected. It should be noted that the small incident angle results in a higher diffraction intensity from the thin film than from the substrate. Moreover, the direction of the observed lattice plain varies with the 2θ position, revealing the polycrystalline nature of the studied films, without any preferred orientation of crystallites. Using the Scherrer formula, the grain size was estimated to be 57 nm.

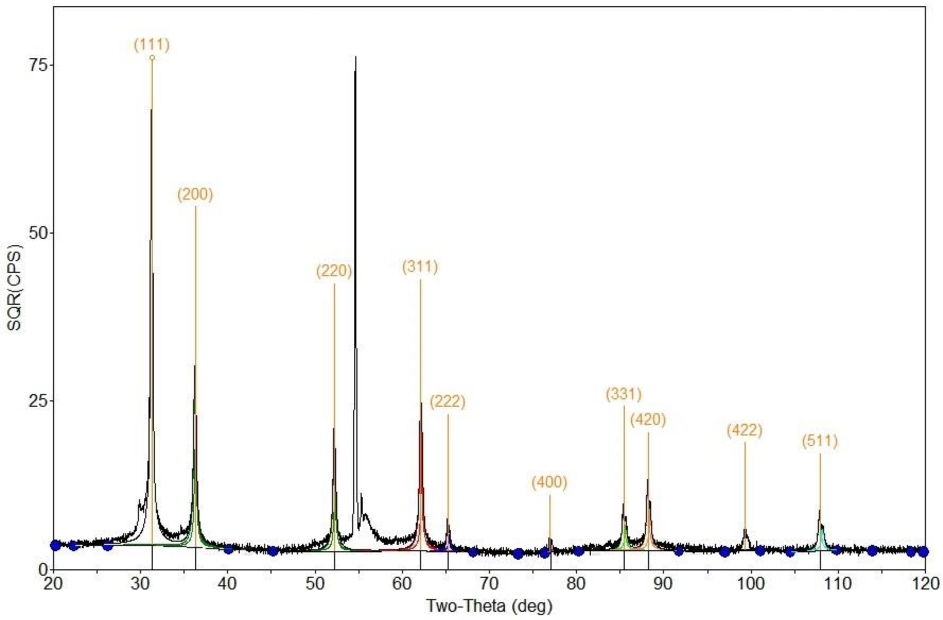

Figure 23. X-ray diffraction pattern of a Pb film.

The measurement was performed on a 70 nm thick Pb film grown under similar conditions as the sample. Ten different crystallite orientations were identified in addition to the signal from the Si substrate (unmarked peak).

Electrical transport measurement

Transport measurements exploring the upper critical field $H_{c2}(T)$ were conducted in order to determine the coherence length ξ and the penetration depth λ of the superconducting film. Figure 24a shows the resistance of the bridge as a function of the applied magnetic field for various temperatures.

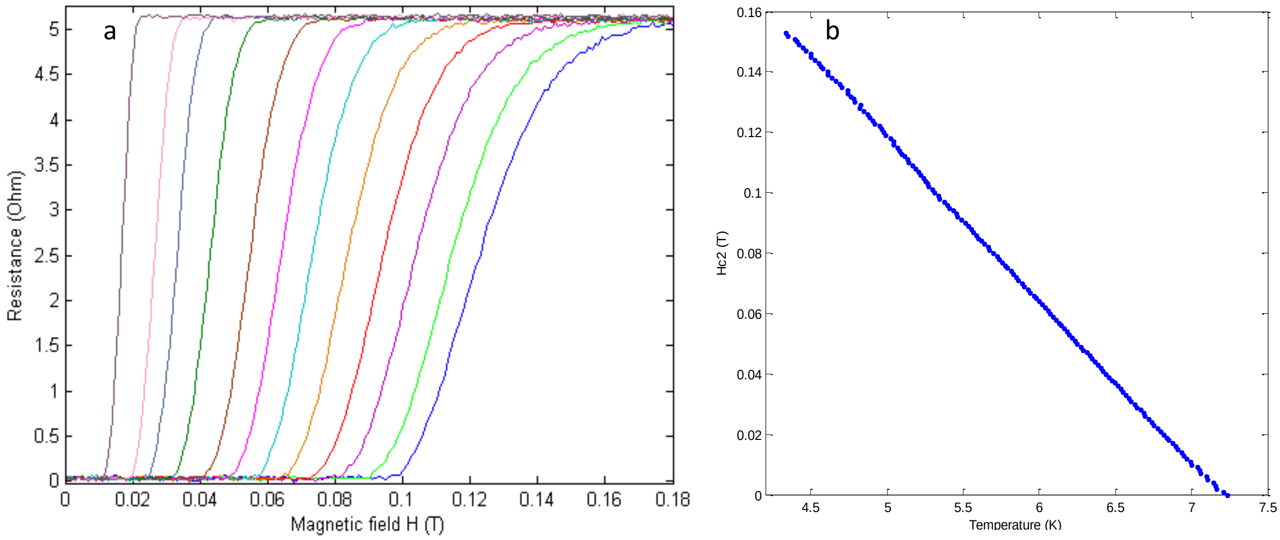

Figure 24. Transport measurement of the sample.

a, Resistance vs. applied magnetic field at different temperatures. The temperature values are equally spaced between 6.8 K (purple) and 4.44 K (blue). b, Superconducting upper critical field $H_{c2}(T)$. The line was determined using the $\frac{R}{R_N} = 0.9$ criterion, where R_N is the normal state resistance.

Figure 24b shows the extracted $H_{c2}(T)$ line, determined at 90% of the normal state resistance. From the measured $H_{c2}(4.2 \text{ K}) = 153\, mT$, and using the expression $H_{c2}(T) = \frac{\Phi_0}{2\pi\xi(T)^2}$ we find the coherence length $\xi(4.2 \text{ K}) = 46\, nm$. Assuming that the thermodynamic critical field H_c is unaffected by disorder, the magnetic penetration depth $\lambda(4.2K)$ can be calculated using the expression $H_c(T) = \frac{\Phi_0}{2\sqrt{2}\,\pi\,\lambda(T)\xi(T)}$. With $H_c(4.2K) = 53\, mT$ for Pb we find $\lambda(4.2K) = 96\, nm$.

Rate of thermally-activated vortex jumps

Vortices in a thin film of thickness d ~ ξ can be modeled as over-damped particles, so we evaluate the rate Γ of spontaneous hopping of vortices over the energy barrier ΔU between neighboring pins, using the standard theory of thermally-activated escape [73]:

$$\Gamma = \omega_0 e^{-\Delta U/kT}, \qquad \omega_0 = \frac{\omega_a \omega_b}{2\pi\gamma} \qquad (1)$$

where ω_a and ω_b are the frequencies of small oscillations at the bottom of the potential well and at the top of the inverted barrier, $\gamma = \eta/M$, M is the vortex mass per unit length, $\eta = \phi_0 B_{c2}/\rho_n$ is the Bardeen-Stephen vortex viscosity, $B_{c2} = \phi_0/2\pi\xi^2$ is the upper critical field, ϕ_0 is the flux quantum, and ρ_n is the normal state resistivity. We first estimate ω_a and ω_b for a vortex in a 1D tilted washboard potential $U(x) = [1 - \cos(2\pi x/s)]U_0 - J\phi_0 x$ where J is the sheet current density. The vortex position x(t) is described by the sine-Gordon equation

$$dM\ddot{x} + d\eta\dot{x} + \frac{2\pi U_0}{s}\sin\frac{2\pi x}{s} = J\phi_0 \qquad (2)$$

where U_0 is the maximum pinning energy, $s = C\xi$ is the characteristic spatial scale of the pinning site, and $C \sim 1$. Hence,

$$\omega_a^2 = \omega_b^2 = \frac{4\pi^2 U_0}{dM\xi^2 C^2}\sqrt{1-\beta^2} \qquad (3)$$

Here $\beta = J/J_c$, and $J_c = 2\pi U_0/s\phi_0$ is the sheet critical current density. Near the depinning transition, $J \approx J_c$ and the expansions of the activation barrier $\Delta U(\beta)$ and the effective attempt frequency ω_0 in the small parameter $1 - \beta << 1$ yield

$$\Delta U = \frac{4\sqrt{2}}{3} U_0 (1-\beta)^{3/2} \qquad (4)$$

$$\omega_0 = \frac{4\pi^2 U_0 R_s \sqrt{2(1-\beta)}}{\phi_0^2 C^2} \qquad (5)$$

where $R_s = \rho_n/d$ is the film sheet resistance in the normal state. For the parameters of our Pb film, U_0 = 2 eV, and R_s = 0.21 Ω, we obtain $\Delta U/ k_B T = 1.042\times10^4(1-\beta)^{3/2}$ at T = 4.2K, and $\omega_0 = 8.1\times10^{11}(1-\beta)^{1/2}/C^2$ Hz. We now estimate the critical value of β_c at which thermal fluctuations cause spontaneous hopping of vortices between pinning sites within the time window $t_0 \cong 300$ s of our measurements. Defining β_c by the condition $\Gamma t_0 \approx 1$, we have the following relationship

$$\frac{4\pi^2 U_0 t_0 R_s \sqrt{2(1-\beta_c)}}{\phi_0^2 C^2} exp\left[-\frac{4\sqrt{2}U_0}{3kT}(1-\beta_c)^{3/2}\right] = 1 \qquad (6)$$

For the materials parameters given above, and with C = 1, Eq. (6) yields $1 - \beta_c \cong 0.022$, $\omega_0 \cong 1.2\times10^{11}$ Hz, and $\Delta U(\beta_c) \cong 34\ k_BT = 12$ meV. As a result, the pinning spring constant $\alpha(\beta) = \alpha_0(1 - \beta_c^2)^{1/2} \approx \alpha_0/5$ softens at the transition point $\beta = \beta_c$ by a factor of ~5 relative to the spring constant α_0 at zero current.

The thermally-activated hopping rate can be enhanced by quantum effects even well above the crossover temperature $T_0 = \hbar\omega_0/k$ at which Γ becomes limited by the quantum tunneling of vortices. For the above values, the quantum crossover temperature $T_0 = 0.9$ K at C = 1, well below T = 4.2 K. In this case Γ in Eq. (1) is increased by the factor q given by [73]

$$q = (\gamma^2 T_0/\omega_b^2 T)^{2T_0/T} \qquad (7)$$

For $T = 4T_0$, the factor $q = \gamma/2\omega_b = 0.5(\hbar\eta/2\pi k_B T_0 M)^{1/2}$ can be large, but it depends on uncertain parameters such as the vortex mass which is determined by multiple mechanisms [74-76]. As an illustration, we evaluate an upper limit of q taking into account only the contribution of localized quasiparticles in the vortex core to the mass, $M = 2mk_F/\pi^3$ where m is the effective electron mass and k_F is the Fermi wave number [77]. Hence, $q = (\pi/4)[\hbar\phi_0 B_{c2}/R_n d m k_F k_B T_0]^{1/2}$. For $k_F = 10^{10}$ m^{-1}, $B_{c2} = 153$ mT and the parameters used above, we get $q \approx 3$, which would give a negligible contribution to $1 - \beta_c$ for the huge values of $t_0\Gamma_0$ and U_0/k_BT evaluated above. Even the much larger quantum factor $q \sim 10^3$ would increase the critical value of $1 - \beta_c = 0.022$ by only 17%.

Numerical simulations

We generated various sets of randomly distributed defects in an area of 1.2×1.2 μm^2 to simulate the vortex dynamics. Each defect contributes a potential of the form $U_n(x,y) = \frac{-U_0}{1+\left(\frac{x-x_n}{\xi}\right)^2+\left(\frac{y-y_n}{\xi}\right)^2}$, with the total potential given by a linear superposition from all the n defects. The simulations in Figure 4 were performed using $U_0 = 0.66$ eV, a defect density of 200 μm^{-2}, and $\xi = 46.4$ nm. For each increment of F_{dc} we trace the vortex flow by solving the massless dynamic equation of vortex velocity vector $\boldsymbol{v}$ given by $\boldsymbol{v} = -\nabla U$, where U is the tilted potential. The viscous vortex drag is not taken into account since, even though the velocity is inversely proportional to the vortex viscosity, the resulting vortex trajectory is independent of the viscosity. As long as the vortex resides inside the well, the trajectory follows the minimum of the titled potential at each F_{dc}. When F_{dc} exceeds the maximum restoring force of a well, the vortex flows along an intricate dynamic trajectory defined by the gradient of the tilted potential until it reaches the next minimum point (dashed lines in Figure 4c). Note that the color scale in Figure 4c represents the un-tilted potential. Similar to the experimental case, we perform subloops of the driving force in order to explore the full set of trajectories.

We have also explored additional functional forms of $U(x,y)$ of a defect, including a potential similar to that derived using Ginzburg-Landau calculations in [63]. The qualitative features described in the paper could be reproduced with the different defect potentials for comparable values of U_0 and ξ.

Ginzburg-Landau simulations of strong pinning

We solve the problem of depinning of a single vortex in a film using the static GL equation

$$\Delta\psi + (1 - p(x,y) - |\psi|^2)\psi = 0. \qquad (1)$$

Equation (1) is written in a dimensionless form, where all distances are measured in $\xi(T)$ and the order parameter $\psi(x,y)$ is in units of the equilibrium order parameter ψ_0. The magnetic vector potential responsible for the London screening near the vortex core is neglected. The function $p(x,y)$ quantifies the local depression of $T_c(x,y)$ that produces the pinning potential well. We used the following model form of $p(x,y)$:

$$p(x,y) = p_0(\tanh(a-r) + \tanh(a+r)), \qquad (2)$$

where p_0 and a define the magnitude and the width of the well, respectively, $\mathrm{r} = \sqrt{\mathrm{x}^2 + \mathrm{y}^2}$, and the center of the pin is placed at the origin. Unlike the sharp rectangular well for a dielectric precipitate or a pinhole, $p(r)$ in Equation (2) has smooth tails that decay over the coherence length ξ, consistent with the static GL solution for the superconducting-normal domain well. This form of $p(r)$ models a proximity-coupled normal region, for example a circular normal island on the film surface, which suppresses superconductivity all the way across the film thickness $d \cong \xi$.

We solve Equations (1) and (2) on a $20 \times 20\, \xi^2$ area, which is large enough to prevent the boundaries from influencing the depinning critical current. An external dc current is imposed in the y direction and a zero perpendicular current condition is imposed across the side boundaries. The solution of this problem gives the dependence of the vortex displacement $u(J)$ as a function of the dc current density J normalized to the critical current density J_c (Figure 25). Here, the vortex core coordinate $u(J)$ is defined as the position of the topological singularity in the phase of the order parameter. The dependence $u(J)$ terminates at $J = J_c$ so that the GL equations do not have static vortex solutions at $J > J_c$. The results of this simulation for different values of the potential depth p_0 and $a = 1.5$ are shown in Figure 25. The displacement $u(J)$ monotonically increases with J and the pinning spring constant softens noticeably as J approaches J_c. The overall behaviors of the restoring force and the potential are similar to that of the model Lorentzian $U(r)$ considered in the main text. The full GL calculation thus does not produce the broken-spring behavior for a single defect even in the case of strong pinning, so the concept of rigid pinning wells can be used, at least qualitatively, for both weak and strong pinning. The latter is important because pinning energies in Pb films suggest strong pinning with $p_0 > 1$.

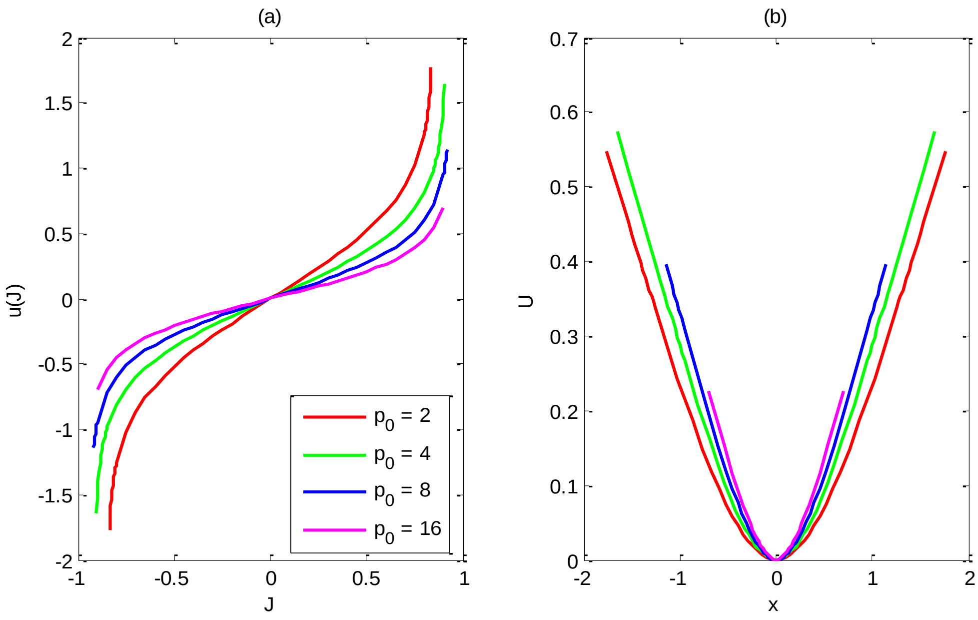

Figure 25. GL calculation of a strong pinning potential.

a, The vortex displacement $u(J)$ as a function of the dc current density J for different values of p_0 and $a = 1.5$. b, Reconstruction of potential wells for different values of p_0 from the displacement plot (a).

Microscope design

In this appendix I describe in technical detail the design of the main parts of the microscope. It is intended for an advanced user who is examining the parts of the system and is interested in understanding their design considerations. The schematics for the parts are provided in "Microscope schematics" starting on page 82.

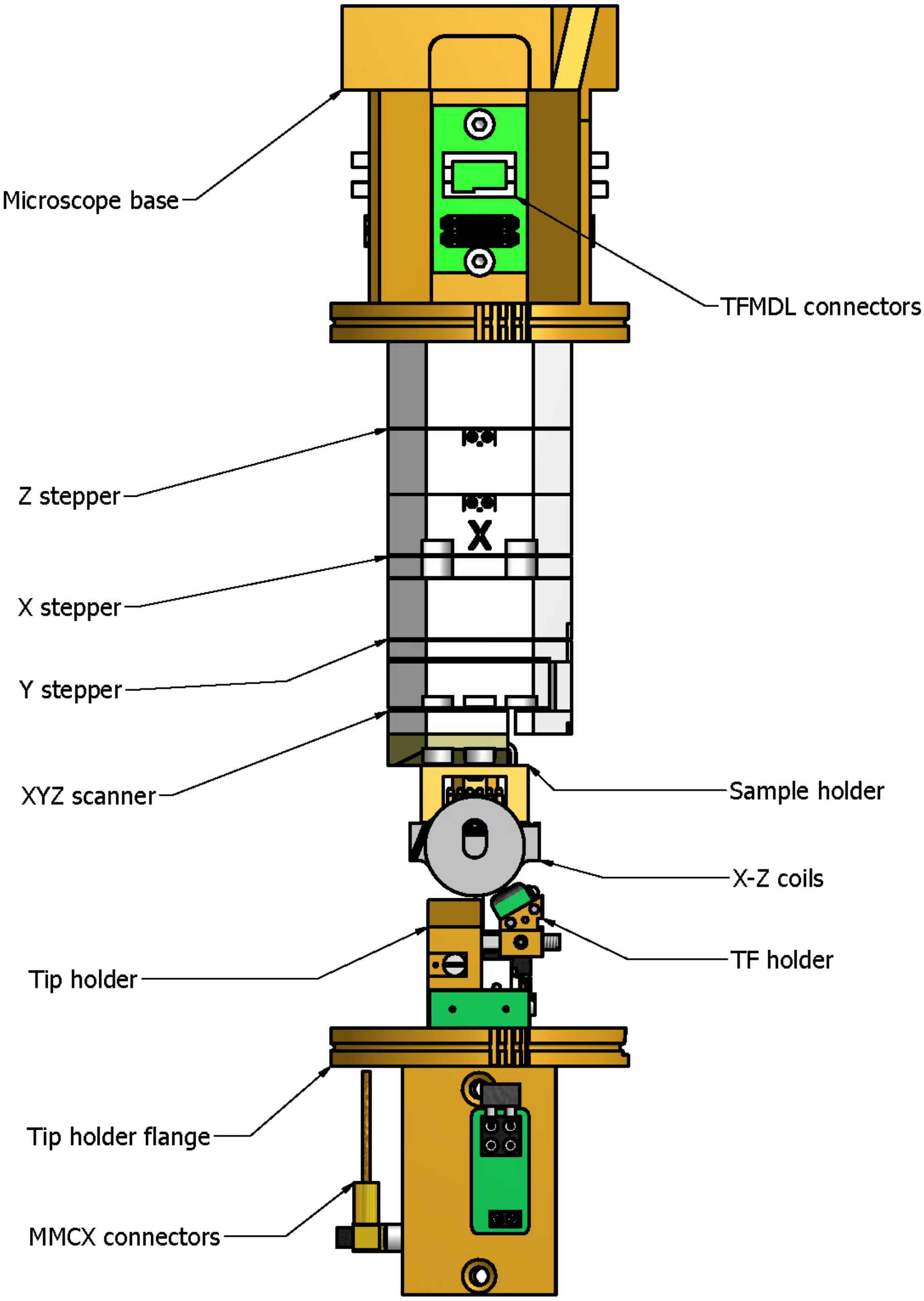

Figure 26. Model of the microscope with the protective sleeve removed.

Tip holder flange

This bottommost part holds the tip holder in place and carries signals from incoming cables via PCB's to the tip and tuning fork. It is fastened to the protective sleeve. Its main part is a disc with a dove tail shaped groove into which the tip holder slides. The tip holder position is determined by a fixed stopper. It is kept in the groove by a dove tail stub, and fixed in place from below by a plastic screw. A non-conducting screw is essential for maintaining the differential connection to the tip.

Below the disc is a hollow box looking element. This was built to accommodate PCB's for the tip, optical relay and tuning fork. In the current design, the following wires may be connected: a twisted pair 2.54mm SIP connector to the SOT, a twisted pair 2mm SIP connector to power the optical short, a twisted pair 2mm SIP connector for the Attocube trans-impedance converter Vdd, two single ended coax MMCX for the dither and two single ended coax MMCX for the TF out. The part was designed to be modular with interchangeable PCB's. In fact, as long as the disc part and the SOT connections are preserved, one may design an alternative bottom flange which will suit future needs (for example, a design for the optical tip vibration readout scheme is already being made).

Tip holder

The most advanced version of the tip holder, which has now become a standard in the lab was designed to enable differential operation. It has a double dovetail design and has three electrically isolated parts:

The bottom dovetail is fixed to the microscope's bottom flange and therefore shares the chassis ground. It is isolated from the SOT by two PEEK pieces, a flat one which separates it from the tip holder body and a "cup" which isolates it from the long m2 screw that holds the entire construction together.

The body of the tip holder has a round groove in which the tip fits. It constitutes the "back electrode". To ensure the contact to the tip, a Beryllium-Copper spring is screwed to the back of the holder and is pressed against the tip. On its side there is a tapered m1.6 hole and a small notch to which the microscope connects. The top dovetail mates with the cooling cube of the thermal evaporator for deposition of the Pb layers which form the SOT. The slanted notch prevents the body from shadowing the tip. The body also has two stainless steel rails which were used to mount the tuning fork (TF) holder. Between the rails there are two m1 screw holes for mounting a "bridge" to which the tuning fork holder connected (in a more recent version the bridge is an integral part of the holder body). Future techniques should preferably fit this construction. Alternatively, the tuning fork related part may be altered or abandoned completely.

The PEEK front electrode (sometimes referred to by tip makers as “top” electrode) is screwed to the body and makes contact to the second lead of the SOT. Inside the insulating PEEK frame is a stainless steel (or brass) rectangular part. To its inner side a Beryllium-Copper spring is spot-welded which touches the tip. The spring can also be mechanically reinforced by two m1 screws and nuts. On the other side there is a threaded hole with a notch to which the microscope connects. A sharpened m1 screw also threads through this piece. When tightened it makes contact to the body, shorting the two parts and hence the SOT.

Tuning fork holder

The holder allows two degrees of freedom in bringing the TF to contact with the tip. It is mounted on the tip holder rails with two holes. Moving it closer or further is done using a double threaded (right and left handed) rod which runs through its center and connects to the bridge on the tip holder. The bridge has a normal right handed thread and the TF holder a left handed thread. The double threaded rod design was chosen for stability (over the screw and spring design) and also gives twice the travel per turn in comparison to a normal screw.

The holder itself is split in two. The dither is glued to the main part which is mounted on the tip holder. A sliding stage holds the Attocube trans-impedance converter and the TF. This stage can be moved laterally on two rails and adjusted by an m1 screw countered by a spring.

The height alignment of the tip and TF was done prior to the deposition either manually or using a specially made tool which uses a fine threaded screw to push the tip up.

Protective sleeve

The sleeve is fastened to the microscope base and holds the bottom flange in place. It also protects the Attocube positioner stack from mechanical damage. It has wire notches along its length and circumferential notches to tie them in place. To heighten its resonance frequencies, the sleeve’s wall thickness was made as thick as the moving parts would allow. Therefore, it has three different internal diameters. On its bottom edge there are three big windows for pre-alignment of the tip and sample. The rounded square hole was used to un-short the tip in an earlier version of the tip holder and is now not in use. A small round hole was added for un-shorting the tip with the current holder design.

Microscope base and positioner stack

This part is screwed to the microscope body and holds the positioner stack and the protective sleeve in place. It has four small PCB's which connect to flexible TFMDL Samtec cables (carrying 10 single wires each) that come from the body, and distribute the wires. Most of the wires (sample contacts, positioner stack, heater and thermometry) go into the protective sleeve and some (Vdd and optical relay) go outside the sleeve. The four "ribs" are there to strengthen the construction for vibration considerations.

The microscope uses Attocube piezo-positioners for the coarse motion and fine scanning. The stack consists of an ANPz101/RES (5 wires), two ANPx-101 (2 wires each) and an ANSxyz100 scanner (6 wires).

Sample holder

The sample holder is connected at the bottom of the Attocube stack. Its base is made of GE10 which is held by screws to the scanner. The main part is made of brass. A Lakeshore TG-120P GaAlAs calibrated diode was placed inside its core and a ~35 Ω heating wire is wound around its base. The sample 24 pin chip socket is screwed into the base using a custom made m2 screw which has a particularly large head to also act as a flat leveled stopper once a sample carrying chip is pushed in. The socket is kept from rotating by four arms which fit to notches in its corners. These arms also have threaded m1 holes with which the chip carrier can be fastened to the sample holder.

20 wires arrive to the sample holder. 4 of them are used for the thermometry, 2 for the heater and 14 are designated for the sample (out of 24 pins). All of the wires are soldered to the pins of the socket (making one row of 6 pins unusable for the sample).

In case the sample is especially sensitive to electrostatic discharge and shorting is required. One may short the wires to the sample by connecting shorted TFMDL cables to the A and C PCB's on the microscope base.

X-Z coils

A new addition is the X and Z coil chip carrier. These coils were built to enable the application of small ac fields to the sample. They are built as one piece with the chip carrier so they are not a permanent part of the microscope. The coils use 4 of the sample pins as current leads (leaving only 10 available).

A 24 pin chip carrier was inserted and glued to the Z coil after winding it. The coil uses a 0.127 mm outer diameter Supercon Inc. NB-Ti wire and has 105 windings. These are then inserted and glued to the X coil construction which has a coil on each side for uniformity and strength of the field. Each coil has 160 windings and together they produce ~100 G/A (by calculation) in the plane of the sample. Figure 27 shows the results from COMSOL simulations for the field to current ratio on the plane of the field. Using the SOT, the ratio of the Z coil at the center of the sample was measured to be 80 G/A, slightly higher than predicted by the simulation.

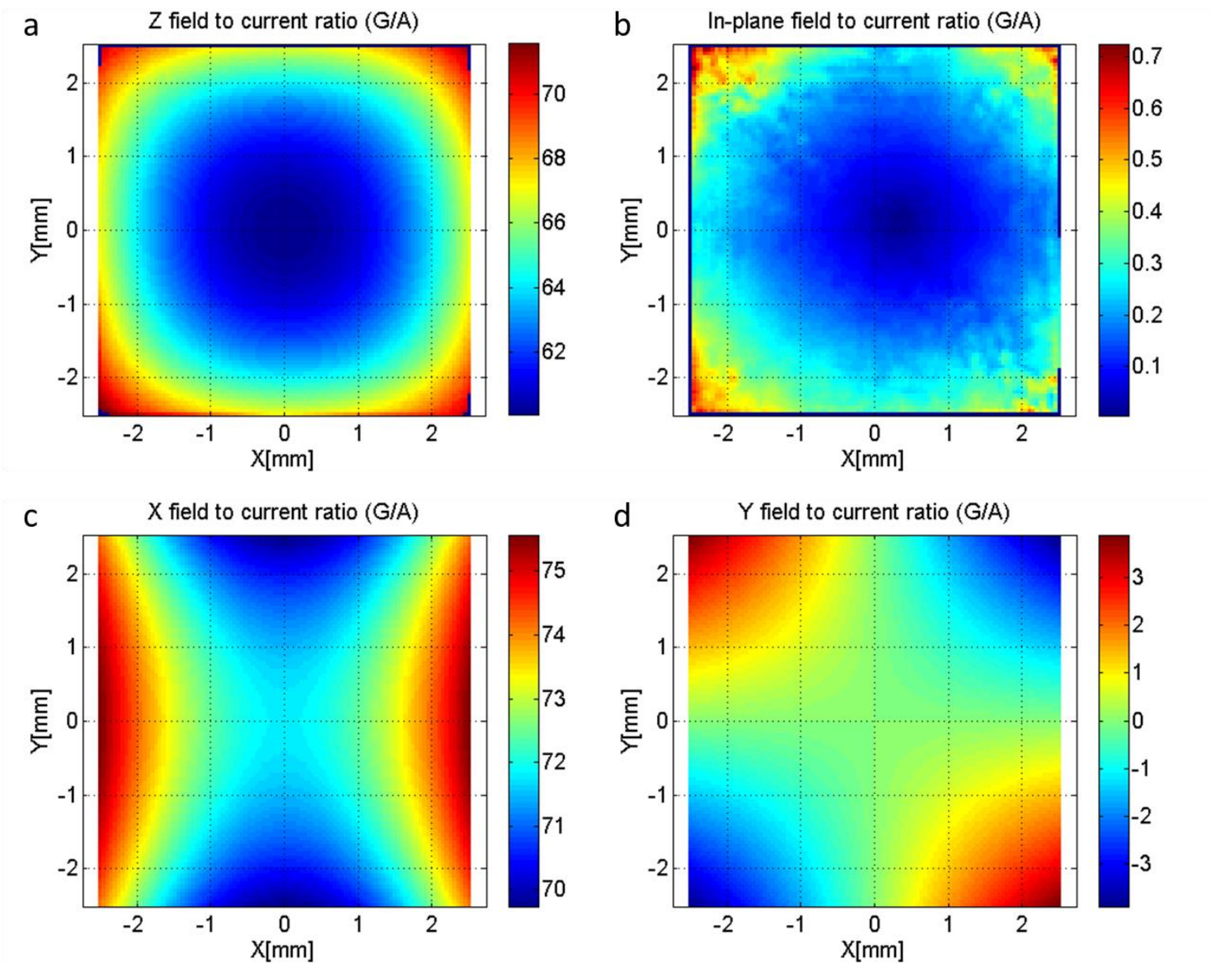

Figure 27. Simulations of the magnetic field generated by the on-sample coils.

COMSOL simulation results of the field which is created on the plane of the sample by the Z and X on-sample coils. a, Z field to current ratio for 105 turns (linearly dependent). b, The in-plane component assuming a plane 50 μm away from the center of the coil. c, X field to current ratio for 2x160 turn coils (linearly dependent). d, The in-plane perpendicular component.

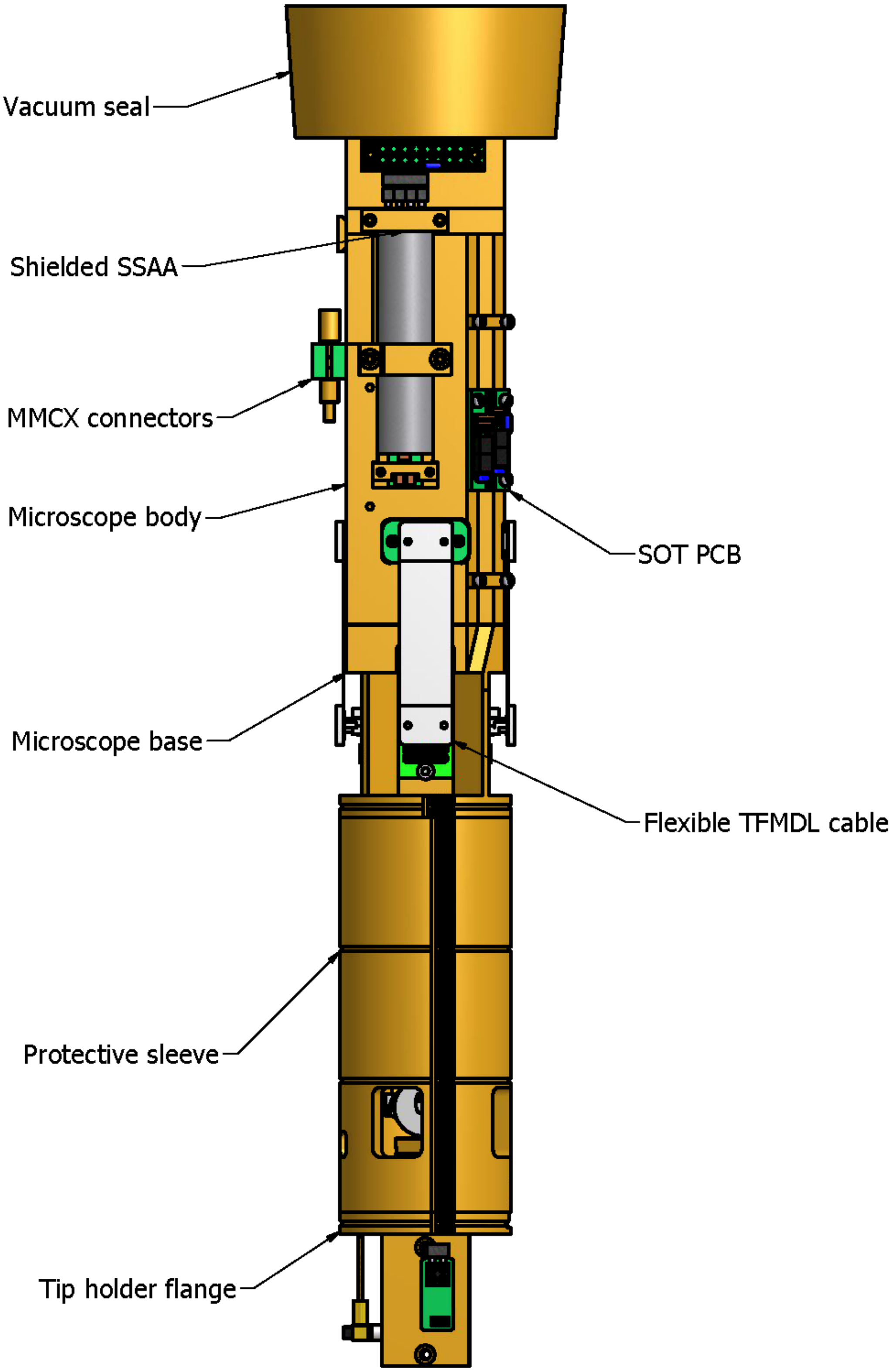

Figure 28. Model of the microscope

The shown parts are 31cm tall.

Body

The body is fastened to the sealing cone. It has four facets holding the SSAA inside its magnetic shield (3 layers of μ metal – Nb - μ metal, made of four concentric cylinders), a PCB for the SOT electronic circuit (bias and shunt resistors) which is shielded by a brass cover and 4 fixed MMCX connectors for coaxial wires coming from the top (TF out and dither).

Six single ended coax lines for the SOT emerge at its base from the rod. Four (SSAAbias and FBcoil) are connected via a small auxiliary breadboard to the SSAA and two (SOTbias) are soldered to the SOT PCB. A twisted pair connects the SOT PCB to the SSAA input coil and a shielded twisted pair goes out of the SOT PCB through a designated notch in the body to connect to the SOT contacts at the bottom flange.

The rest of the wires arrive through the rod bunched into three 12 twisted pair “copper looms”. The wires go through a ¾ inch bore in the body and clamped at its bottom. The wires are split into four groups and are pulled out through four windows in the body to be soldered to PCB’s with TFMDL connectors.

Vacuum can

The sealing cone is silver soldered to a stainless steel tube. It is made of brass with a conical angle of 4 degrees. Its counterpart is the vacuum can which has two diameters, determined by the diameters of the superconducting magnet GE10 supporting sleeve and its bore. Notice that the precise length of the can is what sets the position of the tip and sample in the center of the magnet.

Close to the can’s rim there are two holes. These are used for inserting a plain metal wire to prevent the can from falling into the dewar in case of a loss of vacuum. At the bottom side there are three threaded holes on the base and three along the circumference. These were never used and were put there for the option of strengthening the contact between the microscope and the magnet.

The tube and the top part

The microscope is held by a ¾ inch thin walled stainless steel tube. The wires run down the tube wound around two rods with baffle plates.

Note that when the microscope is fully inserted into the dewar, it still sticks out about 30cm above the flange. This was left to enable the future addition of some sort of a gimbal between the microscope and the neck of the dewar for vibration isolation.

The tube is connected at its top to a manifold cube. This is connected on its top to a six-way kf25 cross creating together 9 usable faces:

- A flange with 6 SMA PE9184 vacuum feed-through connectors for the coaxial wires of the SOT and SSAA operation (marked by I-VI)
- A ball valve with a quick connect socket for exchange gas introduction
- Three 15 pin sub-D vacuum feed-through connectors on a kf50 flange for all of the single wires (marked by A, B and C). These have a Spectrum control K-type pi filter on the inner side of the microscope.
- A KF25 valve for pumping
- A flange with 7 (only 6 are in use) SMA PE9184 vacuum feed-through connectors for TF operation and for the Z-scanner (marked by A-F).
- A Kurt J. Lesker convectron pressure gauge
- A 1 psi pressure release valve and a hanger

A plastic arm is connected to the manifold. It holds a laser which points downwards. In combination with a goniometer connected to the dewar, this is used to the determine the rotation of the probe in respect to the magnet (when using in-plane field).

Wiring

Conceptually, the wires were divided into two groups. The most sensitive signals (SOT, TF and Z-scanner) which are all carried by single ended Lakeshore CC-SC-250 coaxial wires terminated by SMA connectors, and the less sensitive signals (sample wires, coarse positioners, heater and thermometer, Vdd and the optical short) which are all carried by a Copper loom terminated by a sub-D 15 pin filtered connector. These groups were also wound separately on the rods leading down the tube.

The coaxial signals are conneted directly to their respective instruments. The shields are connected to the chassis only at the top and are left floating inside the microscope. The single wire signals are carried by a Samtec EQCD cable and connect to three distribution boxes (Marked by A, B and C) which split them up into BNC connectors (boxes A and B) or single end “banana” connectors (box C – sample wires).

The following table details the path and connector number of every signal:

Dist. Box A

Inst.	**Dist. box**	**Blue Samtec**	**Sub-d pin**	**Samtec**	**Sample holder**
Heater +	BNC1+	35	7	A6	5
Heater -	BNC1-	39	8	A5	6
Relay +	BNC2+	23	5	D2	-
Relay -	BNC2-	31	6	D1	-
Spare	BNC3+	27	13	-	-
Spare	BNC3-	30	14	-	-
Thermo. I-	BNC5+	3	1	A3	2-ו 1 Blue
Thermo. V-	BNC4+	11	3	A4	
Thermo. I+	BNC5-	7	2	A1	4-ו 3 Red
Thermo. V+	BNC4-	15	4	A2	
Spare	BNC6+	38	15	-	-
Spare	BNC6-	GND	-	-	-
Spare	BNC7+	22	11	-	-
Spare	BNC7-	19	12	-	-
Spare	BNC8+	4	9	-	-
Spare	BNC8-	14	10	-	-

Dist. Box B

Inst.	Dist. box	Blue Samtec	Sub-d pin	Samtec	Wire color
Xstep+	BNC9+	3	1	B1	Red
A <-> C	BNC9-	Floating	-	-	-
Xstep-	BNC7+	7	2	B2	Blue
Green	BNC7-	Floating	-	-	-
Ystep+	BNC8+	11	3	D3	Red
B <-> D	BNC8-	Floating	-	-	-
Ystep-	BNC6+	15	4	D4	Blue
Blue	BNC6-	Floating	-	-	-
Zstep+	BNC4+	23	5	D5	Red
	BNC4-	Floating	-	-	-
Zstep-	BNC3+	31	6	D6	Blue
	BNC3-	Floating	-	-	-
Zencoder S+	BNC2+	35	7	D7	Red
	BNC2-	Floating	-	-	-
Zencoder U0	BNC1+	39	8	D8	Green
	BNC1-	Floating	-	-	-
Zencoder GND	BNC12+	4	9	D9	Blue
	BNC12-	Floating	-	-	-
Xscan	BNC11+	14	10	B3	Blue
Xscan	BNC11-	22	11	B4	Blue
Yscan	BNC5+	19	12	B5	Green
Yscan	BNC5-	27	13	B6	Green
Vdd+ / heating resistor	BNC10+	30	14	B7	
Vdd- / heating resistor	BNC10-	38	15	B8	

Dist. Box C

Inst.	C sample	Blue Samtec	Sub-d pin	Samtec	Sample holder
	16	35	7	C4	16
	15	39	8	C3	15
pair	18	23	5	C6	18
	17	31	6	C5	17
	7	27	13	A7	7
	10	30	14	A10	10
pair	20	11	3	C8	20
	19	15	4	C7	19
	22	3	1	C10	22
	21	7	2	C9	21
pair	9	22	11	A9	9
	8	19	12	A8	8
pair	14	4	9	C2	14
	13	14	10	C1	13

Coax. Lines

A	Z scan+	Samtec B9
B	Z scan-	Samtec B10
C	Dither-	
D	Dither+	
E	TF Vout-	
F	TF Vout+	
G	-	
I	SOT Bias	Resistor
II	SOT Bias	
III	FB coil	Resistor
IV	FB coil	
V,VI	SA bias	

Vibration isolation

Much effort was invested in isolating the microscope from vibrations. The most troublesome frequency range is the 100's Hz which is where the resonant frequency of the Attocube positioner stack is located.

As mentioned above, the different parts comprising the microscope were designed to be as massive as possible and shaped with the aid of computerized modal analysis to avoid having resonances in this range.

Furthermore, an entire vibration isolation construction was built in the lab:

A roughly 2 metric Ton reinforced concrete block was cast, into which the system's dewar is inserted and clamped. The dewar was wrapped in a rubber-foam-lead acoustic mat. The block can be suspended in the air by a set of four Newport S-2000A-423.5 isolators which operate using compressed air (pressure should be set to ~50 psi) and attenuate the mechanical vibrations.

Around the concrete construction we have built a concrete filled block wall for acoustic isolation. On the inside of the wall are sheets of mineral wool for acoustic damping. The wall has four hatches to allow access to the pneumatic isolators. The hatches are sealed by concrete filled steel frame plugs. Through the wall we have passed four tubes to carry the needed wires and tubes from the lab inside. The tubes were then filled with sand.

The rim of the wall has a flat marble like material finish. Several threaded rods were embedded in the concrete. These allow the fastening of a specially built steel acoustic roof. In order to access the system, the roof was fitted with a lid that may be opened with the aid of a pneumatic double piston. When the lid is fully opened, the dewar maybe lifted out through the hatch.

The following graph sums the contribution of the isolation system. Our numbers match compare well to vibration measurements of leading SPM laboratories [78].

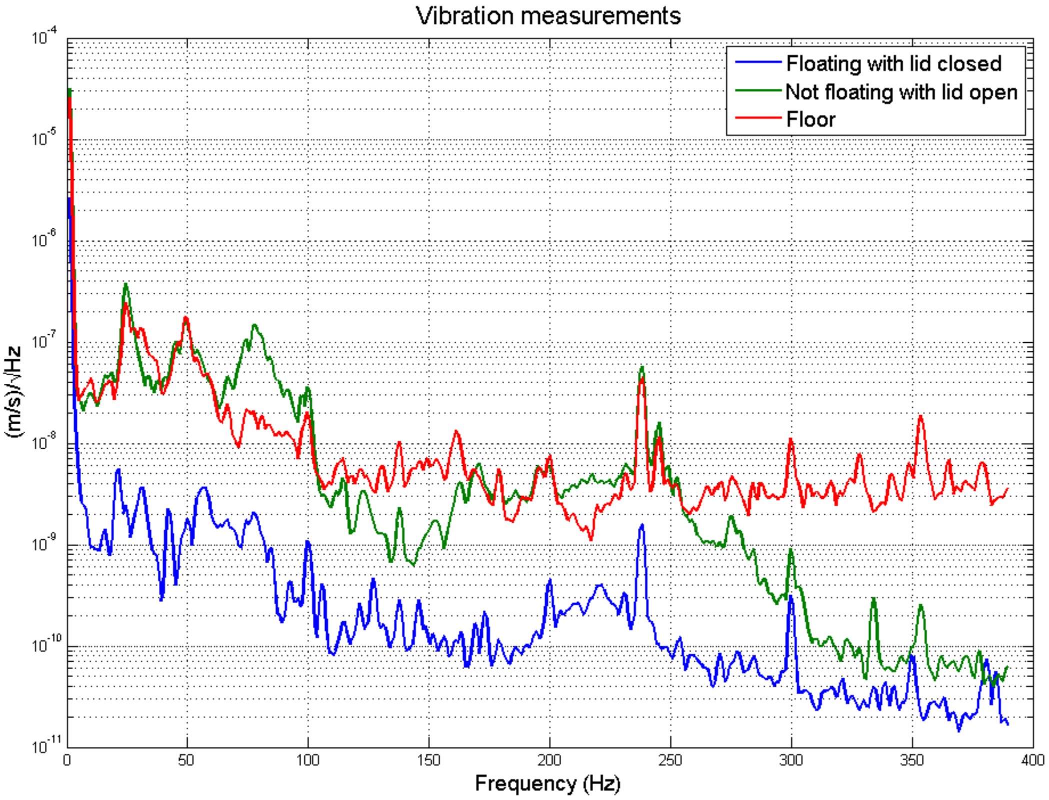

Figure 29. Low frequency vibration measurements of the system.

The graphs show the performance of the vibration and acoustic isolation scheme. Shown are three spectra acquired on the floor next to the system (red), on the concrete block with the acoustic lid open and the pneumatic legs inactive (green) and on the concrete block with the acoustic lid closed and active isolators (blue). These numbers compare well to measurements done at other leading SPM laboratories [78].

What I would have done or recommend doing differently

Coarse Z retraction

It is not fully understood why, but when the microscope is cold, the coarse Z positioner cannot be pulled up, away from the sample. Usually this is not a problem since the ~15 $\mu m$of the scanner are safe enough for He transfers, rotating the head and general meddling with the cables. In addition, thermal expansion and contraction result in the tip and sample separating by about 200 μmupon cooling from 4K to room temperature, so a tip will survive if the warming is done carefully enough.

However, it would have been useful to have this option, for example for big lateral movements above an inclined sample. The main suspected causes for this are the relatively high resistance of the wires leading to the positioner which is higher than the recommended value by Attocube, and the mass of the rest of the stack and the sample holder (and stiffness of the wires perhaps).

Lower resistance to coarse positioners

As mentioned above, the wires leading to the positioners have a higher resistance than recommended. For proper operation the "minus" wires of all three positioners had to be connected. In retrospective, lower resistance wires were better to use.

Sample-tip maximal distance

Out of inexperience, the sample and tip were designed to have a maximal distance which is only half the travel of the coarse Z positioner. This imposes an unnecessary limitation on the height of the sample and the tip. A future design should use the full range of the positioner.

More emphasis on the sample

At the time the microscope was designed, SOT's for 4K use were not yet available and the main focus was the development of the tool. Changing samples was then a very rare event, and the wires leading to the sample were regarded as "less important". Nowadays, the emphasis has shifted to conducting experiments with physical merit and the samples are the main issue.

If I could change the microscope design I would make changing samples an easier and less risky process than it is today. I would also give more importance to the wires leading to the sample. I would've included more than 14 wires and perhaps make them coaxial, or at least make more of them twisted pairs.

Variable temperature

The microscope was not properly designed to work at variable temperature. Although it has a heater and thermometer we've found that heating the sample interferes dramatically with the signal and creates vibrations (perhaps turbulence in the exchange gas) which distort the image and risk the tip. Having this degree of freedom is highly useful for many experiments and is worth investing in.

Microscope schematics

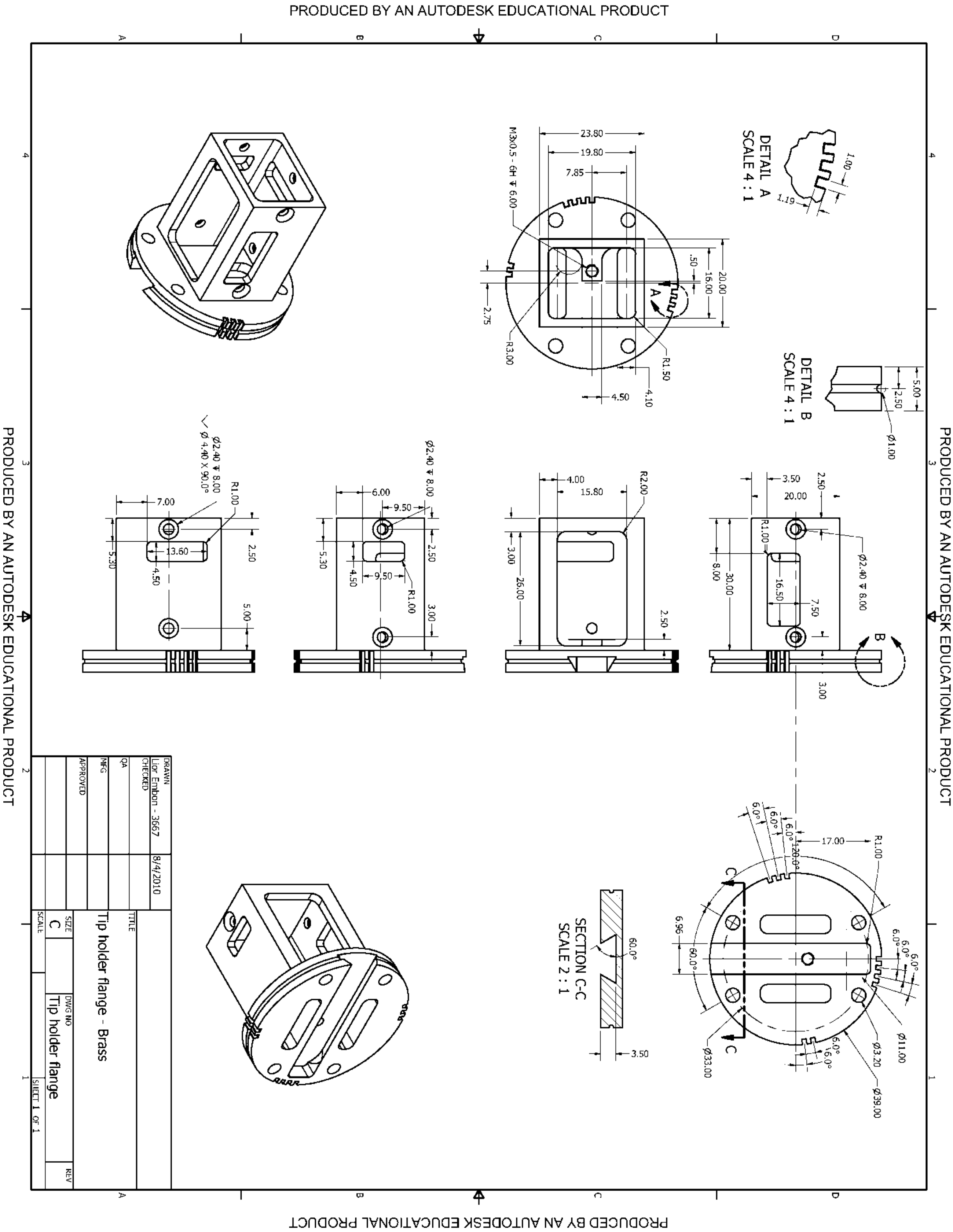

Figure 30. Tip holder flange schematics

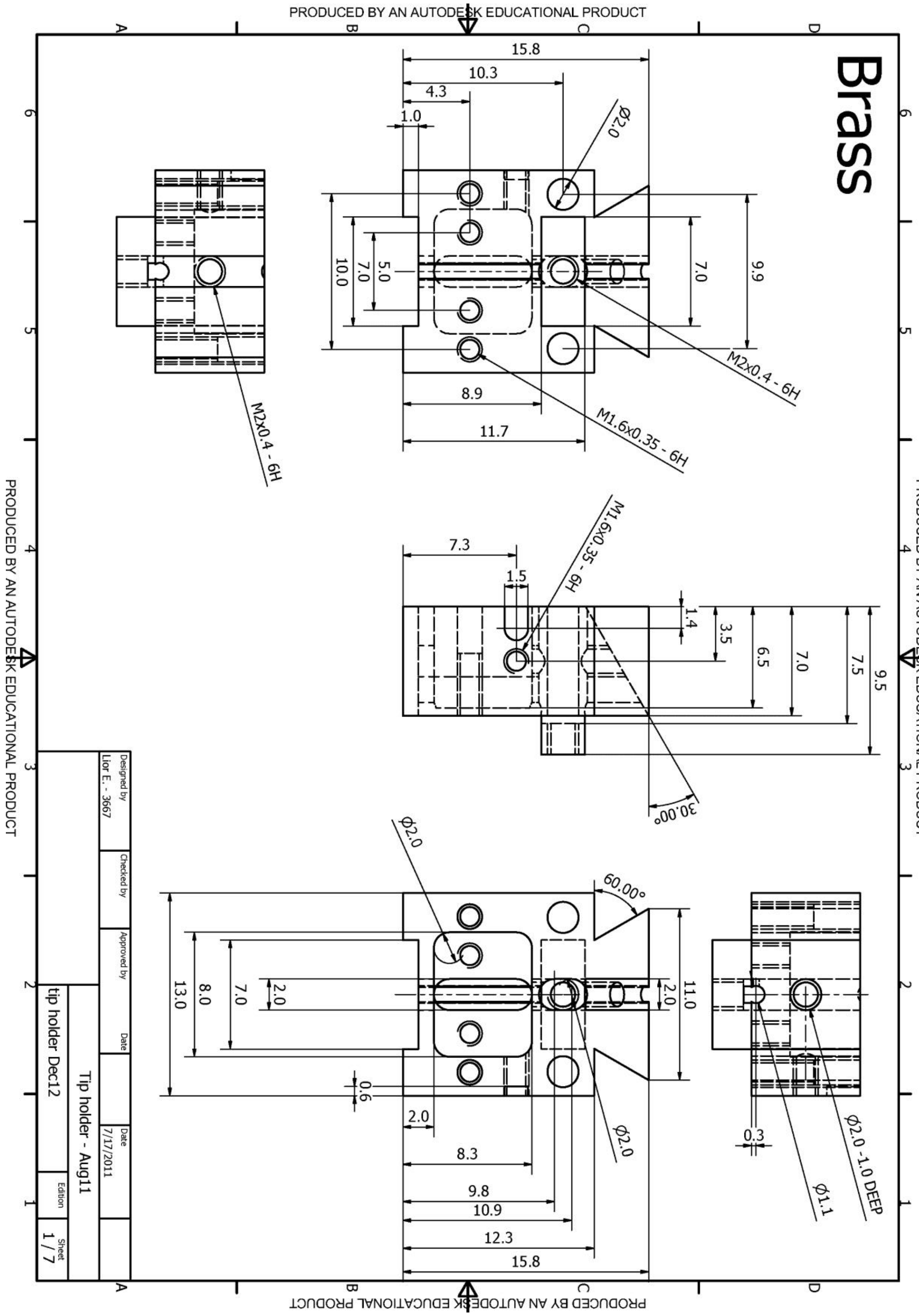

Figure 31. Tip holder schematics I

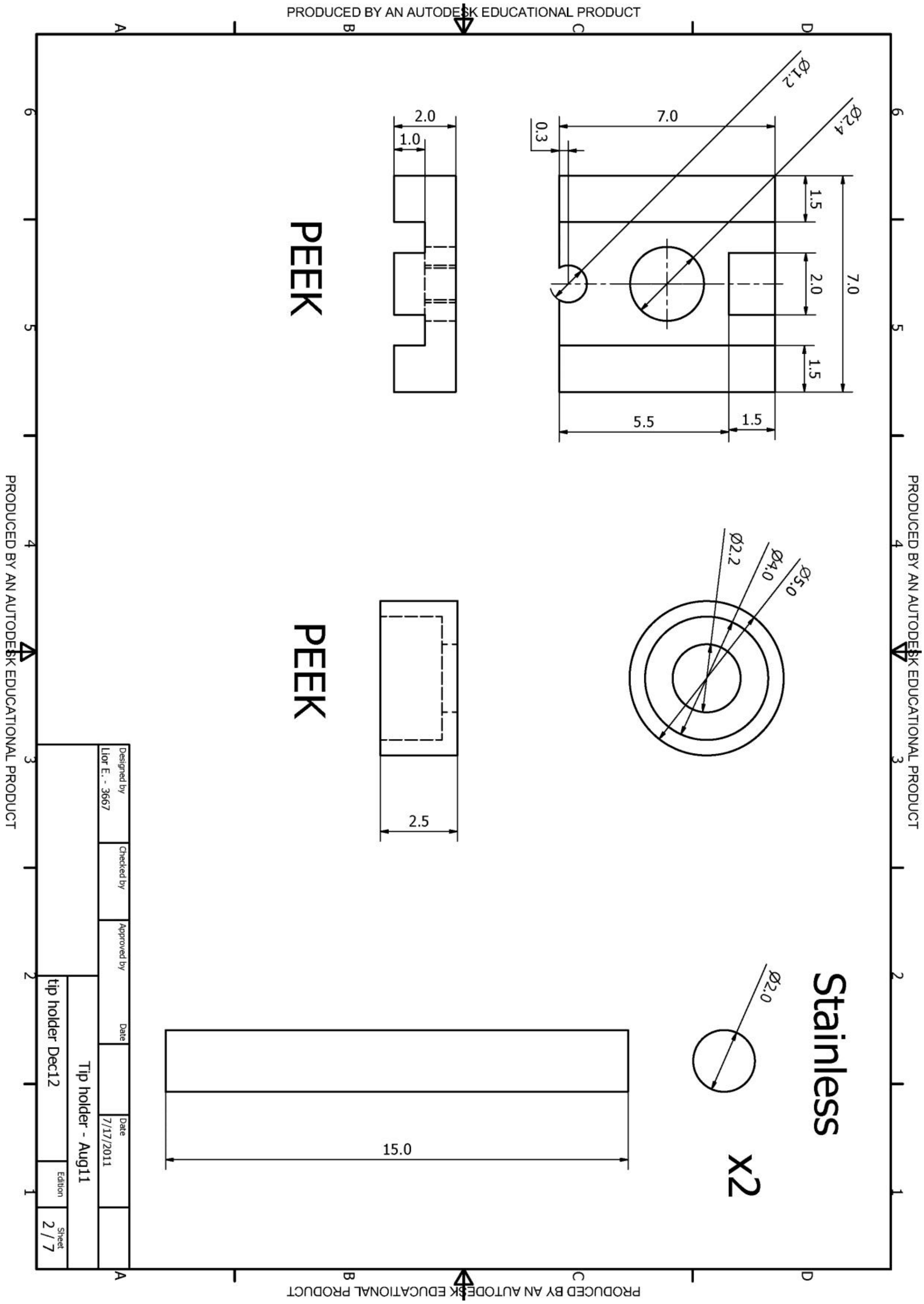

Figure 32. Tip holder schematics II

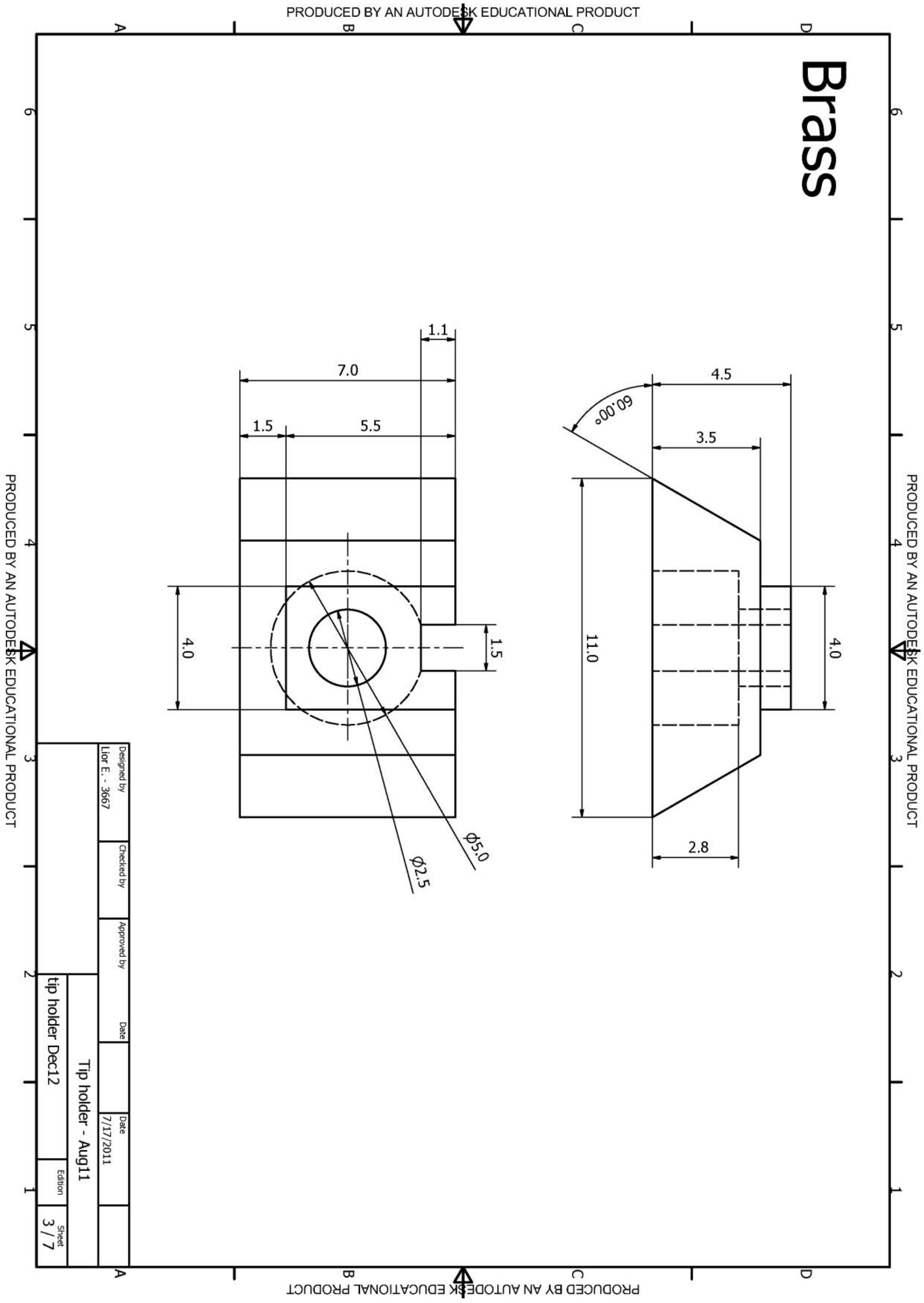

Figure 33. Tip holder schematics III

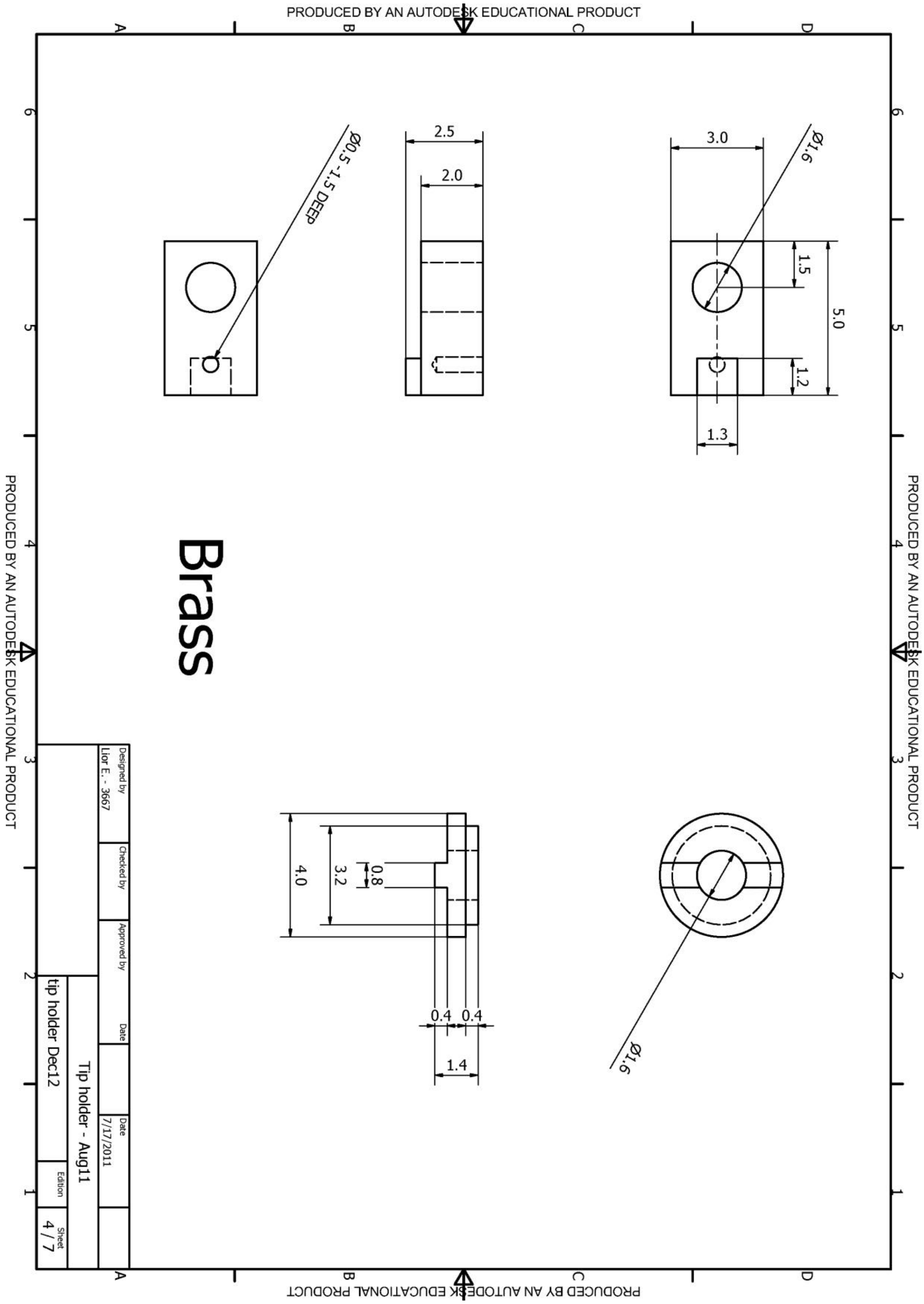

Figure 34. Tip holder schematics IV

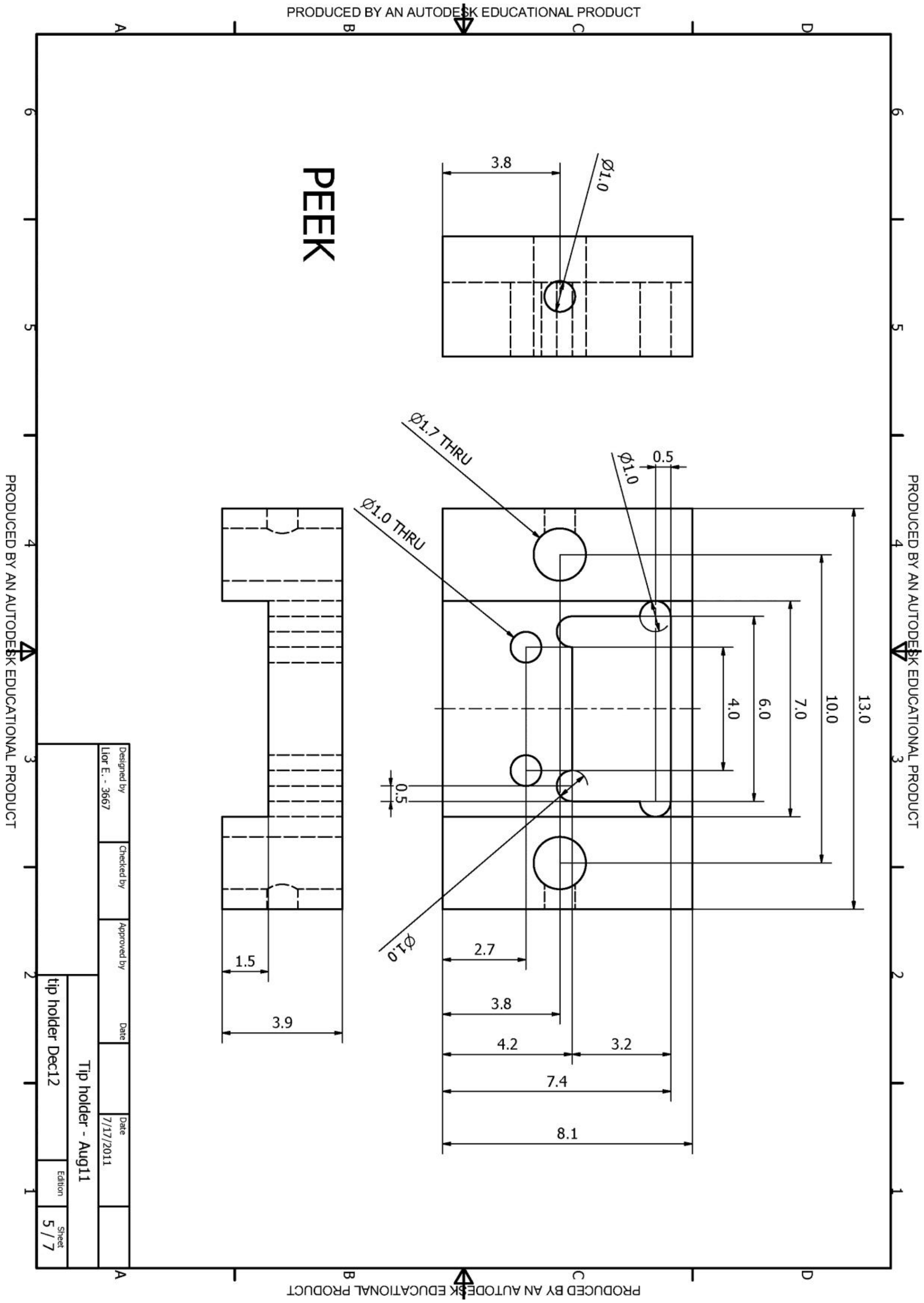

Figure 35. Tip holder schematics V

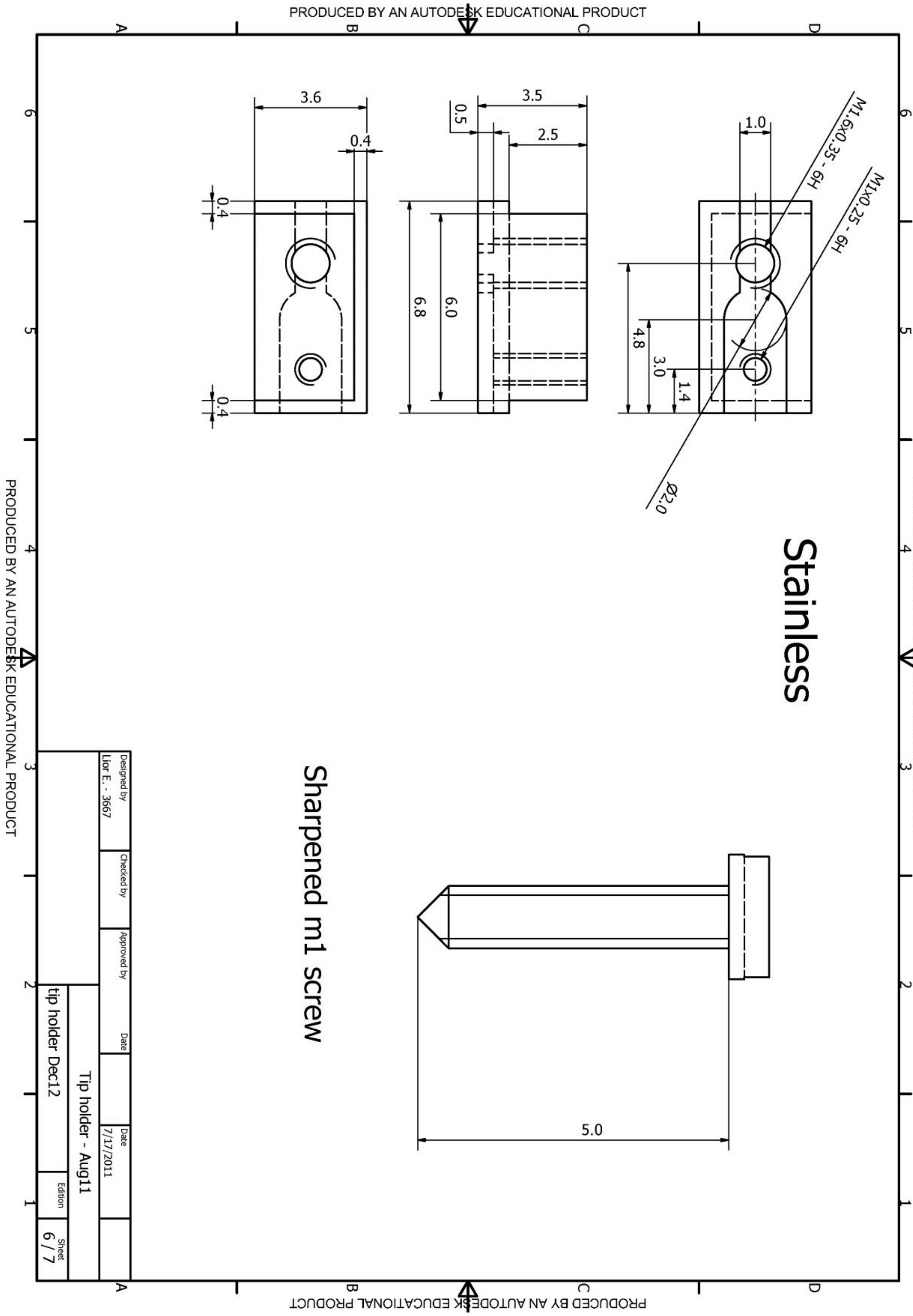

Figure 36. . Tip holder schematics VI

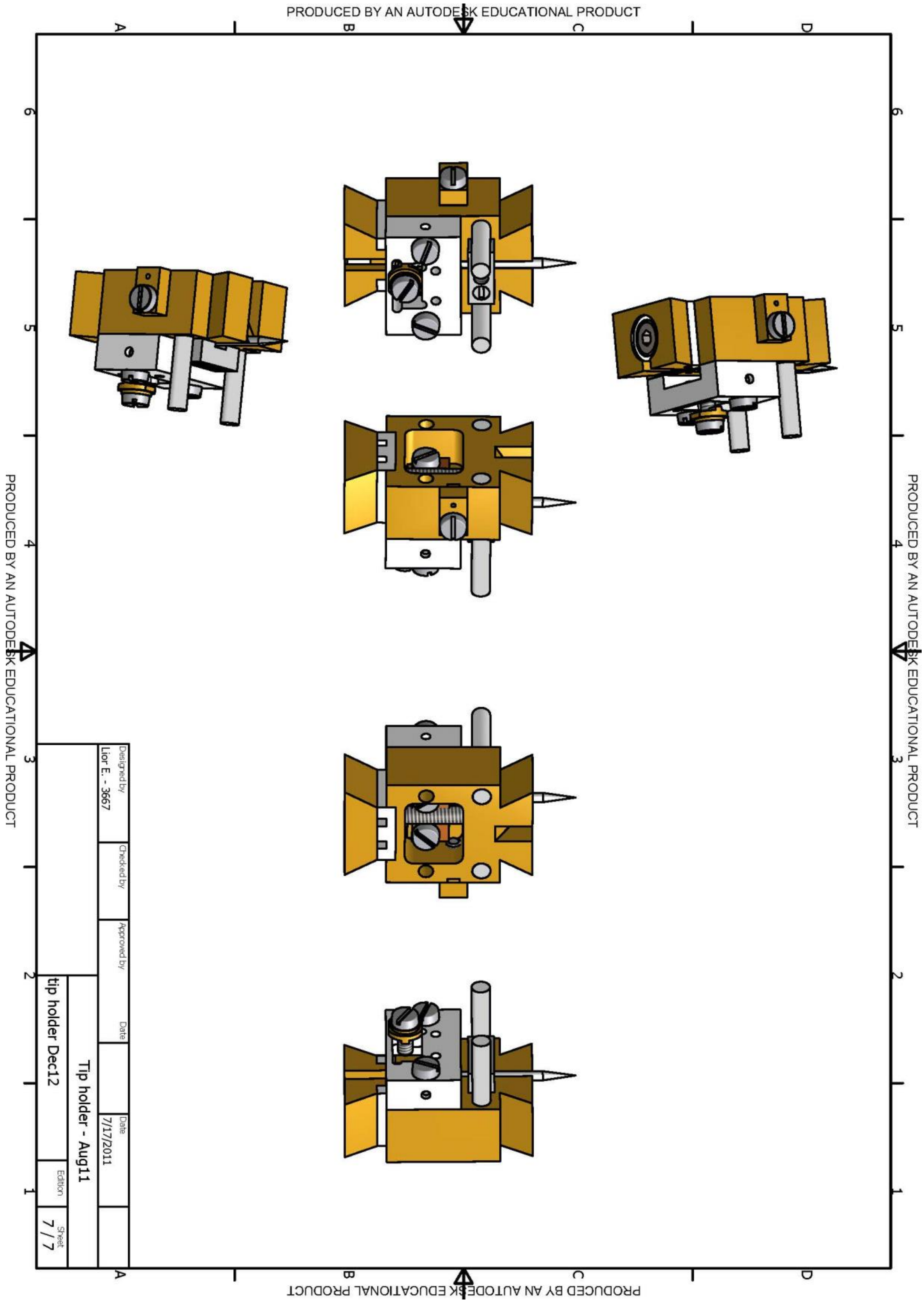

Figure 37. Tip holder schematics VII

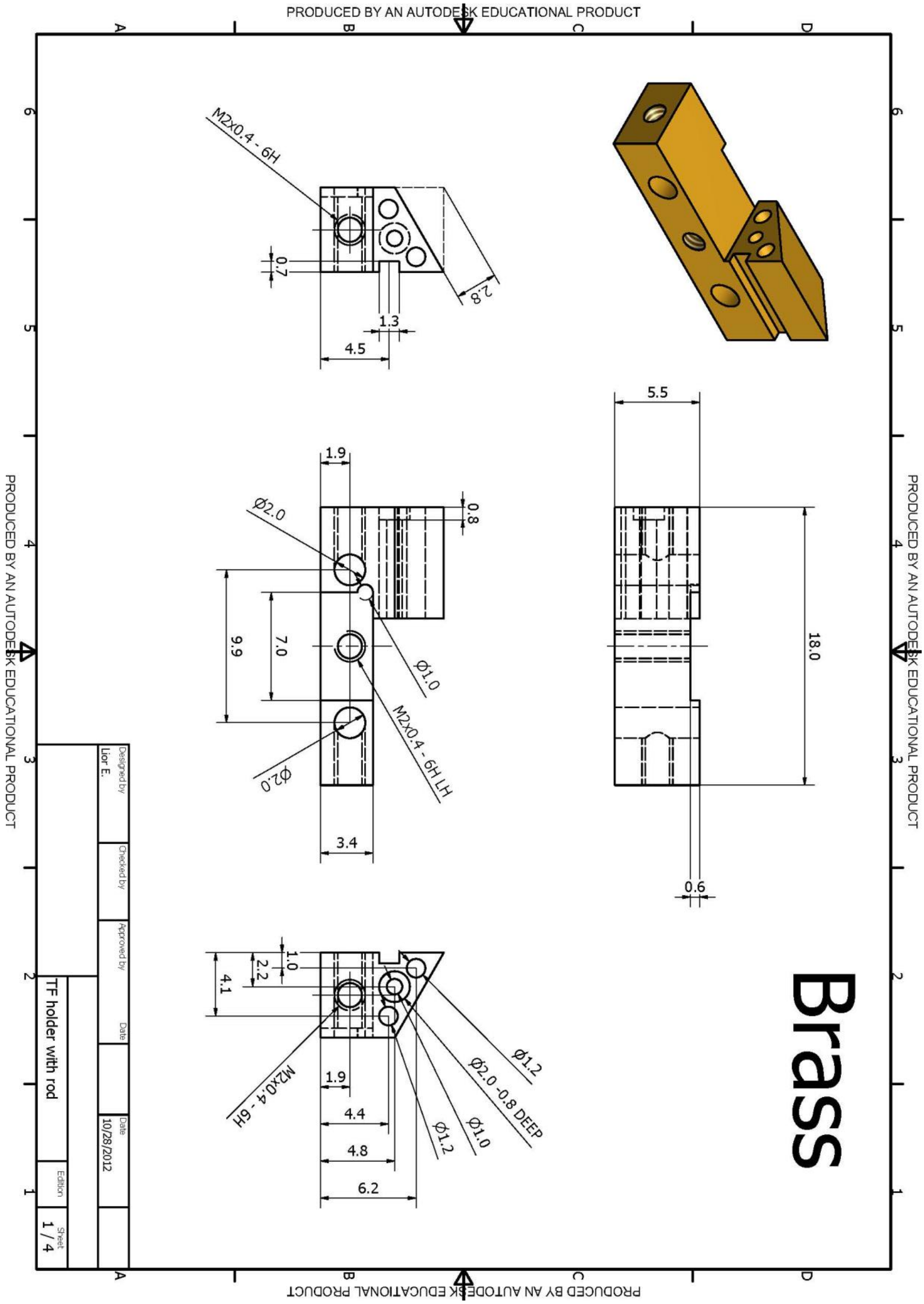

Figure 38. Tuning fork holder schematics I

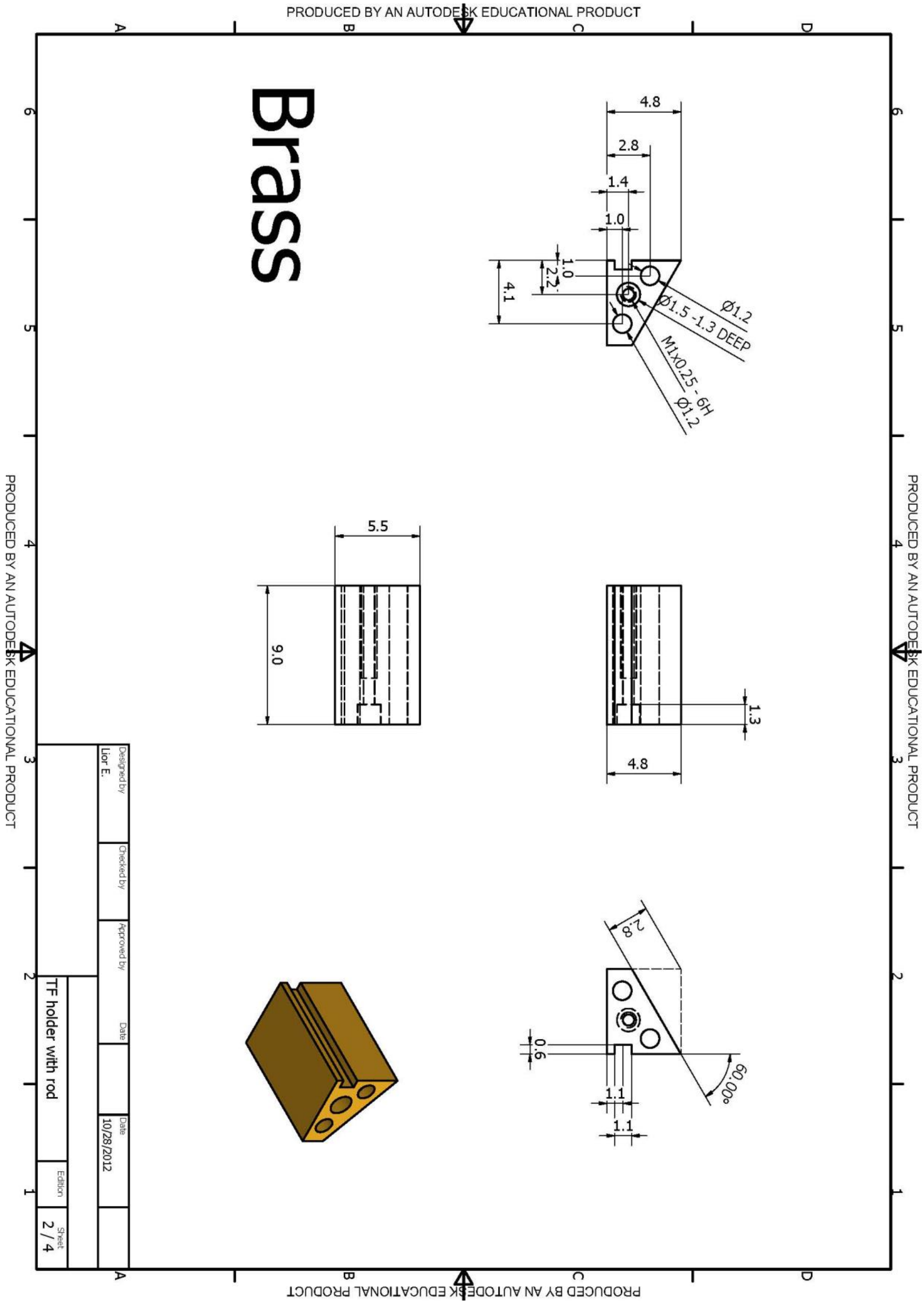

Figure 39. Tuning fork holder schematics II

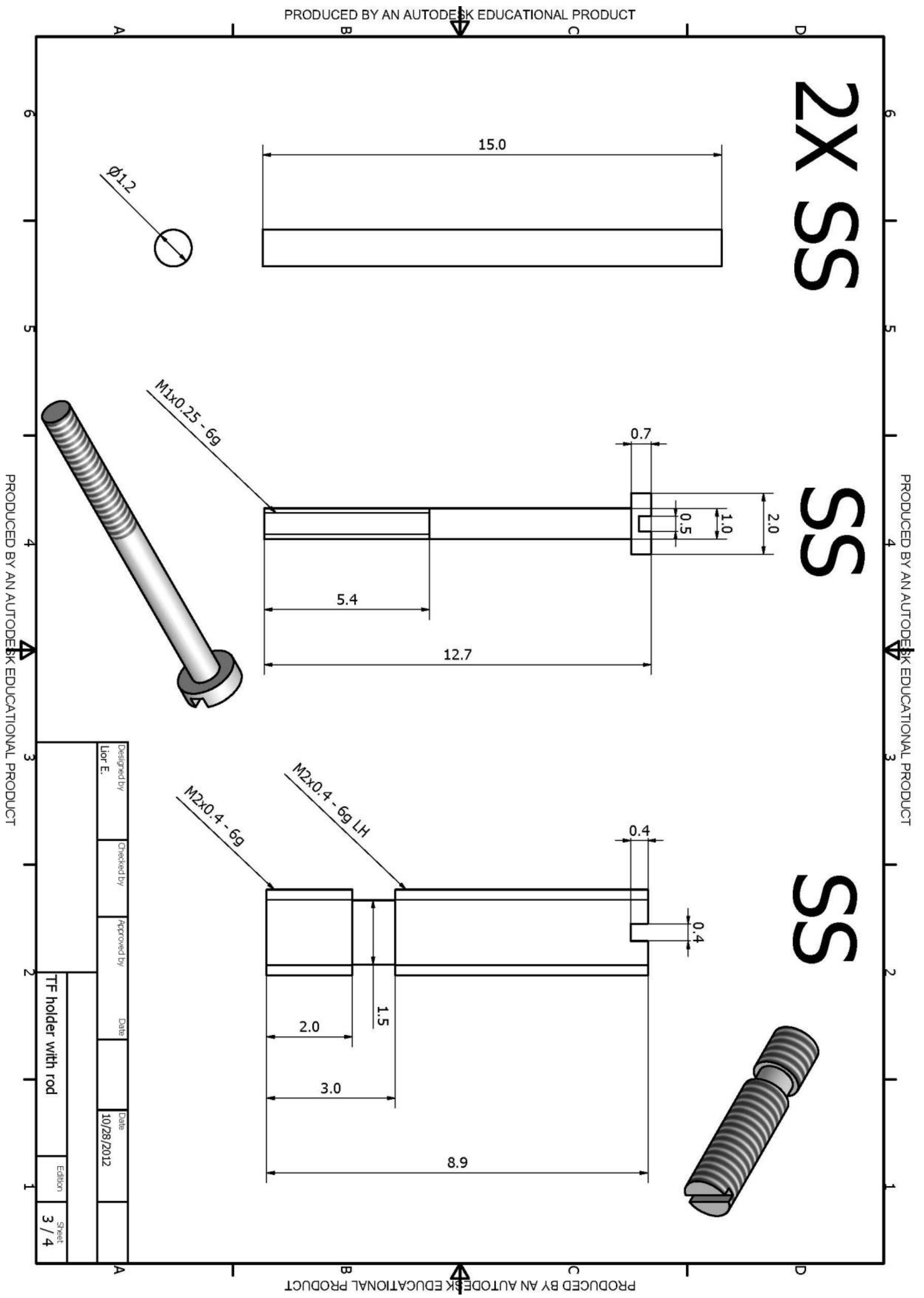

Figure 40. Tuning fork holder schematics III

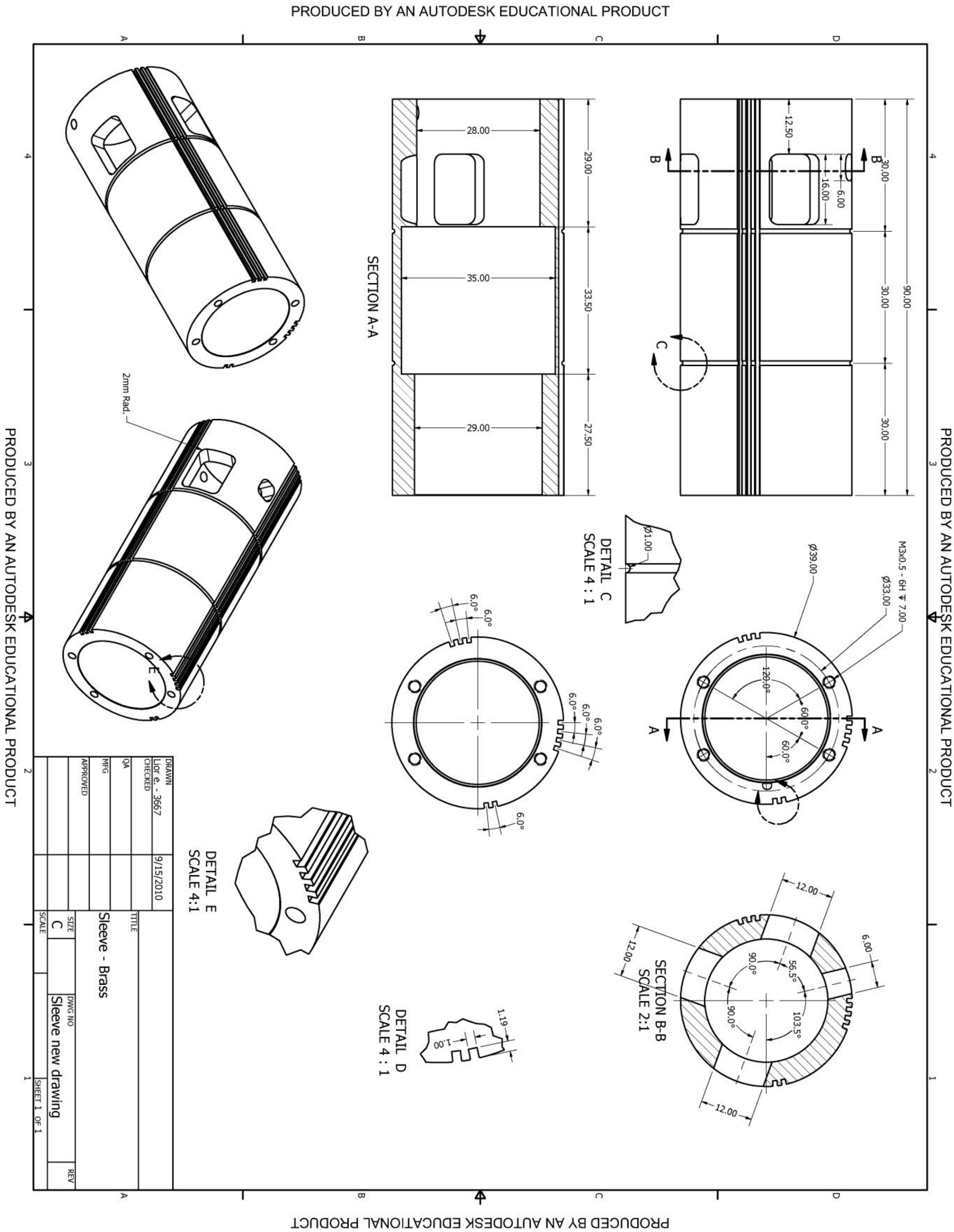

Figure 41. Protective shield schematics

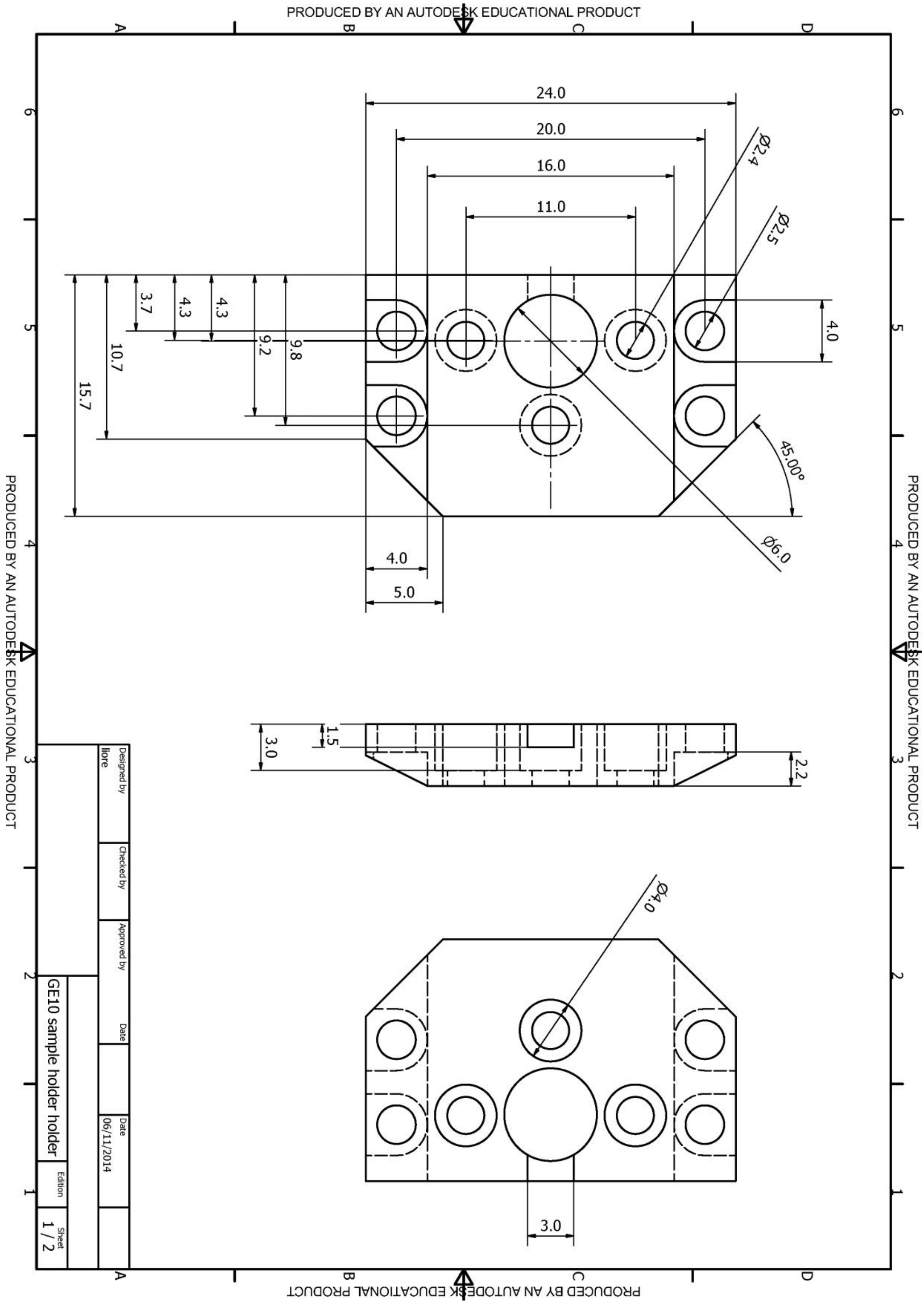

Figure 42. Sample holder schematics I

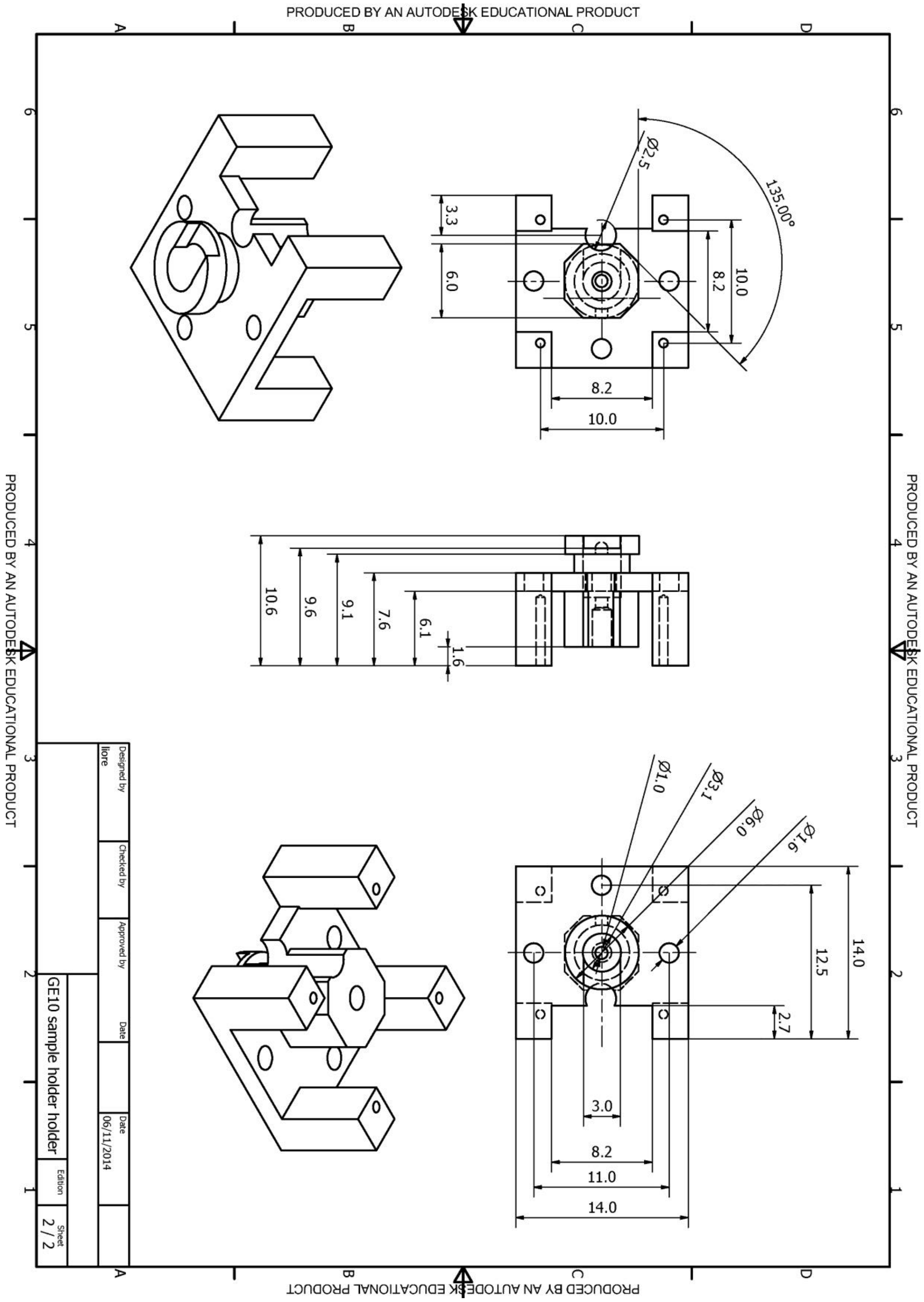

Figure 43. Sample holder schematics II

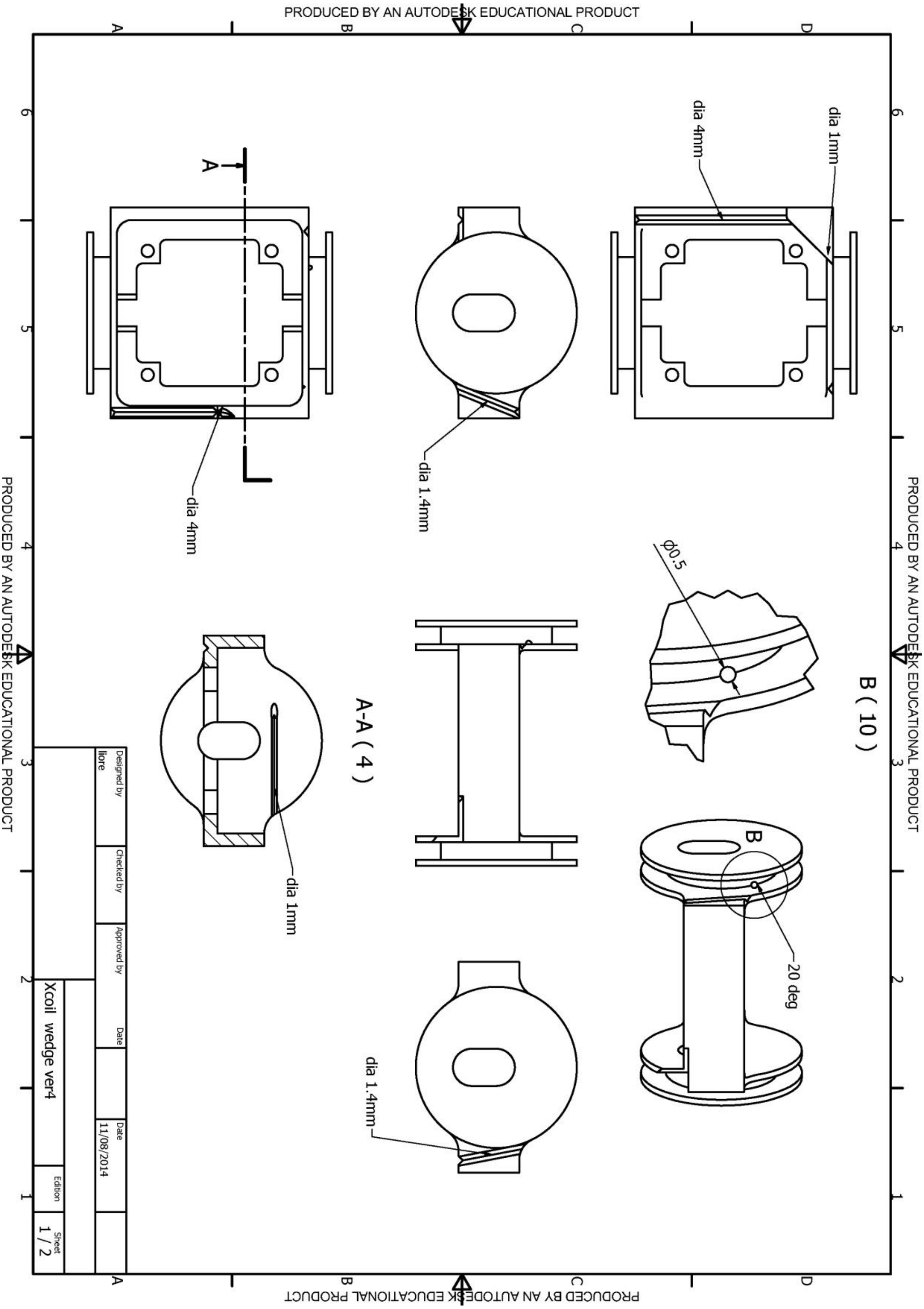

Figure 44. X coil schematics

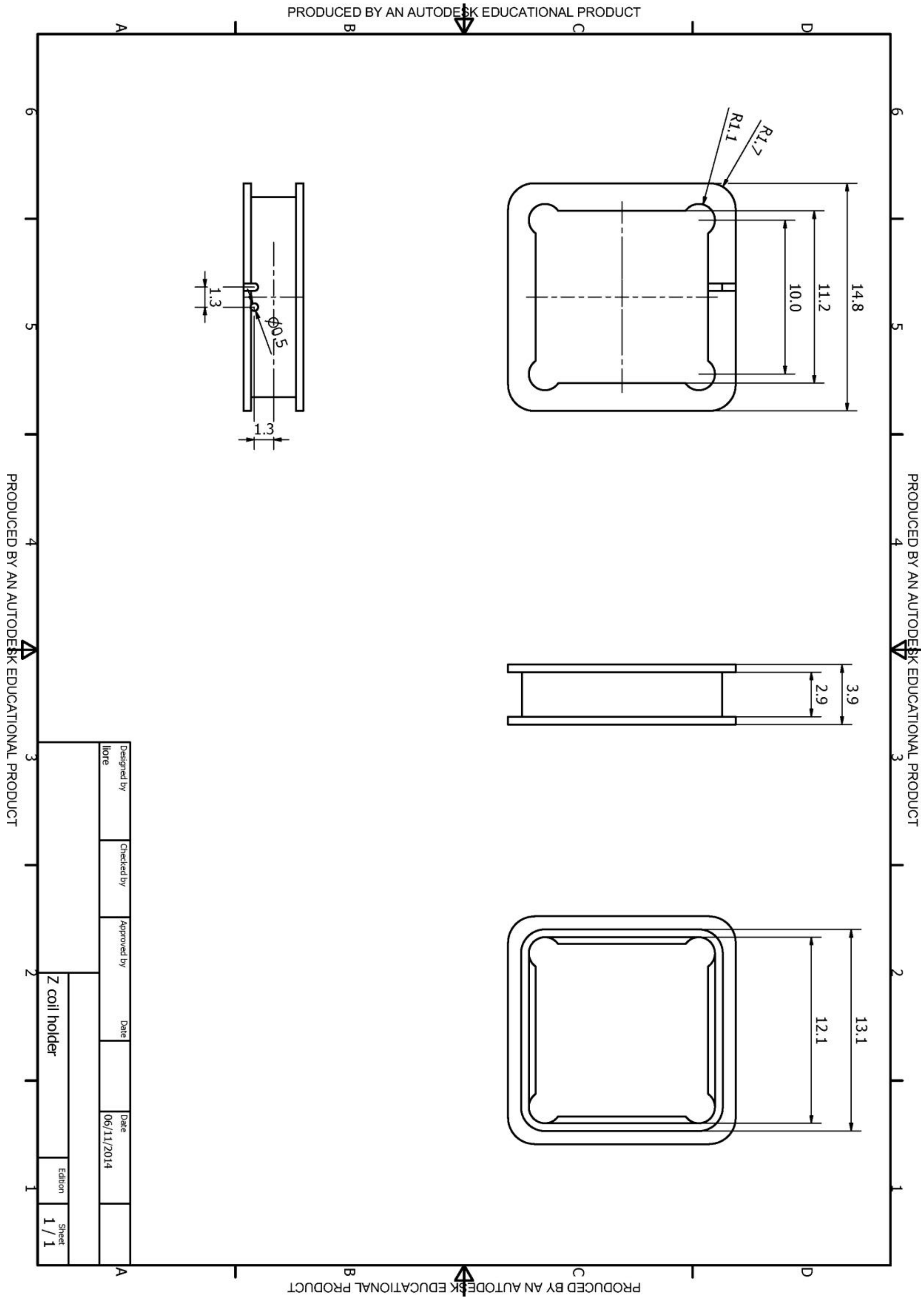

Figure 45. Z coil schematics

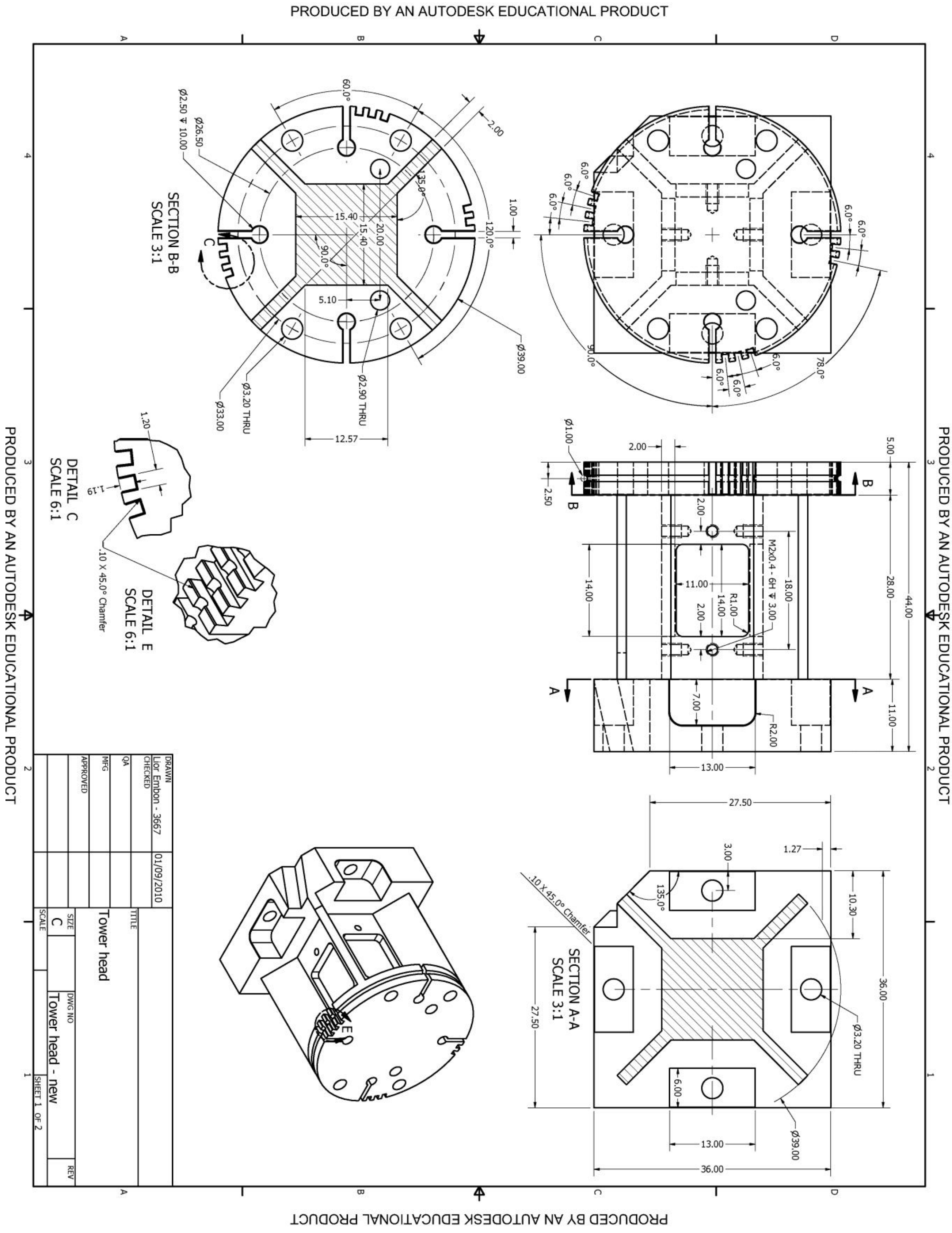

Figure 46. Microscope base schematics

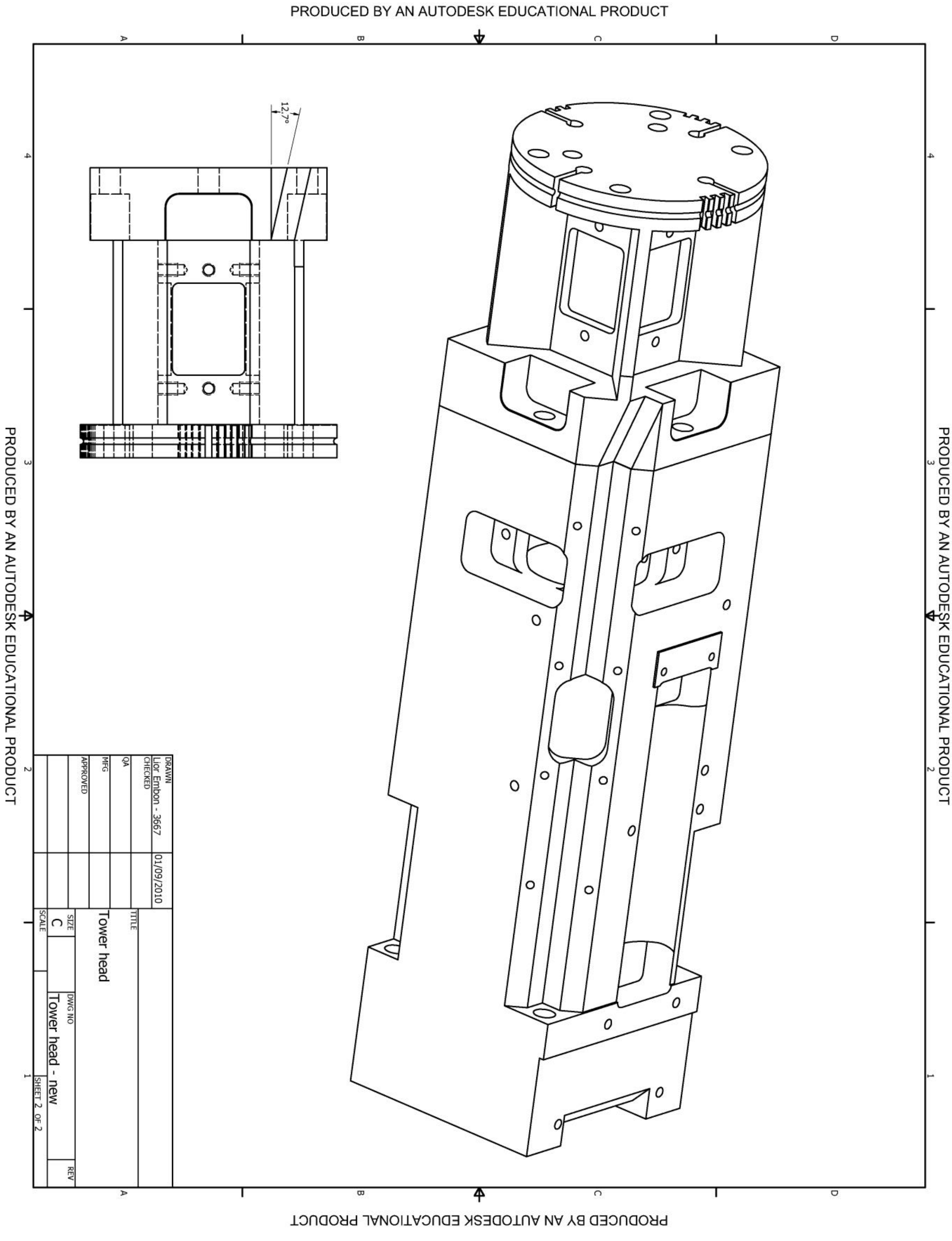

Figure 47. Microscope base and body schematics

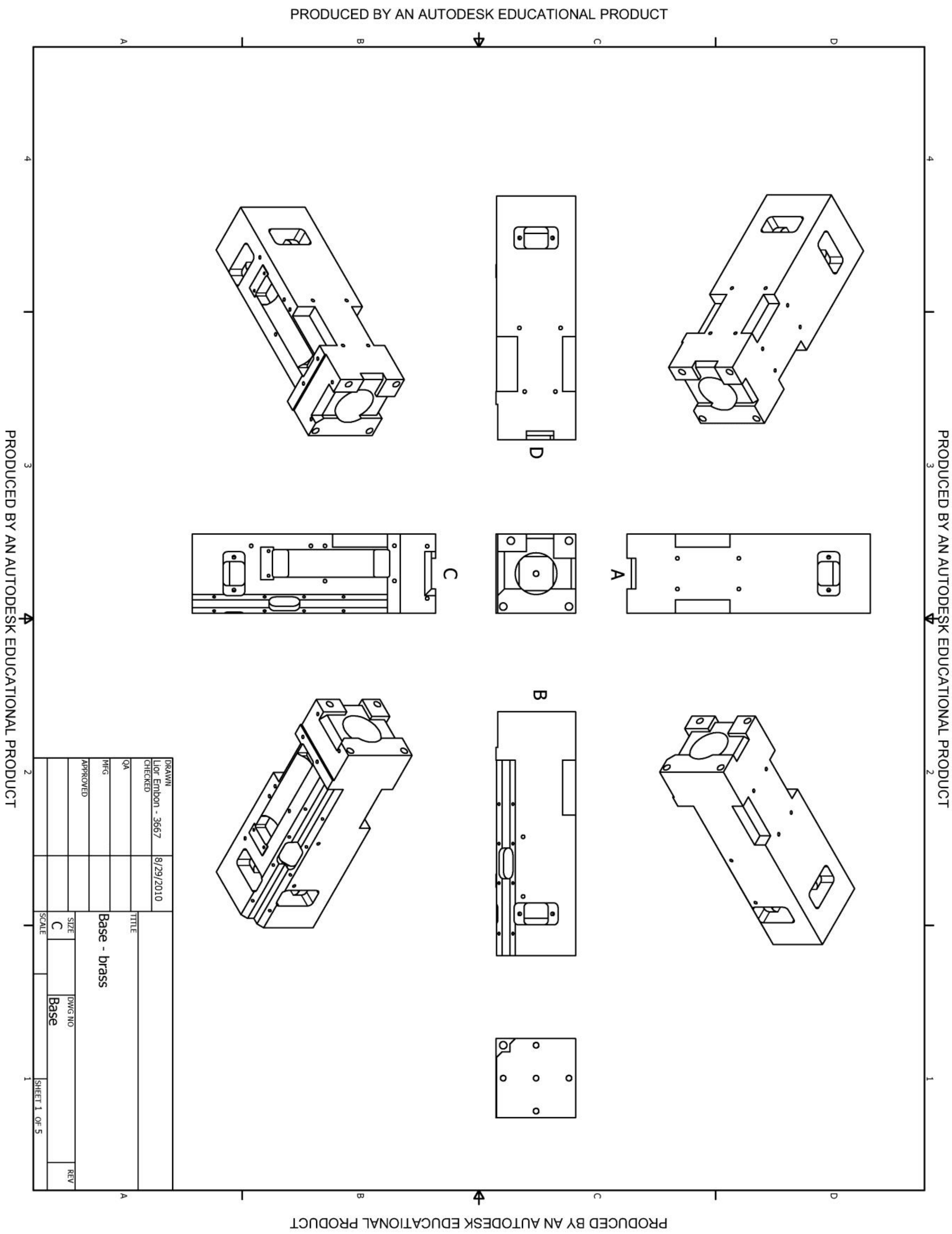

Figure 48. Microscope body schematics I

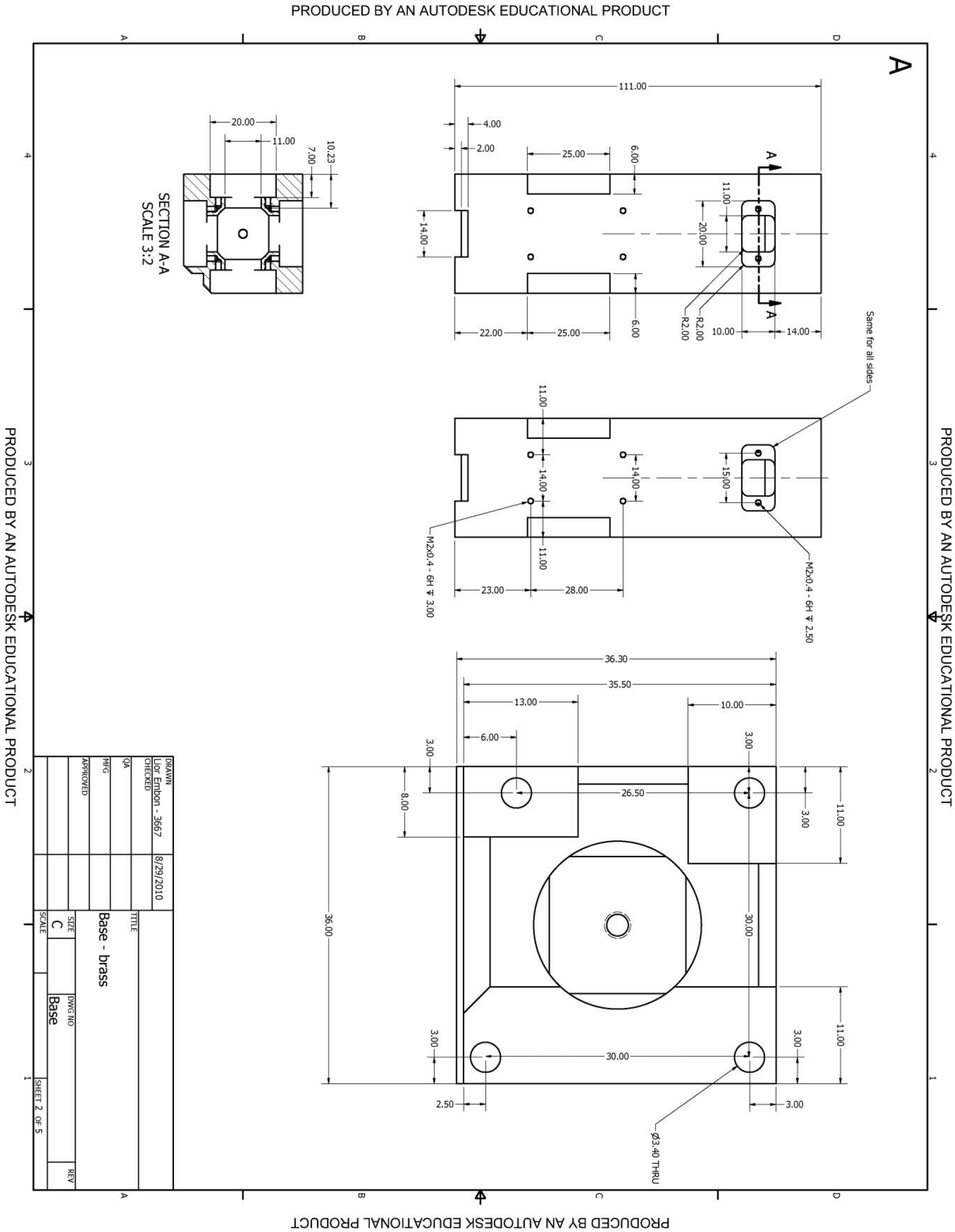

Figure 49. Microscope body schematics II

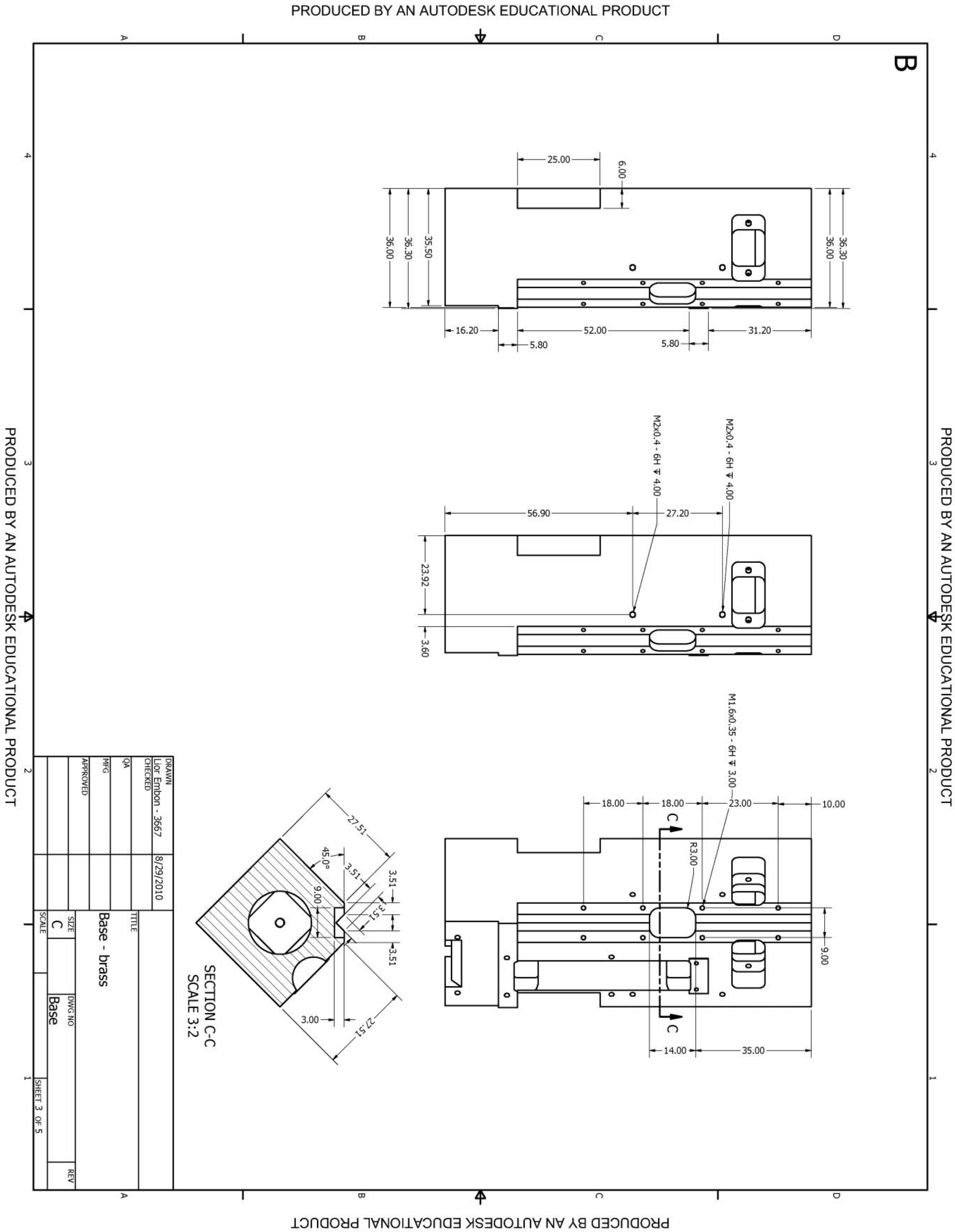

Figure 50. Microscope body schematics III

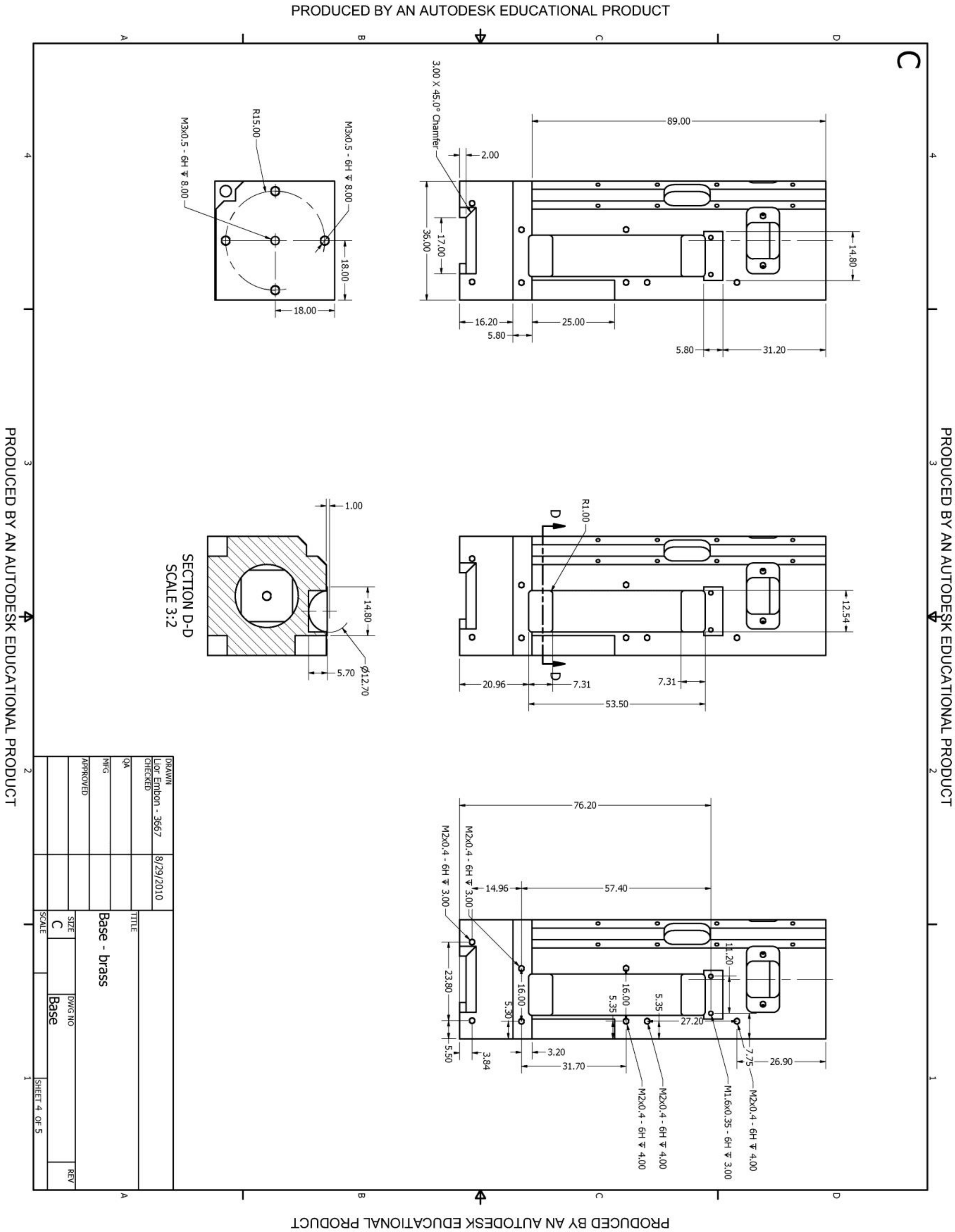

Figure 51. Microscope body schematics IV

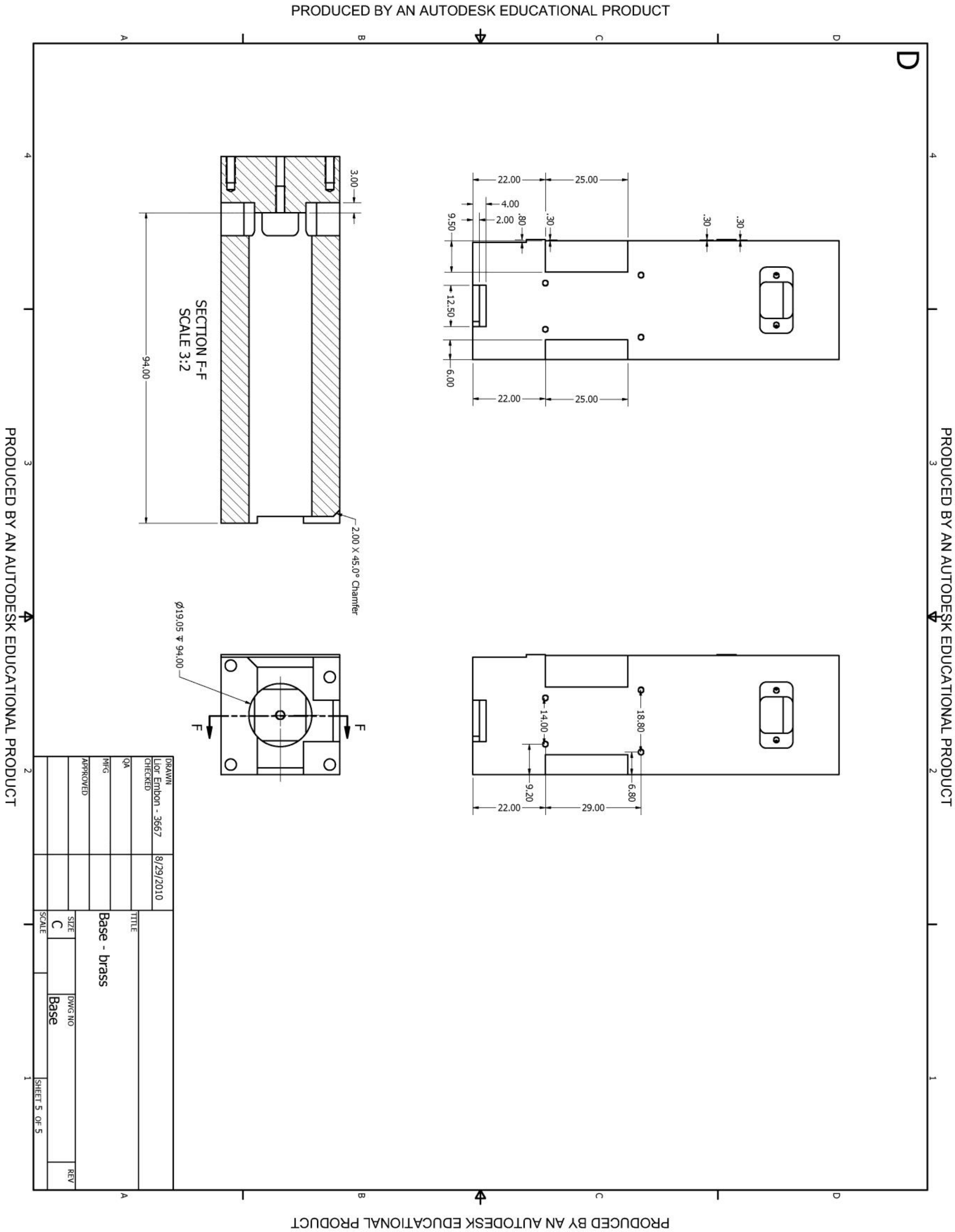

Figure 52. Microscope body schematics V

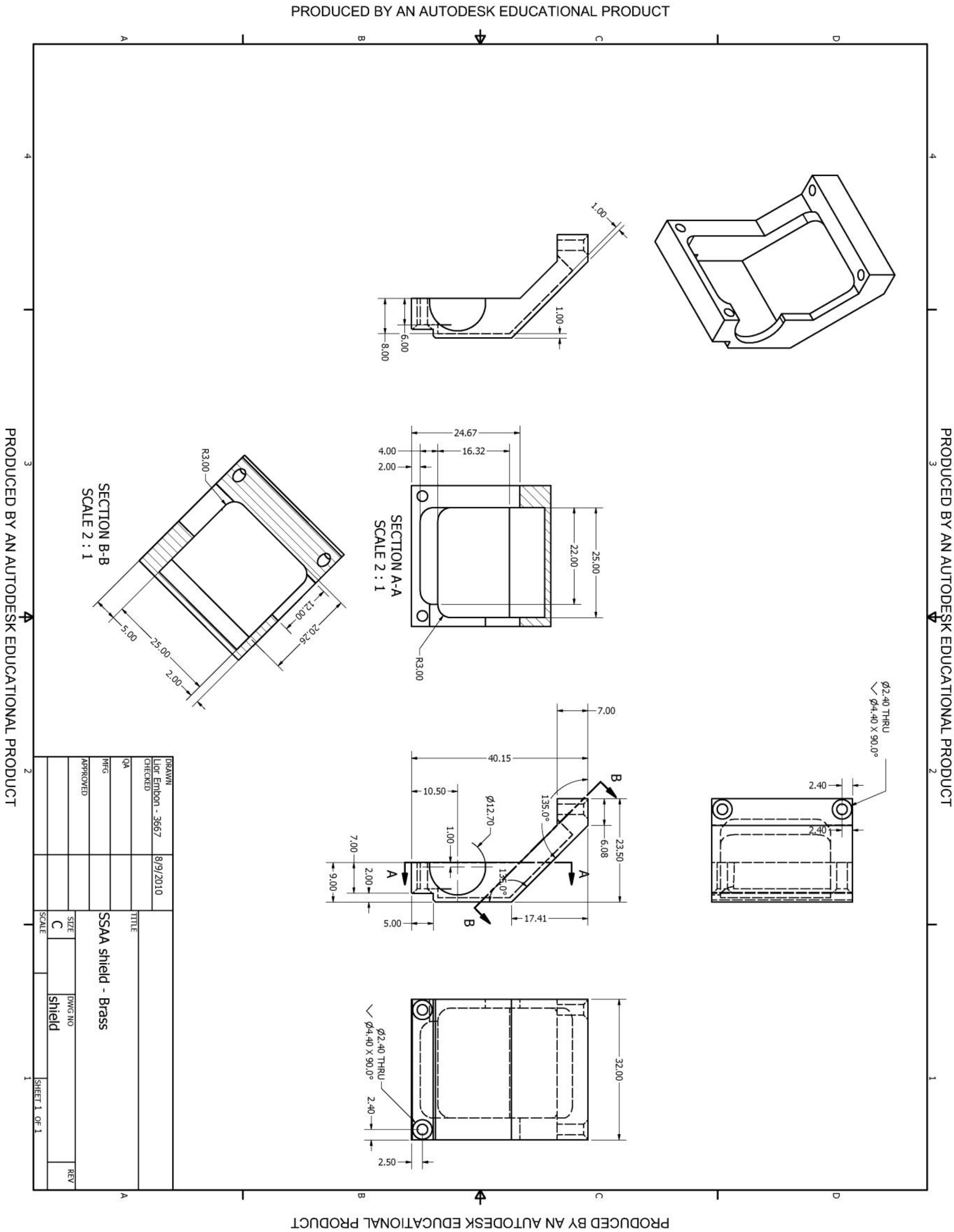

Figure 53. SOT PCB shield schematics

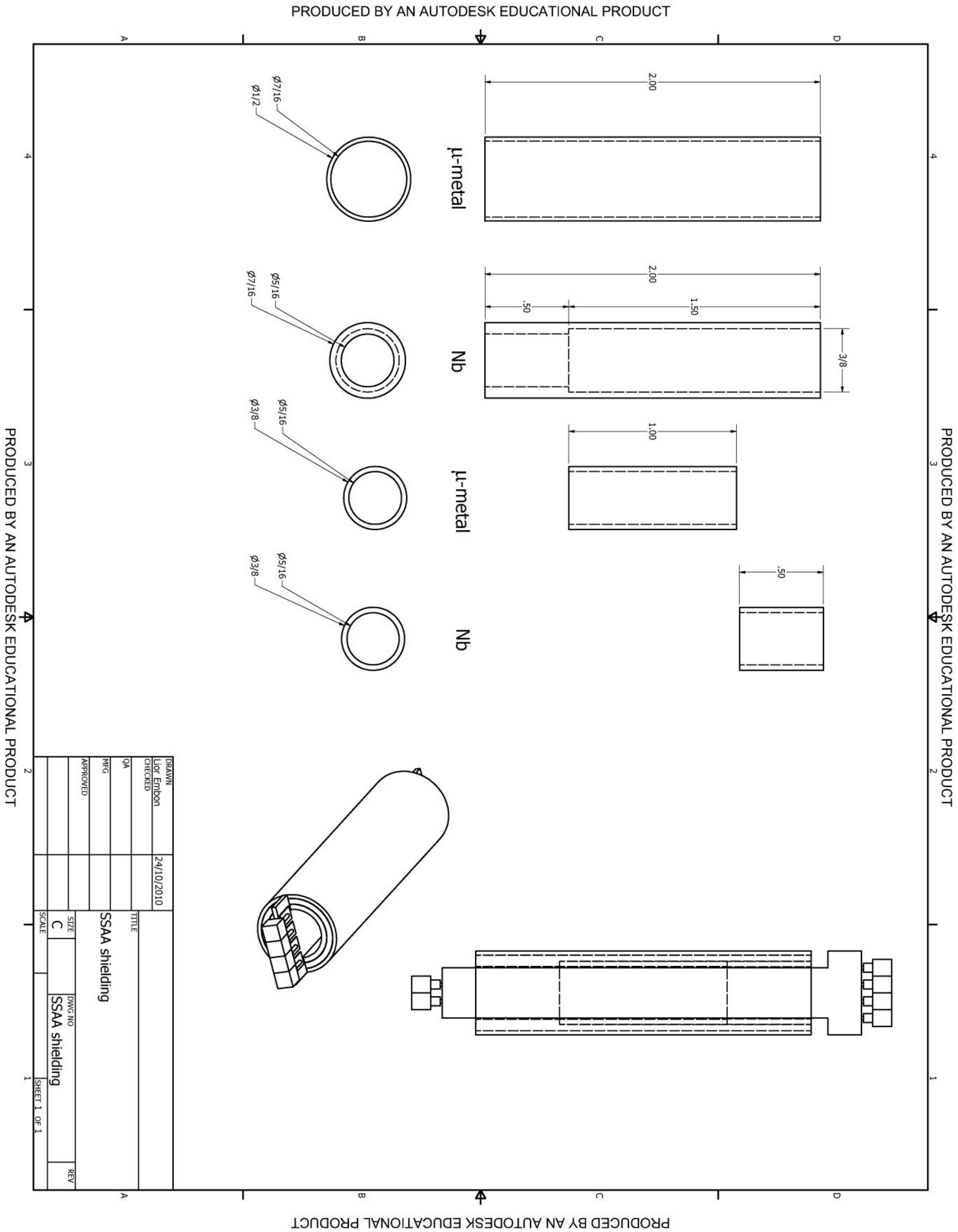

Figure 54. SSAA shield schematics

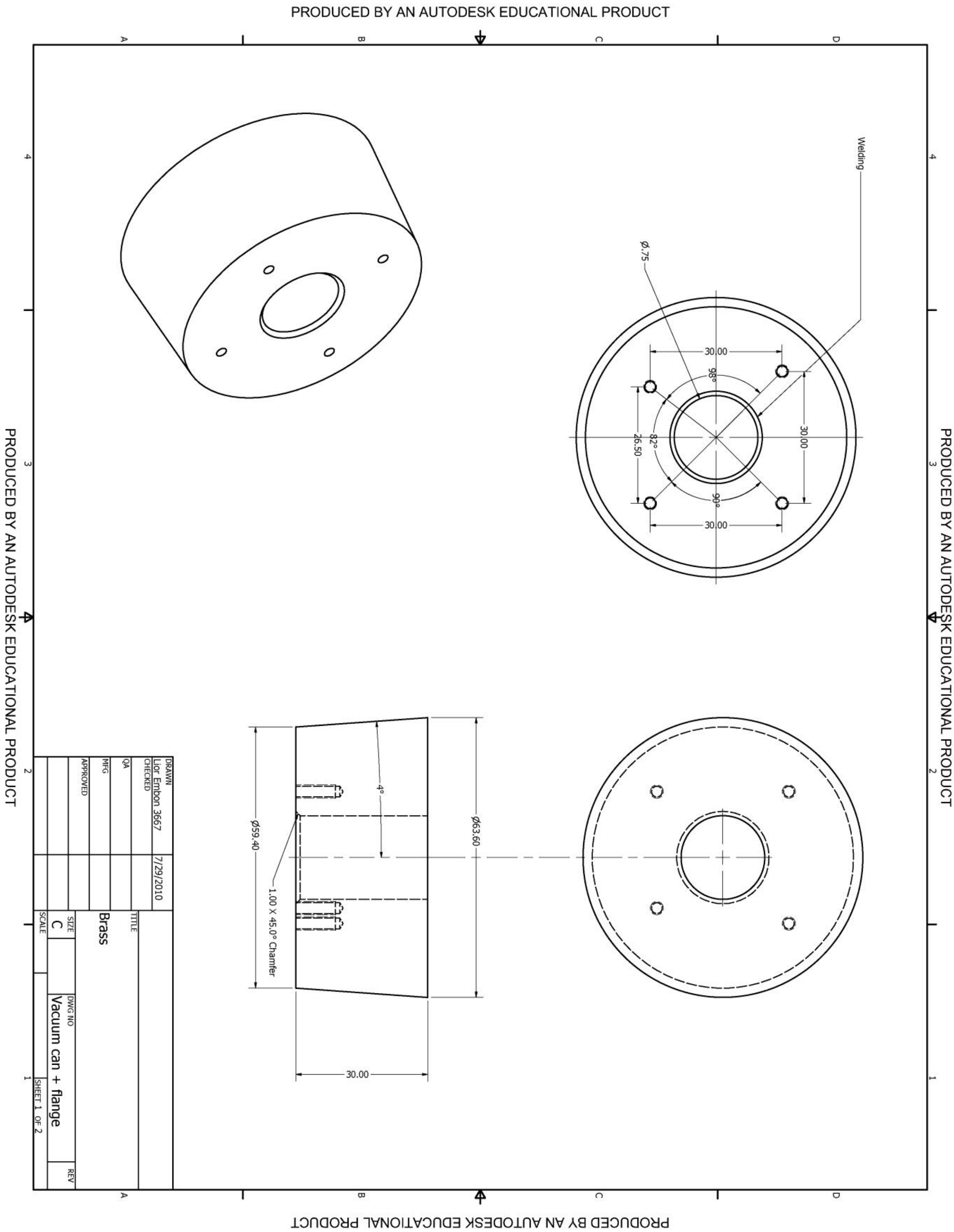

Figure 55. Sealing cone schematics

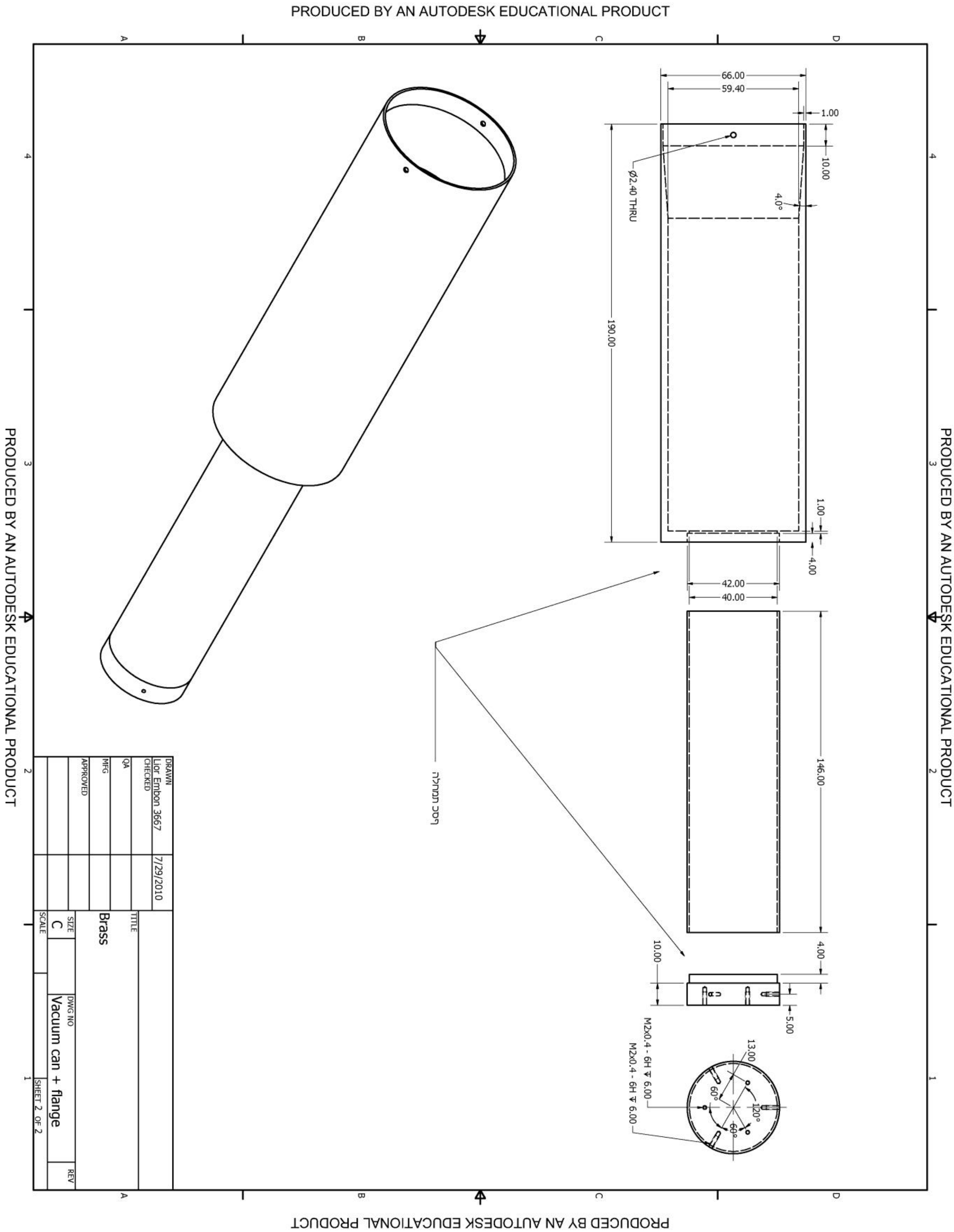

Figure 56. Vacuum can schematics

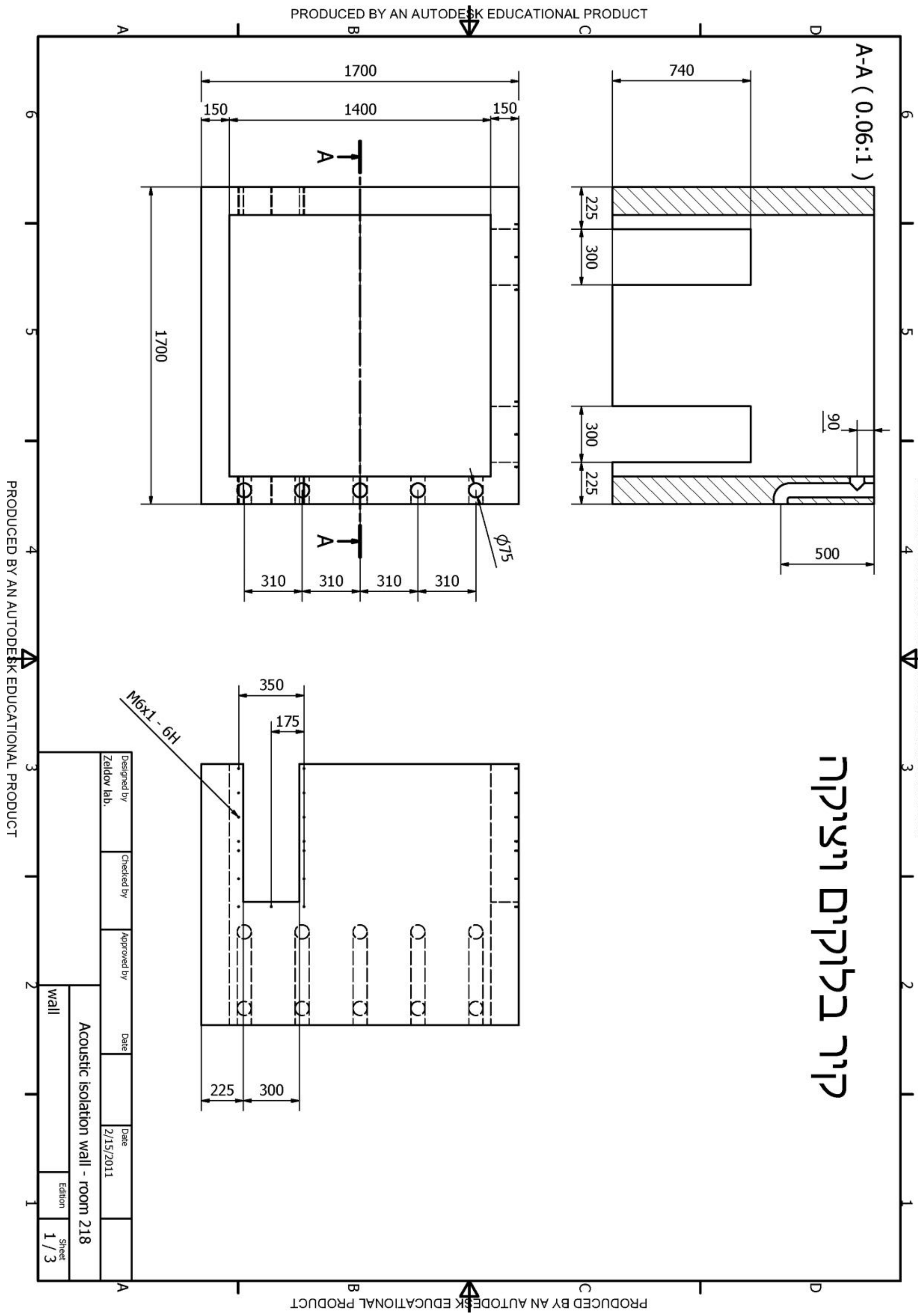

Figure 57. Acoustic wall schematics I

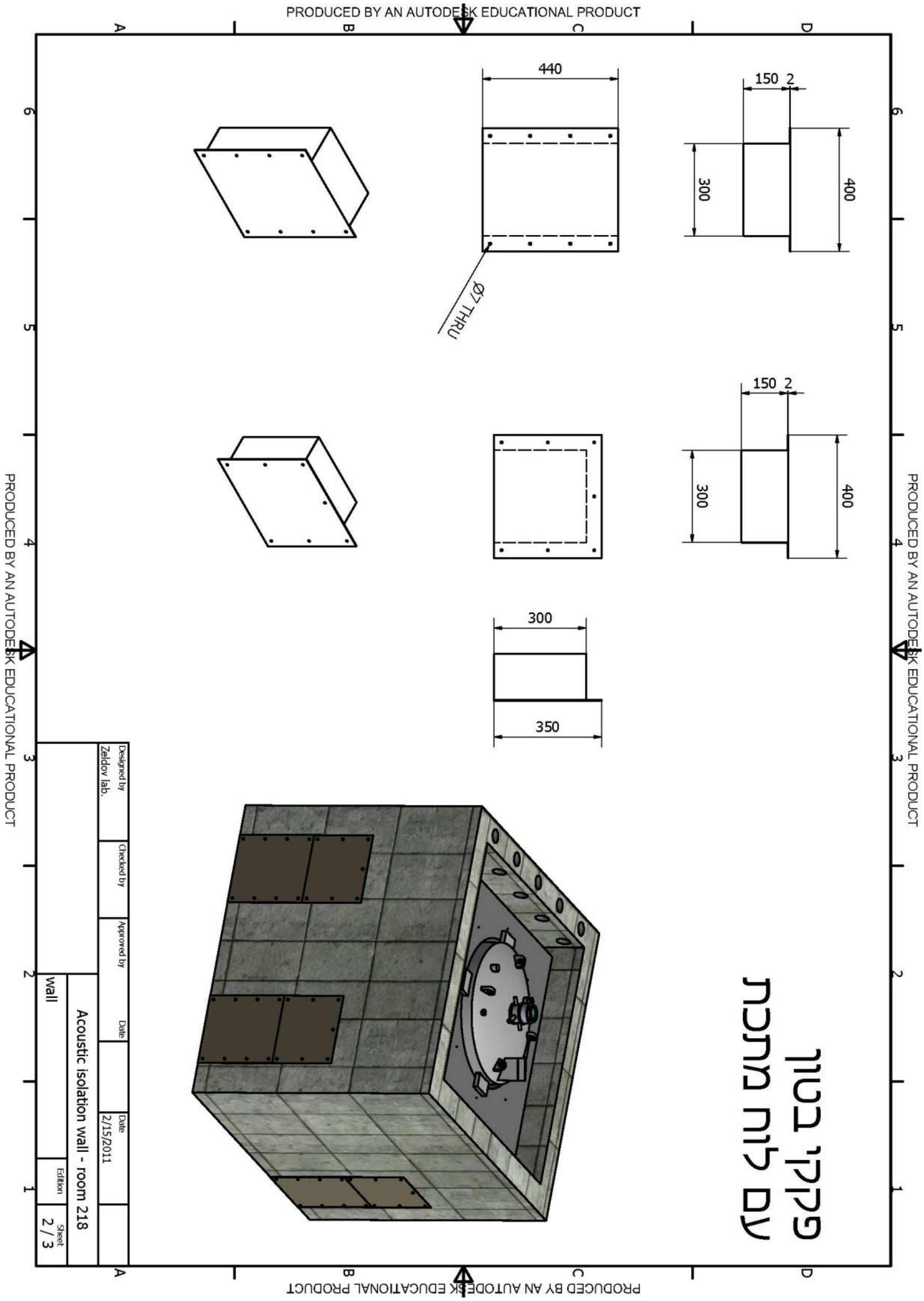

Figure 58. Acoustic wall schematics II

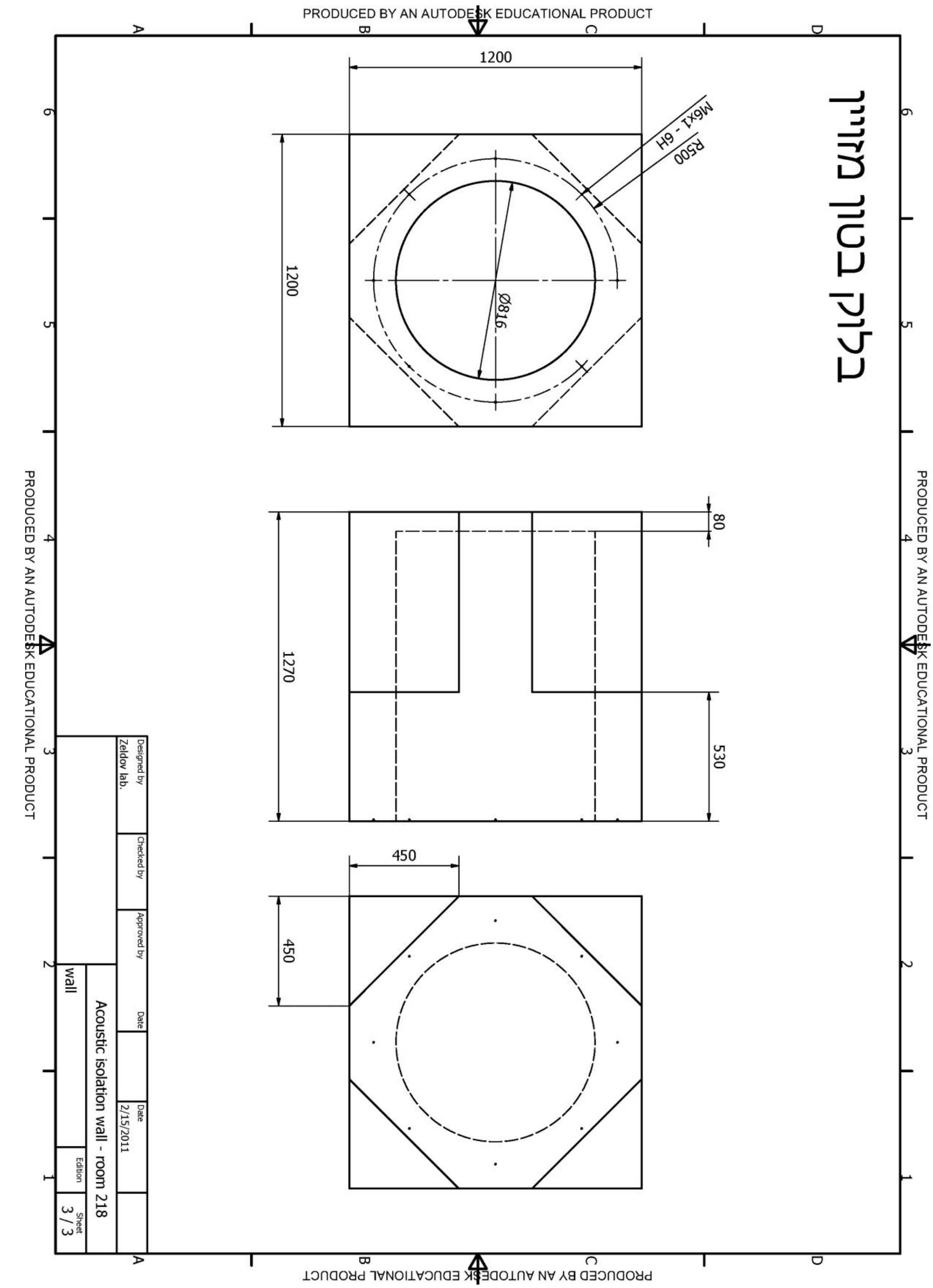

Figure 59. Vibration isolation concrete block schematics

List of publications

1. Eyal, O. Pelleg, **L. Embon**, E. Polturak, Evidence for a High-Temperature Disorder-Induced Mobility in Solid ^{4}He, *Phys. Rev. Lett.* **105**, 025301 (2010)
2. Vasyukov, D., Anahory, Y., **Embon, L.**, Halbertal, D., Cuppens, J., Neeman, L., Finkler, A., Segev, Y., Myasoedov, Y., Rappaport, M. L., Huber, M. E. & Zeldov, E. A scanning superconducting quantum interference device with single electron spin sensitivity. *Nature Nanotech.* **8**, 639-644 (2013)
3. Reiner, J., Anahory, Y., **Embon, L.**, Myasoedov, Y. and Zeldov, E., "Sensor Device For Direct Magnetic Field Imaging", United States Provisional Patent Application No. 61/826,725 (2014)
4. Anahory, Y., Reiner, J., **Embon, L.**, Halbertal, D., Yakovenko, A., Myasoedov, Y., Rappaport, M.L., Huber, M.E. and Zeldov, E., Three-junction SQUID-on-tip with tunable in-plane and out-of-plane magnetic field sensitivity. *Nano. Lett.* **14**(11), 6481-6487 (2014)
5. **Embon, L.,** Anahory, Y., Suhov, A., Halbertal, D., Cuppens, J., Yakovenko, A., Myasoedov, Y., Rappaport, M. L., Huber, M. E., Gurevich, A., and Zeldov, E. Probing dynamics and pinning of single vortices in superconductors at nanometer scales, Accepted for publication in *Sci. Rep.*

תקציר

מיקרוסקופ סורק חדשני, המבוסס על התקן התאבכות קוונטית של מוליכי-על (ההקמ״ע) על חוד פותח ונבנה. ההקמ״ע על חוד (הע״ח) קטנים עד כדי 46 ננומטר יוצרו בקצהו של חוד קוורץ משוך. ההע״ח מציגים רעש שטף נמוך עד כדי 50 ננו-קוונטת-שטף לשורש התדר, ערך הדומה להקמ״ע השקטים ביותר אשר דווחו. התקנים אלה מסוגלים לפעול בשדה מגנטי גבוה עד טסלה, ויש להם רוחב פס גדול, החל מסטטיקה ועד למעל מגה-הרץ. כיוון שלהע״ח הצורה המיטבית למיקרוסקופיה סורקת, ניתן לסרוק אותם ננומטרים ספורים מעל פני שטח של דוגמא, ורעש הספין שמתקבל נמוך עד כדי 0.38 מגנטרון-בוהר לשורש תדר, שיפור של קרוב לשני סדרי גודל ביחס לכל ההקמ״ע אחר.

המיקרוסקופ הסורק מבוסס הע״ח הוא כלי גמיש, אשר ניתן להשתמש בו לחקר מגוון רחב של מערכות המציגות תופעות מגנטיות בטווח האורך הננומטרי. תכנון המיקרוסקופ, הייצור והאפיון של ההע״ח, כמו גם דוגמאות ממחקר של זרימת שטף מגנטי במוליכי-על ומבחינת התכונות המגנטיות המופיעות במפתיע בתווך שבין שתי תחמוצות מוצגים בחלק הראשון של העבודה.

בחלקה השני, אני מדווח אודות שימוש במיקרוסקופ לחקר הדינמיקה של מערבולות מגנטיות במוליכי-על, וריתוקן על ידי פגמים בשכבות עופרת דקות. מחקר זה התאפשר הודות לרגישות המגנטית חסרת התקדים וליכולת למדוד תנודות הקטנות מאנגסטרם בודד. מדדנו, לראשונה, את התלות הבסיסית של של כח הריתוק של צבר פגמים כתלות במיקום המערבולת, וגילינו התנהגות מורכבת הרבה יותר מהידוע עד כה. זאת, כוללת התרככות מפתיעה של כח הקפיץ, השתחררות המערבולת מריתוקה כקפיץ שבור, וכן קפיצות ספונטניות בעלות חשל בין אזורי ריתוק שונים של המערבולת. התוצאות שלנו מצביעות על חשיבותן של תנודות תרמיות אפילו ב-4.2 קלווין, ועל התפקיד המכריע של אדוות קלות בפוטנציאל הריתוק, דבר השופך אור על המנגנונים שמאחורי ההתנהגות החשמלית של מוליכי-על.

Declaration

This thesis summarizes my independent effort.

This work was done in close collaboration with Dr. Yonathan Anahory. The scanning SOT microscope, the vibration isolation system and the supporting characterization and experiment automation software were designed and realized by the author. Dr. Anahory developed the Pb SOT fabrication technique with the assistance of Drs. Denis Vasyukov, Yuri Myassoedov and Michael Rappaport. The SSAA was fabricated in NIST by Prof. Martin E. Huber from the University of Colorado, Denver. The feedback electronics were originally designed by Prof. John M. Martinis and modified by Prof. Huber. The Pb micro-bridge samples were designed by the author and fabricated by Dr. Anahory. The sample used in part II was characterized by the author, Dr. Anahory and Dr. Jo Cuppens. Dr. Anahory wrote the data analysis software with the help of Anton Yakovenko. Dr. Alex Meltzer (Suhov) and Prof. Alex Gurevich from Old Dominion University carried out and analyzed numerical and analytical calculations. Dorri Halbertal performed numerical analysis and parametric fitting. The experiment was developed and carried out by the author together with Dr. Anahory and Prof. Eli Zeldov. These workers also analyzed and interpreted the results together with Prof. Gurevich. Part II is based on an “accepted for publication” paper that was written by the author, Prof. Zeldov, Dr. Anahory and Prof. Gurevich. Prof. Zeldov orchestrated the entire project, also taking active part in the measurements and analysis of the data.